# MULTI-AXIAL FATIGUE CRACK GROWTH UNCERTAINTY QUANTIFICATION AND RISK MANAGEMENT

By

Kevin Adam Wolfe

Thesis

Submitted to the Faculty of the

Graduate School of Vanderbilt University

in partial fulfillment of the requirements for

the degree of

MASTER OF SCIENCE

in

Civil Engineering

December, 2012

Nashville, Tennessee

Approved:

Professor Sankaran Mahadevan

Professor Prodyot K. Basu

To my family and my teachers.

## ACKNOWLEDGMENTS

There are many people who aided in the work presented here. My research advisor, Dr. Sankaran Mahadevan, was always available to give support and guidance in my work here at Vanderbilt and for that I am very appreciative. Dr. Mahadevan was a terrific teacher and provided not only classroom knowledge but also novel ways to approach problem solving. The experience I gained from studied under his tutelage is invaluable resource and something that I will build on throughout the rest of my life.

The research performed was sponsored in part by the Federal Aviation Administration, William J. Hughes Technical Center (Project Manager: Dr. John Bakuckas) and NASA Ames Research Center (Project Manager: Dr. Kai Goebel). I would like to acknowledge Dr. Goebel and Dr. Yongming Liu of Arizona State University for the guidance provided during monthly progress teleconferences.

I would also like to provide special recognition to Dr. Vadiraj Hombal for his constant support and guidance. Dr. Hombal was instrumental in the crack growth modeling portions of this research and contributed many helpful suggestions and supplies to the experimental studies provided. Dr. Arun Krishnan provided a great deal of insight in the experimental procedure and the quantification of the associated errors.

I am also very grateful to have been part of a great team in the Risk and Reliability Research group at Vanderbilt. I would like to thank You Ling and Josh Mullins in particular for their assistance in the parameter calibration and model validation portions of this research.

## TABLE OF CONTENTS

PAGE

DEDICATION ..... ii

ACKNOWLEDGMENTS ..... iii

LIST OF TABLES ..... vii

LIST OF FIGURES ..... vii

CHAPTER

1. INTRODUCTION ..... 1

    1.1 Motivation ..... 1

    1.2 Organization of the thesis ..... 4

2. BACKGROUND INFORMATION ..... 7

    2.1 Gaussian process surrogate modeling ..... 7

    2.2 Surrogate modeling of 3D crack growth ..... 8

    2.3 Bayesian networks ..... 12

3. QUANTIFICATION OF DISCRETIZATION ERRORS USING SURROGATE MODELING TECHNIQUES ..... 17

    3.1 Introduction ..... 17

    3.2 Simulation of non-planar crack growth ..... 19

    3.3 Crack representation ..... 25

    3.4 Surrogate modeling for non-linear kinetics of crack growth analysis ..... 30

    3.5 Illustration of discretization error modeling ..... 38

3.6 Conclusion ..... 43

4. IDENTIFICATION OF ERRORS IN FATIGUE EXPERIMENTATION AND BAYESIAN MODEL PARAMETER CALIBRATION ..... 45

4.1 Introduction ..... 45

4.2 Experimental setup ..... 47

4.3 Sources of error in fatigue experiments ..... 49

4.4 Bayesian model parameter calibration ..... 54

4.5 Implementation of Bayesian calibration ..... 57

4.6 Conclusion ..... 64

5. MODEL VALIDATION ..... 66

5.1 Introduction ..... 66

5.2 Discretization error in EPCG model ..... 67

5.3 Experimental Data from Bell Helicopter Textron Inc. ..... 69

5.4 Experimental testing and model parameter calibration ..... 70

5.5 Bayesian model validation ..... 76

5.6 Conclusion ..... 80

6. STRUCTURAL HEALTH MONITORING AND FATIGUE DAMAGE PROGNOSIS FOR CONDITION BASED MAINTENANCE INSPECTION SCHEDULING ..... 81

6.1 Introduction ..... 81

6.2 Types of non-destructive testing ..... 85

6.3 Reliability-based validation metric ..... 86

6.4 Estimation of detectability limit ..... 88

6.5 Damage tolerance methodology ..... 89

6.6 Numerical example: inspection interval estimation..... 92

6.7 Extension to include inspection fidelity..... 96

6.8 Framework for implementation with inspection fidelity considerations ..... 98

6.9 Extension of numerical example to include inspection fidelity..... 99

6.10 Conclusion ..... 101

7. CONCLUSIONS AND FUTURE WORK ..... 103

REFERENCES ..... 106

## LIST OF TABLES

3.1 Load Block Descriptions……24

3.2 Load History Descriptions……...24

3.3 First Ten Principal Components……..29

3.4 Training Data for First Order Markov Kinetics…….. 31

3.5 Training Tables for Surrogate Modeling for Crack Growth Analysis…… 34

3.6 Surrogate Model Training at Various Resolutions……..35

5.1 Validation Results for Unadjusted Prediction Model……..79

5.2 Validation Results for Adjusted Prediction Model……. 79

6.1 Results of Digital Model Simulation……. 100

6.2 Updated Paris Law Parameters…….. 101

## LIST OF FIGURES


2.1 Equivalent-Planar Crack Growth…… 10

2.2 Conceptual Bayes Network……. 14

3.1 Stress Profile in Rotorcraft Mast……. 21

3.2 Finite Element Meshes of Rotorcraft Mast……. 21

3.3 Loading History 1…… 25

3.4 Crack Configurations for Load History 1…… 25

3.5 Spline Representation of Crack Fronts…… 27

3.6 Crack Front Predictions Corrected for Temporal Discretization…… 36

3.7 Implementation of Discretization Error Compensation Procedure……. 37

3.8 Temporal Discretization Surrogate Model…….. 39

3.9 Crack Growth Predictions Considering Temporal Discretization……... 40

3.10 Spatial Discretization Surrogate Model……... 41

3.11 Crack Growth Predictions Considering Spatial Discretization…… 41

3.12 Spatiotemporal Discretization Surrogate Model…….. 42

3.13 Crack Growth Predictions Considering Spatiotemporal Discretization……...43

4.1 CT Specimen Composed of 7075 Aluminum…….. 48

4.2 Schematic of Experiment Assembly…… 49

4.3 Procedure for Tracking Alignment Dots……..52

4.4 Dot Tracking to Measure Position Variation……... 53

4.5 Calibration Errors for MTS Equipment……53

4.6 Illustrative Diagram for General Model……...55

4.7 Bayes Network for CT Specimen Crack Growth……58

4.8 da/dN vs. dK for CT Specimens……...59

4.9 Prior Distributions of $C$ and $m$ ……60

4.10 Distributions of $C$ and $m$ Parameters after Calibration……61

4.11 Posterior Distributions for Other Calibrated Parameters……. 62

4.12 Distributions of $C$ and $m$ Parameters after Refined Calibration…….. 63

4.13 Posterior Distributions of Other Parameters…… 64

5.1 Crack Length Validation Comparison……..71

5.2 Bayes Network for Calibration with Multiple Information Sources……75

5.3 Implementation of Calibration Procedure…… 75

5.4 Posterior Distributions of Calibrated Parameters……76

5.5 Experimental Data vs. Model Prediction……. 78

6.1 Determination of Inspection Interval Prior to Actual Crack Occurrence…… 90

6.2 Determination of Inspection Interval after First Inspection……90

6.3 Determination of Inspection Interval after Flaw has been Observed…….. 90

6.4 Framework for Maintenance Inspection Scheduling……92

6.5 Model Reliability Curve……...93

6.6 Actual Crack Growth and Initial Model Prediction……. 94

6.7 Actual Crack Growth Compared against the Model after 1st Inspection……. 95

6.8 Actual Crack Growth Compared against the Model after 2nd Inspection…… 95

6.9 Maintenance Inspection Schedule for Numerical Example……. 96

6.10 Bayes Network for Simulation Model…… 97

6.11 Framework for Inclusion of Inspection Fidelity……99

# CHAPTER 1

# INTRODUCTION

## 1.1 Motivation

In many engineering systems, there are mechanical components that are subjected to cyclic loads which cause fatigue crack growth. These components are often critical to the survival of the system as a whole, and a thorough understanding of their performance is crucial to facilitate risk assessment and management. In 1978, Battelle Laboratories completed a study requested by the National Bureau of Standards that investigated the total cost associated with material fracture in the United States [1]. That study determined that over $88 billion dollars per year were being spent on material fracture at that time. This expenditure represented almost 4% of the national gross domestic product during that year [2]. The results of the report led to a surge in research emphasizing on fracture mechanics, material properties, and improved inspection scheduling/techniques. These were the areas that were deemed critical toward the improvement of structural reliability, reduction of material usage, and minimization of the replacement of critical components.

Among the major industrial sectors where fatigue and fracture of structural components are of critical concern is the aeronautical and aerospace industry. The aerospace community initially adopted a safe life approach in order to increase structural integrity throughout the design life of a component. In this approach, components are designed to withstand a pre-determined life and the assumption is that the components

will remain free of flaws. Under this philosophy, critical components are retired from service at the end of the pre-determined safe life period regardless of the current condition of the component. There are several deficiencies in this type of approach to risk management. The first of which is the over-design of the components and the waste of resources due to the removal of "good" components from service long before necessary. Another less common, but highly critical, flaw is that unique situations may lead to a critical flaw being achieved in the component within the safe life of the component.

The limitations in the safe life philosophy led to the development of a damage tolerance approach. Damage tolerance (DT) design is based on the assumption that initial flaws exist in any structure and such flaws will propagate under repeated cyclic loading conditions which are substantially less that the yield stress of the material. The concepts of the damage tolerance approach are based on fracture mechanics principles and have been pursued for fixed-wing aircraft structures since the 1970s [3]. In order for a DT approach to be viable, a detailed understanding of relevant component service loads and stress spectrums, material properties, and crack growth mechanisms must be known.

The goal of this thesis is to add to the collective knowledge used for proper implementation of a DT approach to risk management of a fatigue-critical mechanical component. The first aspect necessary for proper use of the DT methodology is an accurate crack growth model that can be used to determine the life remaining before an inspection is necessary. Since numerous studies have been performed to assess the uncertainty in three dimensional crack growth models [4, 5], this thesis will have a precise focus on numerical errors related to temporal and spatial discretization that have

not been previously investigated in much detail.

Crack growth models employ the use of material parameters such as threshold stress intensity factor, fracture toughness and other parameters that are model specific like Paris law parameters $C$ and $m$; the values of which are typically obtained via experimental testing. The variability in the experimental data is typically attributed to either inherent variability in the material itself or some type of observation error. In order to develop a firm understanding of the actual uncertainty in the material parameters, a calibration technique that considers all forms of uncertainty in the experimentation must be employed. Such a technique is developed in this thesis.

Once a detailed and robust crack growth model is achieved, the model is used to predict the amount of remaining life in the component before an inspection is necessary to evaluate the condition of the component. The DT approach provides a means for determining a safe and efficient maintenance inspection interval, but there is no consistent methodology for making the decision of what type of inspection should be performed. There are several different types of non-destructive testing that could be performed at a given maintenance event. Some inspections are inexpensive and easy to perform but do not yield precise information regarding the current condition of the component. Other inspection systems yield detailed insight into the current state of the component, but require highly trained technicians or costly specialized equipment. Another issue of concern with inspection fidelity choice is downtime. Some inspection procedures require the component in question to be removed from the engineering system in order to be analyzed while other can be performed while the component is in-service. This thesis develops an inspection planning methodology that decides both the schedule

and the type of inspection technique by taking into account the various uncertainty in crack growth prediction – natural variability, data uncertainty and model uncertainty.

### 1.2 Organization of the thesis

The primary objectives of this thesis are investigate modeling and experimental errors that affect growth life prediction and to extend DT risk assessment to include decision making with respect to the inspection scheduling and fidelity. Each chapter in the thesis employs the use of one of two three dimensional crack growth models. The first crack growth model is an equivalent planar approach to modeling non-planar crack growth and the second employs a non-parameterized representation of the crack fronts using principal component analysis.

The thesis is organized into seven chapters. Chapter I provides the motivation behind the presented research and outlines the organization of this thesis. Chapter II provides a brief discussion of the key underlying statistical and mathematical techniques used in this research, which includes Bayesian analysis and Gaussian process surrogate modeling. Chapter II also presents a detailed description of the equivalent planar crack growth model.

Chapter III develops a methodology for quantification of the numerical errors incurred due to discretization in the modeling of 3D crack growth. The non-parameterized crack front representation is employed in this chapter to ease the training of surrogate models used to quantify the discretization errors. The spatial discretization error caused by finite element meshing is investigated and although the methodology proposed is for a specific finite element solver, it could easily be extended to other finite

element software. Temporal discretization is also investigated in this chapter. Generally, loading in a crack growth simulation is applied in block form (collections of several load cycles of constant amplitude). Crack growth is dependent on not only the applied load, but also on the previous crack state. It is because of this dependency that the block loading leads to a discretization error. With block loading, the crack increment for a single load cycle is simply multiplied by the length of the block to determine the crack growth increment over the total load block duration. Ideally the crack growth would be calculated incrementally after each load cycle and the difference between the block approach and the cycle by cycle approach is referred to as the temporal discretization error. The methodology proposed in Chapter III provides a technique for quantification of this type of numerical error. For practical engineering problems, it is important to not only understand the individual contributions of temporal and spatial discretization, but also the combined effect. The combined spatio-temporal discretization is also modeled in Chapter III of this thesis.

Chapter IV seeks to fulfill two goals. The first goal is to investigate the types of uncertainty that are present in fatigue fracture experimentation. Machine calibration and alignment, imaging errors, and other observation errors are investigated. The second goal of the chapter is to account for these identified sources of error/uncertainty in calibrating material properties that are necessary for modeling of fatigue crack propagation. Bayesian model parameter calibration is employed for this purpose.

The results of the model parameter calibration, along with the discretization error quantification presented in Chapter III will then be used to correct the equivalent planar crack growth model. The goal of Chapter V is to validate the equivalent planar crack

growth law model using experimental results obtained from Bell Helicopter Textron Inc. for a two radius hollow cylinder similar to a rotorcraft mast. Chapter V demonstrates how multiple sources of data can be combined in a Bayes network to provide a robust validation scheme. Bayesian hypothesis testing will be utilized to perform this task and a model confidence based on the validation will be presented.

Chapter VI extends the DT approach to risk management in fatigue critical components to consider inspection scheduling and fidelity. The effect of inspection fidelity and model prediction uncertainty on the length of the next inspection interval is studied. The information gained from the analysis is then used for decision making regarding inspection schedule and fidelity.

A summary of the results of each chapter is provided in Chapter VI. The potential future work that could be performed to expand on the current study is also presented in the chapter.

# CHAPTER 2

# BACKGROUND INFORMATION

This chapter provides a brief introduction to some the key underlying statistical and mathematical techniques that are essential to the formulation of the uncertainty quantification and risk management methodologies developed in this thesis. The focus of the first section of this chapter will be on the development of Gaussian process models. Gaussian process regression models are used heavily in the second section of this chapter to introduce a crack growth model that will be utilized in Chapters V and VI and in Chapter III for the use of uncertainty quantification in another 3D crack growth model. The third section of this chapter will provide the reader with a basic introduction to Bayesian networks. Bayesian networks will be utilized in Chapters IV, V and VI for the use in Bayesian model parameter calibration.

## 2.1 Gaussian process surrogate modeling

In many practical engineering problems, complicated finite element solvers or computationally taxing computer simulations must be employed to obtain numerical data for detailed analysis. Reliability studies require a vast amount of numerical data which makes problems where the acquisition of said data is computationally difficult very cost prohibitive. To overcome this hurdle, surrogate models are typically developed. Surrogate models, or as they are sometimes called approximation models, are designed to mimic the simulation model as closely as possible while being far more computationally

more efficient. Different types of surrogate modeling techniques (conventional polynomial response surface, polynomial chaos expansion [6], support vector regression [7], relevance vector regression [8], and Gaussian process interpolation [9]) have been investigated in the literature. This thesis employs the use of the Gaussian process (GP) surrogate modeling approach, which is a powerful technique based on spatial statistics for interpolating data and is increasingly being used to build surrogates to expensive computer simulations for the purposes of optimization and uncertainty quantification [9, 10, 11]. There are three distinct advantages to the GP model over other surrogate modeling approaches: 1) it is not constrained by polynomial-type functional forms, 2) it is capable of representing highly nonlinear relationships in multiple dimensions, and 3) it produces an estimate of the prediction uncertainty dependent on the quantity and location of training data.

To demonstrate how a GP is built, consider an illustrative example. Let the underlying function $f: \Omega \rightarrow \Re, \Omega \in \Re^D$ be known at $N$ training points. The set $\mathcal{D}_T = \{\mathbf{x}_T, \mathbf{y}_T\}$ represents the training data where $\mathbf{x}_T = \{\mathbf{x}_1, \mathbf{x}_2, \dots \mathbf{x}_N | \mathbf{x}_i \in \Omega\}$ is the set of measurement locations and $\mathbf{y}_T = \{\mathbf{y}_1, \mathbf{y}_2, \dots \mathbf{y}_N | \mathbf{y}_i = f(\mathbf{x}_i)\}$ is the set of measured function values. $\mathbf{f}_T = \{\mathbf{f}_1, \mathbf{f}_2, \dots \mathbf{f}_N | \mathbf{f}_i = f(\mathbf{x}_i)\}$ is the set of underlying function values. It is assumed that measurement noise, $\epsilon_i \sim \mathcal{N}(0, \sigma_n^2)$.

The information contained in data $\mathcal{D}_T$, is then used to infer $\mathbf{f}_p$, the value of the underlying function $f$ at points $\mathbf{x}_p \in \Omega$, by computing the distribution $p(\mathbf{f}_p | \mathcal{D}_T)$. In general, a trend function is then applied and the residuals of the trend function are modeled by a Gaussian process. A GP is fully defined with the specification of the mean function, $m(\mathbf{x})$, and the covariance function, $k(\mathbf{x}, \mathbf{x}')$. These functions must be selected

so as to reflect the assumptions (such as stationarity, periodicity, etc) about the underlying function describing the data [12, 13, 14]. The covariance function provides a flexible and realistic assessment of the prediction variance, and quantifies the effect of the distance between prediction and training points. A detailed comparison of different covariance functions, both stationary[15] and non-stationary[16], can be found in the literature.

### 2.2 Surrogate modeling of 3D crack growth

The main goal of this thesis is to provide methodologies toward uncertainty quantification and risk management in a three-dimensional crack growth. Toward this goal, two different crack growth models, both with the capability of capturing the non-linear kinetics of non-planar crack growth in a mechanical component under multi-axial, variable amplitude loading, will be analyzed. One approach will employ a non-parameterized representation of the non-planar crack. The basic idea behind this proposed method is that it allows for the user to monitor complex crack configurations and the generation of arbitrary crack front shapes. A detailed discussion of this method will be presented in Chapter III along with the quantification of discretization errors related to simulated crack growth.

In this section, a second approach to non-planar crack growth will be discussed. The second proposed method for crack propagation modeling employs a parameterized, equivalent-planar representation of the simulated crack fronts. For each of these methods, the surrogate models implemented will be trained using finite element analysis results produced via FRANC3D[17]. FRANC3D is a finite element based solver

specifically designed to simulate non-planar crack growth of complex three dimensional structures.

The primary advantage to the planar approximation is that the crack representation is limited to an idealized semi-elliptical shape (see Figure 2.1) that is characterized by two geometric quantities, $a$ and $c$. The stress intensity factor range and crack growth increment at each load increment need only be calculated at the semi-major A) and semi-minor (C) axis locations. Equivalent planar crack growth projects the non-planar cracks onto a single oriented plane, and therefore reduces the complexity involved in the crack representation, enabling the propagation to be modeled more efficiently.

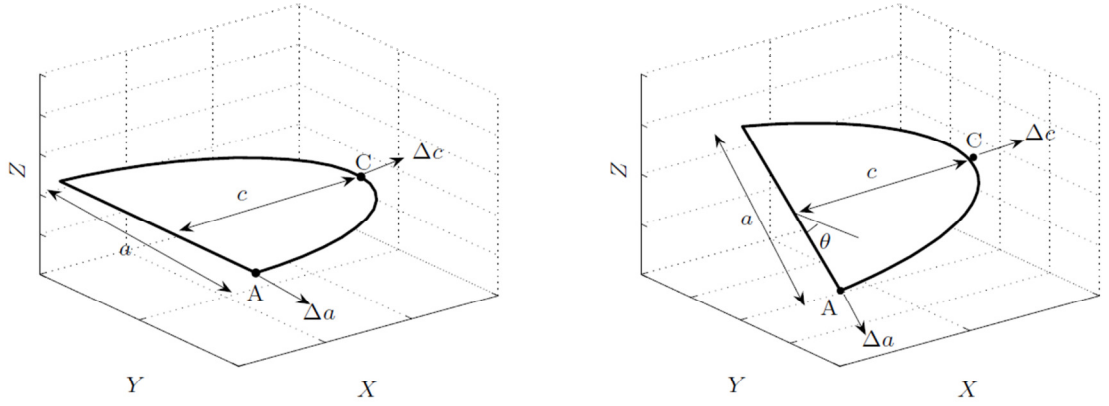


(a) Planar Crack Growth (b) Equivalent Planar Crack Growth

Figure 2.1: Equivalent-planar crack growth: $A$ corresponds to crack edge along the major axis and $C$ to the crack edge along the minor axis.

Equivalent planar approximation relies on an estimate of the overall crack orientation for its analysis [18]. Considering block loading in this application, each applied load scenario will consist of a different number of load blocks, a block-by-block relationship between crack characteristics, and the applied load considered:

$$\mathbf{w}[n+1] = g(\mathbf{w}[n], \mathbf{u}[n])$$

where $g$ is a non-linear function that defines the relationship between the current crack shape, $\mathbf{w}[n]$, and the applied loading $\mathbf{u}[n]$ at the $n$-th load block. Crack shape is represented by the crack configuration (orientation and length), $\mathbf{w}[n] = (\theta[n], a[n])$, and the applied load. This non-linear relationship is modeled as a GP:

$$\mathbf{w}[n+1] = \mathcal{GP}(\mathbf{w}[n], \mathbf{u}[n], \Phi) \quad (1)$$

where $\Phi = [\lambda, \sigma_p, \sigma_n]$ represents the parameters of the squared exponential covariance function assumed for the GP. The parameter $\sigma_n$ represents the uncertainty in the training values of $\theta_n$ and $a_n$ which results from variations in the FRANC3D mesh parameters set for each crack increment simulation. The parameter $\sigma_p$ represents the variability in the output variable. The length scale parameters, $\lambda$, characterize the variation of the output variable with respect to the input variables and therefore quantify the importance of each input variable. The training of the surrogate model consists of estimating the parameters $\Phi$ of the model using the training data acquired the finite element analyses.

The first surrogate model implemented in this equivalent planar crack growth prediction technique is utilized to predicted the orientation of the crack front while the second is used to estimate the stress intensity factor range at a given crack stage. The stress intensity factor is a function of crack shape, component geometry and applied load. As described in [19], an efficient surrogate model can be constructed to replace the finite element simulation in the calculation of the stress intensity factors for crack growth on a plane. For use here however, the plane is actually an equivalent plane meaning the surrogate model must be adapted to account for the crack orientation. The surrogate model extended for $\theta$ as an additional input is

$$K_{eq} = \mathcal{GP}(a, c, \boldsymbol{u}, \theta, \Phi) \quad (2)$$

Once the two surrogate models for crack orientation and stress intensity factor calculation are completed, the crack prediction model can be assembled. Since the main components to most crack growth laws are current crack shape, stress intensity factor range, and loading duration, this surrogate modeling methodology could be applied to any such crack growth model. In this thesis however, Paris law is implemented due to its simplicity and accessibility.

### 2.3 Bayesian networks

In this thesis, Bayesian calibration will be used to determine the distributions of model parameters when experimental data is available. The model's prediction is compared against the experimental data and samples are taken of the parameters so that the likelihood of the model prediction matching the data is maximized. To perform this, Bayesian networks are employed to gather all model parameters and sources of uncertainty.

To understand how a Bayesian network is operated, one must first have a solid understanding of Bayes' theorem [4] on which the approach is based. First consider a group of mutually exclusive and collectively exhaustive events $A_i$ ($i = 1$ to $n$) that together form a sample space. Suppose then that $B$ is any other event from the sample space, as long as $P(B) > 0$, it can then be deduced that from the law of conditional probability

$$P(A_i|B) = \frac{P(B|A_i)P(A_i)}{\sum_j P(B|A_j)P(A_j)} \tag{3}$$

A physical interpretation of the above equation will follow. In Bayesian terminology, the quantities $P(A_i)$ are known as prior probabilities and are the

probabilities of the events prior to any observed data. If an event $B$ is then observed, the result of the equation can then be calculated and the result, $P(A_i|B)$, is known as the posterior probability. It is by this methodology that Bayesian analysis updates a prior assumption about the distribution of a random variable based on observed instances of that variable or functions of that variable.

A Bayesian network is a graphical representation of the relationship between various uncertain quantities in a system. Bayesian networks are an example of a directed acyclic graph, which is to say that it is a collection of vertices and directed edges. Since a Bayesian network is a mean by which the outputs of component and subsystem level tests can be related to the inputs of the overall system, the nodes or vertices of the Bayesian network represent each uncertain quantity in the system and the directed edges represent the nodes' relationships in the terms of conditional probabilities. Disconnected nodes imply independence between the corresponding random variables. An example of a conceptual Bayesian network that aids in uncertainty quantification across multiple levels of models and observed data is presented in Figure 2.2. The common presentation (used in Figure 2.2 also) in Bayesian network is to represent uncertain parameters with circular nodes and to represent observed data with square nodes. The conditional probability links between variables are represented by solid edges in the diagram and if observable data is available for a particular variable then that relationship is illustrated with a dashed line in the figure.

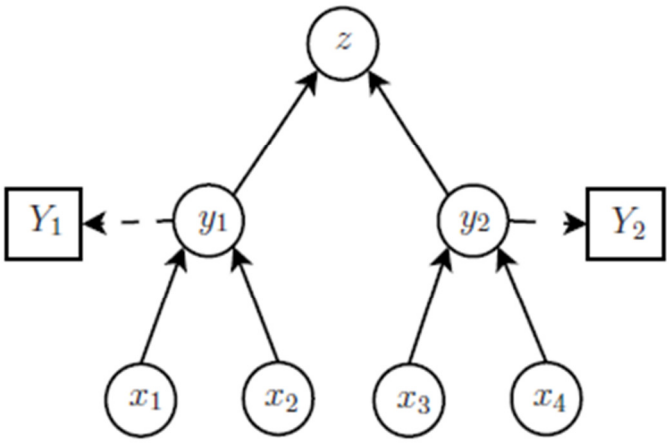


Figure 2.2: Conceptual Bayesian Network

The system presented in Figure 2.2 is composed of two subsystems. The system output $z$ is a function of the two subsystem outputs $y_1$ and $y_2$. Each subsystem has two distinct input variables: $x_1$ and $x_2$ for subsystem 1 and $x_3$ and $x_4$ for subsystem 2. In this sample problem, two of the input variables, $x_2$ and $x_4$, are to be considered as model parameters such as a material properties geometric constants. For the sake of demonstration it is assumed that there is no observation data for the system level output, but observable data is available at the subsystem outputs and that data is represented in the figure as $Y_1$ and $Y_2$.

There are two methods of use for Bayesian networks: forward problems (uncertainty propagation along the the flow of the Bayesian network) and inverse problems (updating the uncertainty in the parent nodes based on the data on a dependent node using Bayesian inference [5]). Since the inverse problem is the type necessary for the use of Bayesian networks in this thesis, that method will be presented. For more details on the forward problem see [20].

In the inverse problem, the probability densities of the model parameters ($x_2$ and $x_4$ in Figure 2.2) can be updated based on the observed data ($Y_1$ and $Y_2$) using Bayes theorem as:

$$f(x_2, x_4|Y_1, Y_2) \propto L(x_2, x_4) f'(x_2) f'(x_4) \quad (4)$$

The joint posterior density is given by $f(x_2, x_4|Y_1, Y_2)$. The likelihood function, $L(x_2, x_4)$, is calculated as the probability of observing the given data ($Y_1$, $Y_2$), conditioned on the parameters being updated, i.e. $x_2$ and $x_4$. The likelihood function accounts for the uncertainty in the inputs $x_1$ and $x_3$. For details of the likelihood function, refer to [21].

A prior distribution ($f'(x_2)$ and $f'(x_4)$) is a representation of all of the knowledge known about a parameter before collecting any additional data. Prior distributions of the random variables of interest can be either informative or non-informative. If a significant amount of information is known about the behavior of a variable, an informative prior can be used and will assist the analysis. For instance, the parameters of common materials may have well known distributions, manufactured products may have specified nominal values and tolerance levels, or an expert may have a high level of confidence that a parameter falls in a certain interval range. This concept of the prior distribution is heavily scrutinized by detractors of Bayesian statistical methods because the assumptions made about the prior distribution affect the result of the Bayesian analysis. Poor assumptions of prior information will ineffectively bias the resulting posterior distributions. However, the inclusion of useful information into a prior distribution increases the effectiveness of the analysis and eases the computational difficulty. The prior distribution describes the subjective knowledge about the system

and the associated uncertainty. This prior knowledge is updated in the Bayesian analysis process when new information becomes available in the form of testing or inspection data. This leads to the reduction of uncertainty in the system-level prediction. For more information about prior distributions, including non-informative priors, refer to [21].

# CHAPTER 3

# QUANTIFICATION OF DISCRETIZATION ERRORS USING SURROGATE MODELING TECHNIQUES

## 3.1 Introduction

Surrogate modeling is typically used to replace an intensive computer simulation in order to save time and expense. The surrogate model presented in this chapter represents non-planar crack growth in mechanical components under multi-axial, variable amplitude loading. The approach presented here accounts for the effect of both spatial and temporal discretization in the 3-D finite element analysis of non-planar crack growth.

The surrogate modeling technique that is presented here models the relationships between crack fronts obtained at different discretization levels. The surrogate model can use these relationships to predict crack front shapes that are corrected for the effects of discretization error. These corrected crack fronts are then used to develop another surrogate model that empirically captures the non-linear kinetics of the non-planar crack growth in a mechanical component under multi-axial, variable amplitude loading. The objective is to develop a computationally affordable yet accurate model, which uses a small set of training data to model the evolution of crack growth in the component. Once the model is trained, it can be used in a predictive manner to determine the next stage of crack growth given a current crack shape and loading scenario.

Existing methods for the use of surrogate models for crack growth modeling reduce the complexity in crack representation by assuming a parameterized planar crack

representation and model the relationship between crack size, applied loading, and equivalent stress intensity factors [22, 23].

While the parameterized crack representation enables rapid assessment of crack growth, a parameterized crack model also limits the possible shapes that the crack can take during the simulations. The surrogate model presented here employs a non-parameterized crack front curve thus allowing for a more realistic representation of non-planar cracks. By representing the cracks in this way, the analysis can consider complex crack front geometries. The crack can be allowed to propagate naturally forming arbitrary configurations thereby allowing the relationship between crack fronts at varying degrees of discretization to be modeled accurately. The proposed method is a three step approach which involves: 1) crack front representation, 2) estimation of corrected crack fronts (corrected for discretization errors), and 3) modeling of crack growth kinetics. First, a low dimensional non-parameterized representation of the crack front curves is sought. This first step is necessary so that the kinetics of the crack growth can be modeled in this low dimensional space which eases one of the computational complexities associated with this type of problem. In the low dimensional space, robust surrogate model training can occur with relatively little training data.

Description of the modeling of the fatigue crack growth in a cylindrical mechanical component (similar to a rotorcraft mast) is presented in Section 3.2 below. The focus is on defining the representation of multi-axial, variable amplitude load blocks and histories. A more elaborate discussion on the use of block loading in a fatigue crack growth application was presented in Chapter II. The example presented in Section 3.2

will be carried forward in each subsequent section for ease of illustration of the methods developed along the way.

Dimensionality reduction requires fixed dimension representation of the data space. For the problem of fatigue crack growth analysis, a spline-based representation of the crack front is considered. This type of representation reparameterizes the crack front curves such that all of the crack fronts associated with the analysis can be systematically represented in fixed dimension.

The Gaussian process regression presented in Section 3.3 is used to estimate the corrected crack front after the application of some given load block. This estimation is used to model the non-linear kinetics of crack growth under variable amplitude loading. In Section 3.4, a methodology is proposed to account for temporal, spatial, and combined spatio-temporal discretization errors.

### 3.2 Simulation of non-planar crack growth

In general there are a few items that crack growth models need in order to perform their function of fatigue crack growth prediction. An initial flaw size, shape and location is usually a prerequisite for fatigue crack growth analysis. Most models utilize some form of material constants for the given specimen, although for many models these "material properties" are just fitting constants based on experimental testing [24. Another common variable in fatigue crack growth models is the stress intensity factor at the crack tip. Since the stress intensity factor is dependent on the component's geometry, applied load, and current crack size and shape, these properties are also crucial to most analyses.

All of these factors are critical to the analysis in their own right, but their interaction with each other can also have important consequences in terms of implementation of full non-planar crack growth simulation. A more detailed description of the options available for the full scale simulation has been discussed in Chapter II. A brief discussion relevant to the non-parametric crack growth model is presented here.

For illustration purposes, a two-radius hollow cylindrical component like a rotorcraft mast is to be used throughout the remainder of this chapter. Based on stress analysis under bending and torsion loads, the fillet region of the component (see Figure 3.1) was identified as the region of highest stress concentration and therefore the most likely location for crack initiation to occur. Consequently, all analyses in this chapter assume that an initial elliptical surface flaw is present in the fillet region of the component. FRANC3D [17] is employed for automated crack representation and crack propagation. FRANC3D utilizes ANSYS [25] for component stress analysis and implements a crack tunnel and singular elements to provide automated local remeshing at the crack location. In order to ease computational effort a submodel of the fillet region was extracted from the full model. A diagram of the extracted submodel and the crack tunnel (local mesh) are presented in Figure 3.2. Within the software, the maximum shear stress criterion is used to determine the crack growth direction [25]. Paris law [26] is the crack growth model used to estimate the crack growth increment. The deterministic values used for "material constants" $C$ and $m$ were 1E-9 and 2.7 respectively. Deterministic values for these variables were used in this chapter for the sake of simplicity as their uncertainty is not of primary concern; however, a more detailed analysis of proper representation of these parameters is presented in Chapter IV. It

should also be noted that the methods of discretization error quantification presented here are not limited to the choice of aforementioned crack growth criteria. These specifics were only chosen for the clarity of illustration.

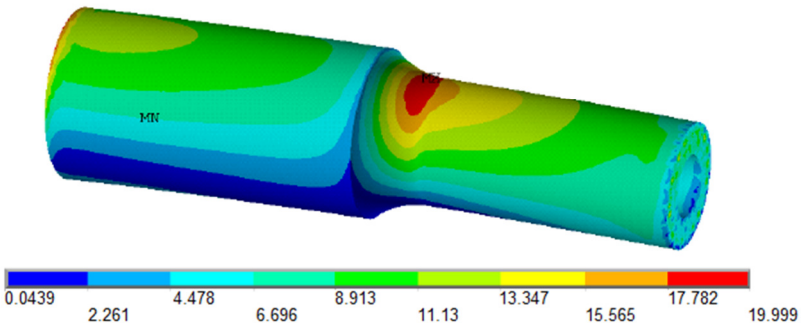


Figure 3.1: Plot of stress profile within rotorcraft mast component under bending and torsional loading

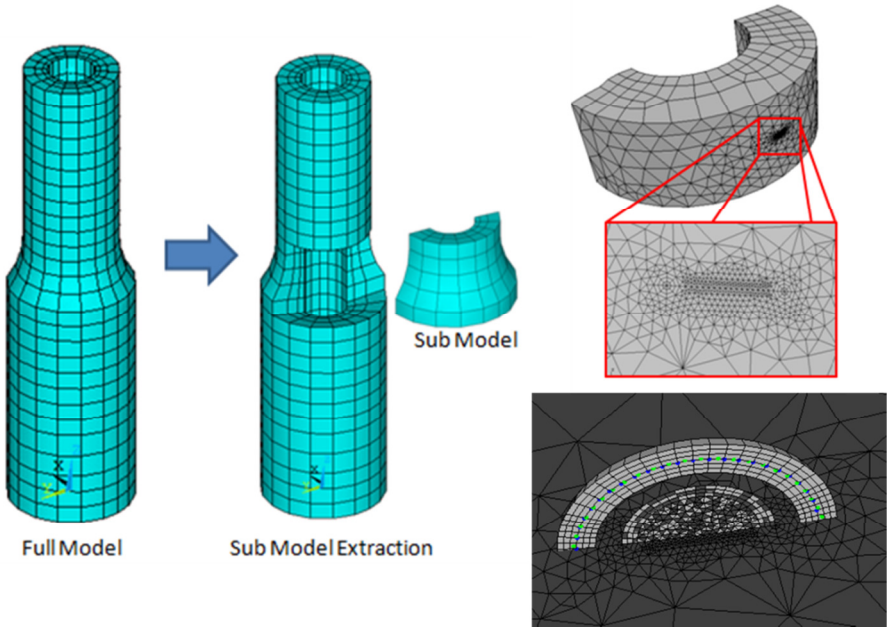


Figure 3.2: Finite element meshes of the full model, submodel, and crack tube (local mesh)

A cycle-by-cycle approach, in which the crack growth analysis is performed for each load cycle, provides the most accurate estimate of crack growth. Since the growth

per cycle is on the order of $10^{-10} - 10^{-8}$ in/cycle for this high cycle fatigue problem, this high fidelity approach presents significant computational demands both in terms of the number of cycles and the number of nodes required in the Finite Element Analysis (FEA) mesh. The complexity of the crack shape increases with each iteration of the simulation. This increases the requirements for the remeshing stage because more complex crack front shapes demand a finer mesh for accurate representation.

Therefore an incremental block-type crack extension analysis is employed here. Since the FEA program creates discrete points along the crack front to represent the crack shape, these points are how the crack is propagated. In the block loading approach, these specific points are extended by a multiple of the crack growth increment that was calculated by the FEA program for a single cycle:

$$\Delta a = d_k * \frac{da}{dN} \tag{5}$$

where $\Delta a$ is the total crack growth applied to the current location of the point on the crack front, $d_k$ is the user defined block duration, and $\frac{da}{dN}$ is the crack growth increment predicted by the FEA solver for a single cycle at the current crack state for that point along the crack front. The advantage to this method is that it allows for crack extension without the requirement of constant crack updating and remeshing after every load cycle making predictions for long mission durations attainable. There are some glaring weaknesses in this approach however. The first of which is the dependence on the load history consisting of several sub-blocks with constant amplitude loading. For some problems this assumption may not cause a large issue but for a component such as a rotorcraft mast it is highly unlikely that the load applied to the mast will be of constant amplitude for any sustained period of time. The second and more general problem will

be the focus of one of the subsequent portions of this chapter. Since the crack growth prediction is dependent on the previous crack state, it is erroneous to assume that the crack growth prediction for a single cycle will be correct for an entire block of cycles. The numerical error created by this assumption will be treated as the temporal discretization error from hence forward.

For this demonstration problem, each load history $L_k$ will consist of $N_k$ individual load blocks, $\{B_k[n]\}_{n=1}^{N_k}$. These load blocks represent different durations and bending and torsional load amplitudes, $B_k[n] = \{b_k[n], t_k[n], d_k[n]\}$. Because of constraints due to the FEA solver's ability to model incredibly small crack growth increments, the bending and torsional load values were limited to four values each: $b = \{1.75, 2.00, 2.25, 2.5\}$ and $t = \{0.5, 1.5, 2.5, 3.5\}$. The durations for each of the 16 possible load combinations were also chosen according to the previously mentioned FEA constraint. All of load blocks used in the demonstration problem are presented in Table 3.1.

Using the load blocks tabulated in Table 3.1, 28 load histories, each of 120,000 cycles total duration, were randomly generated using a bucket-filling algorithm. The algorithm begins by randomly selecting a load block. The next block is then selected randomly only this time with the constraint that the total duration must be less than 120,000 cycles. The process of random block selection continues until a load history of 120,000 total cycles is created. Note that while each load history has a total of 120,000 cycles, the number of blocks within each history varies. Twelve samples of these load histories, along with the corresponding final crack orientation $\theta_k$, are listed in Table 3.2. As an example, the first load history $L_1$ is illustrated in Figure 3.3. The corresponding

crack fronts are shown in Figure 3.4. The change in orientation of the crack fronts as they evolve is noted.

Table 3.1: Load block descriptions

| | *b* | *t* | *d* |
|---|---|---|---|
| 1 | 1.75 | 0.5 | 40 |
| 2 | 1.75 | 1.5 | 38 |
| 3 | 1.75 | 2.5 | 36 |
| 4 | 1.75 | 3.5 | 34 |
| 5 | 2 | 0.5 | 32 |
| 6 | 2 | 1.5 | 30 |
| 7 | 2 | 2.5 | 28 |
| 8 | 2 | 3.5 | 26 |
| 9 | 2.25 | 0.5 | 24 |
| 10 | 2.25 | 1.5 | 22 |
| 11 | 2.25 | 2.5 | 20 |
| 12 | 2.25 | 3.5 | 18 |
| 13 | 2.5 | 0.5 | 16 |
| 14 | 2.5 | 1.5 | 14 |
| 15 | 2.5 | 2.5 | 12 |
| 16 | 2.5 | 3.5 | 10 |

Table 3.2: Load histories descriptions

| | $B_k[1]$ | $B_k[2]$ | $B_k[3]$ | $B_k[4]$ | $B_k[5]$ | $B_k[6]$ | $B_k[7]$ |
|---|---|---|---|---|---|---|---|
| 1 | 4 | 11 | 2 | 12 | 16 | - | - |
| 2 | 7 | 1 | 7 | 9 | - | - | - |
| 3 | 12 | 13 | 10 | 6 | 15 | 15 | 16 |
| 4 | 4 | 5 | 5 | 10 | - | - | - |
| 5 | 7 | 14 | 16 | 6 | 7 | 16 | - |
| 6 | 10 | 6 | 1 | 15 | 13 | - | - |
| 7 | 1 | 3 | 16 | 10 | 15 | - | - |
| 8 | 4 | 16 | 15 | 3 | 7 | - | - |
| 9 | 14 | 15 | 4 | 6 | 11 | 16 | - |
| 10 | 5 | 4 | 11 | 16 | 15 | 15 | - |
| 11 | 16 | 12 | 2 | 11 | 4 | - | - |
| 12 | 2 | 16 | 4 | 12 | 11 | - | - |

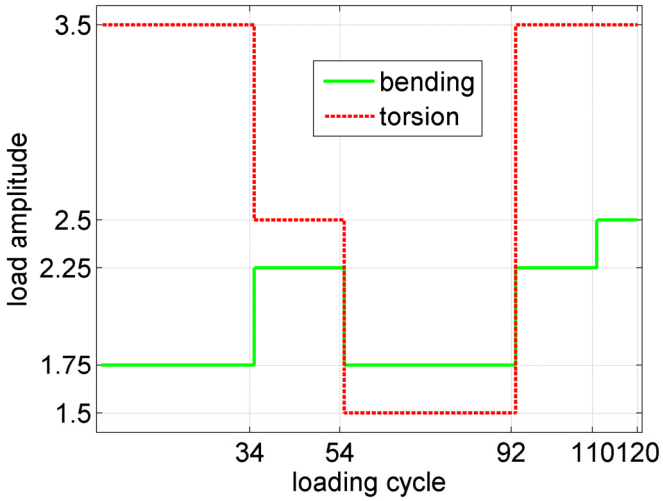


Figure 3.3: Loading history 1: 120,000 cycles of 5 loading blocks. Each block consists of bending load $b_k[n]$, torsional load $t_k[n]$, and load duration $d_k$

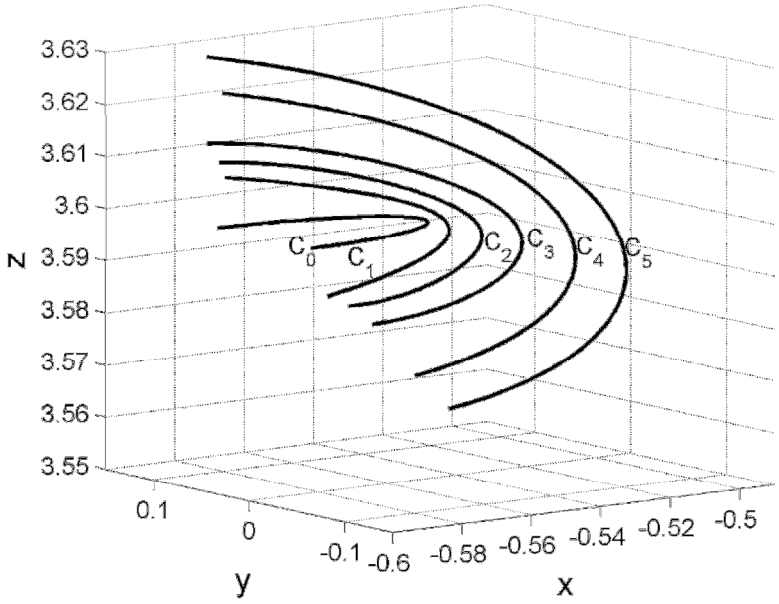


Figure 3.4: Crack configurations for load history 1: The five fronts after each of the five blocks in the load history has been applied.

### 3.3 Crack representation

The crack fronts generated by the simulation described in the previous section may be represented as $\mathbf{Q}_n = [\mathbf{X}_n, \mathbf{Y}_n, \mathbf{Z}_n]$, where $n$ is an index into the loading block, and $\mathbf{X}_n$, $\mathbf{Y}_n$, and $\mathbf{Z}_n$ are $N_n \times 1$ vectors of the respective Cartesian components of the $n$-th

crack front. Due to the mesh refinement that occurs after the application of each load block, the crack fronts consist of a varying number of representative points. As a consequence, no immediate correspondence can be established between the nodes belonging to two different crack fronts, and the development of a model that captures the relationship between the crack fronts is not possible. A consistent parameterized representation of the crack fronts is therefore required.

The first step toward the generation of a consistently parameterized representation is to develop a spline representation of the crack fronts $\mathbf{C}_n(s) = \{\mathbf{X}_n(s), \mathbf{Y}_n(s), \mathbf{Z}_n(s)\}$, where $s \in [0,1]$ is the spline parameter [27, 28]. This is achieved by parameterizing the elements corresponding to each component $\mathbf{C}_n$ with:

$$S_n = \left\{0, \frac{1}{\Delta_n}, \frac{2}{\Delta_n}, \ldots \frac{N_n-1}{\Delta_n}\right\}, \Delta_n = N_n - 1 \tag{6}$$

Thus the discrete points $\mathbf{Q}_n$ are now represented by the spline curve $\mathbf{C}_n(S_n)$. However, while the above representation provides a parameterization of all crack fronts in the interval [0,1], the correspondence between the crack fronts is not apparent since each crack front is still parameterized by a different set of $N_n$.

In order to represent all of the fronts by the same number of parameters the number of spline nodes, $M$, must be chosen and the spline node separation $\Delta \triangleq (M-1)^{-1}$ must be set. Then using the interpolation property of splines, each spline representation is reparameterized at $S = \{0, \Delta, 2\Delta, \ldots (M-1)\Delta\}$. The reparameterized representation of the $n$-th crack front corresponding to the load history, $L_k$ may then be written as:

$$\mathbf{C}_k^n(S) = \{\mathbf{X}_k^n(s), \mathbf{Y}_k^n(s), \mathbf{Z}_k^n(s)\} \tag{7}$$

where $\mathbf{X}_k^n(s), \mathbf{Y}_k^n(s),$ and $\mathbf{Z}_k^n(s)$ are now of size $M \times 1$. $\mathbf{Q}_k^n$ is the $n$-th crack front of load history, $L_k$, and is represented by $\mathbf{C}_k^n$, where the parameterization of the latter is implicitly understood. The crack fronts due to load history $L_i$, and their spline representations are shown in Figure 3.5 for illustration. The fidelity of the re-sampled spline representation increases as $M$ increases.

In general, crack fronts represent arbitrary curves with discontinuities and branching. While the crack fronts generated by the FEA simulation described in the previous section do not possess these characteristics, the use of splines allows for the modeling of discontinuities in the crack shape. In addition, an important consideration in this work is the ability to describe a crack of any arbitrary shape and analyze its propagation under a given load history.

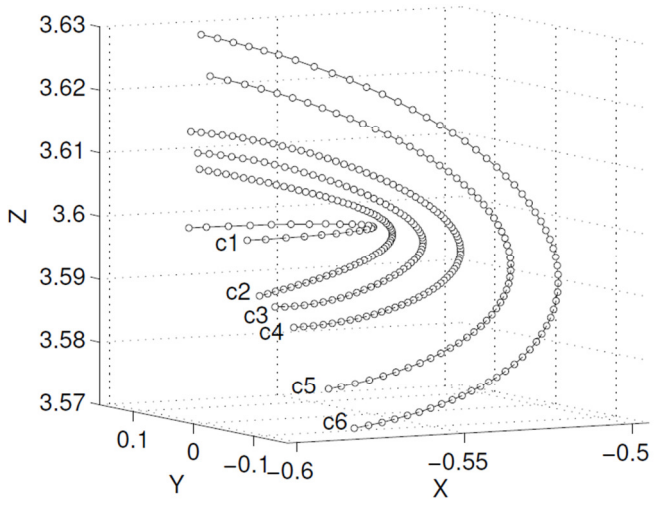


Figure 3.5: Spline representation of the crack front using $M = 31$ spline nodes per front: Mesh nodes are represented as lines and spline nodes as circles.

Under the reparameterization described above, each crack front $\mathbf{C}_k^n[n]$ is represented by a $3M$ – dimensional spline parameter vector: $\mathbf{C}_k^n[n] = \{\mathbf{X}_k[n], \mathbf{Y}_k[n], \mathbf{Z}_k[n]\}$. This allows for the modeling of arbitrarily shaped curves crack fronts and the modeling of them as

freely deformable space curves. While the fidelity of spline representation increases as $M$ increases, so does the dimension of the data space, $\Omega$. The tradeoff of representation fidelity versus data space dimensionality limits the use of space filling designs which are necessary for accurate training of surrogate models and thus prohibits direct modeling of crack growth kinetics in the high dimensional data space. Instead, a principal component analysis (PCA) based compact representation of the crack fronts, *C,* will be used.

Specifically, for each crack front $\mathbf{C}_k[n]$ a corresponding latent space representation must be found:

$$\mathbf{W}_k[n] = \mathbf{U}^T\,[\mathbf{C}_k[n] - \bar{\mathbf{C}} \tag{8}$$

where $\bar{\mathbf{C}}$ is the $1 \times 3M$ vector of the means of the crack fronts due to the training loading histories, $K$, and

$$N = \sum_{k=1}^{K}(N_k + 1) \tag{9}$$

which is the total number of crack fronts in the training set. $\mathbf{U}$ is a $3M \times D$ matrix containing the bases of the latent space and $\mathbf{W}$ is the $D \times N$ matrix of the latent variables corresponding to the $N$ crack fronts $\mathbf{C}$ in the training set. The dimension of the latent space is $D \leq M$.

Based on the covariance matrix of a spline component $\mathbf{S} = \mathbf{C}\mathbf{C}^{\mathrm{T}}$, PCA is employed to extract $3M$ uncorrelated linear bases for this space. These bases are ranked according to the amount of variance that they capture, with the first component accounting for the most variance. To achieve this ranking, PCA employs eigen-decomposition of the covariance matrix, $\mathbf{S}$; eigenvectors provide the uncorrelated bases, and eigenvalues provide a measure of the variance by which the corresponding eigenvector can be ranked [29]. This transformation may be inverted from latent space to data space using:

$$\mathbf{C}_k[n] = \mathbf{U}\mathbf{W}_k[n] + \bar{\mathbf{C}} \quad (10)$$

The latent space of the crack fronts was estimated using the parameterized representations of each of the crack fronts available from the $K = 28$ simulations. The contributions of the first 10 principal components (out of a possible $M = 93$ components) is tabulated in Table 3.3. As is seen in the table, the first principal component captures 97.38 percent of the variance. In other words, 97.38 percent of the variation of the $3M$ – dimensional domain is located along a line, and 98.48 percent of the variation on a plane spanned by the first two principal components. Thus the most important parts of the spline components are their projection on the subspaces spanned by these principal components. The crack front which is represented by $M$ – variables in the data space, collapses to a single point on a line or a plane in the latent space.

Table 3.3: First ten principal components: Eigenvalues and percentage of variability explained by the principal component

| $i$ | $\lambda_i$ | % variance |
|---|---|---|
| 1 | 0.0205 | 97.38% |
| 2 | 0.0002 | 1.10% |
| 3 | 0.0002 | 0.85% |
| 4 | 0.0001 | 0.45% |
| 5 | 0.0000 | 0.08% |
| 6 | 0.0000 | 0.05% |
| 7 | 0.0000 | 0.04% |
| 8 | 0.0000 | 0.03% |
| 9 | 0.0000 | 0.01% |
| 10 | 0.0000 | 0.01% |

The eigenvectors represent the principal modes of variation of the crack fronts about the mean shape $\bar{\boldsymbol{C}}$. The first principal component accounts for the directions of

major variation, which correspond to the direction in which the most active nodes move. For example, in the *X* spline component, most of the growth is in the middle nodes (see Figure 3.5) and the first principal component captures this variation. The second component accounts for the variation unexplained by the first component.

### 3.4 Surrogate modeling for non-linear kinetics of crack growth analysis

The previous section was concerned with the representation of the crack front. In this section the focus will be on modeling the crack growth process under a prescribed loading by modeling the trajectory of each crack in the latent space. Towards this, let $\mathbf{w}_n$ be the latent space representation of the crack front at the beginning of the *n*-th loading cycle. Application of a load $\mathbf{u}_n$ results in a new crack front represented by $\mathbf{w}_{n+1}$. The general form of this $p+1$-th order kinetics may be written as:

$$\mathbf{w}[n+1] = g(\mathbf{w}[n], \mathbf{w}[n-1], \dots \mathbf{w}[n-p], \mathbf{u}[n]) \tag{11}$$

where $p \geq 0$. In this work, it is assumed that *g* is a non-linear function of previous crack shape and loading history. By using previous crack shape and loading history as regressors, this non-linear function may be modeled by using a Gaussian Process Regression [14, 30, 31]:

$$\widehat{\mathbf{w}}[n+1] = \mathcal{GP}(\mathbf{w}[n], \mathbf{w}[n-1], \dots \mathbf{w}[n-p], \mathbf{u}[n]) \tag{12}$$

A brief introduction to Gaussian Process Regression was presented in Chapter II, for further details see [14]. For example, the first order Markov kinetics, in which the next crack shape depends only on the previous crack shape ($p = 0$), $\mathbf{w}[n+1] = g(\mathbf{w}[n], \mathbf{u}[n])$, the training data would be of the form presented in Table 3.4. By considering sequences such as $\big(\mathbf{w}[n], \mathbf{w}[n-1], \dots \mathbf{w}[n-p], \mathbf{u}[k]\big) \rightarrow \mathbf{w}[n+1]$,

the kinetics model may be extended with higher order ($p \geq 1$) dependencies in either the crack shape of the loading history. This only increases the number of input variables and thus the size of the training matrix. It should also be mentioned that only a single FEA simulation was used to illustrate the principals involved, but several such simulations may be incorporated.

Table 3.4: Training data for first order Markov kinetics

| Input 1 | Input 2 | Output |
|---|---|---|
| $\mathbf{w}[1]$ | $\mathbf{u}[1]$ | $\mathbf{w}[2]$ |
| $\mathbf{w}[2]$ | $\mathbf{u}[2]$ | $\mathbf{w}[3]$ |
| $\mathbf{w}[3]$ | $\mathbf{u}[3]$ | $\mathbf{w}[4]$ |
| ⋮ | ⋮ | ⋮ |
| $\mathbf{w}[L]$ | $\mathbf{u}[L]$ | $\mathbf{w}[L+1]$ |

Prediction for entire load histories may be obtained by considering an iterated GP model in which the crack front prediction from the previous stage is taken as input for the next stage:

$$\widehat{\mathbf{w}}[n+1] = \mathcal{GP}(\widehat{\mathbf{w}}[n], \widehat{\mathbf{w}}[n-1], \ldots \widehat{\mathbf{w}}[p], \mathbf{u}[n]) \quad (13)$$

Given an intial crack $\mathbf{w}[0]$ and a load history $L_k$ of $n$ loading blocks, the objective is to predict crack fronts $\widehat{\mathbf{w}}[1], \widehat{\mathbf{w}}[2], \ldots \widehat{\mathbf{w}}[n]$.

For illustration, a small example will be considered. The evolution of an initial crack front for load history $L = \{l_7, l_3, l_{11}, l_3\}$ will be predicted. The load history consists of 4 load blocks (7,3,11,3) with a total load duration of 120,000 cycles. Using a first order model and starting from an initial crack $C_0$, four crack fronts $(C_1, C_2, C_3, C_4)$ are to be predicted:

$$\widehat{\mathbf{w}}[1] = \mathcal{GP}(\mathbf{w}[0], l_7) \tag{14}$$

$$\widehat{\mathbf{w}}[2] = \mathcal{GP}(\widehat{\mathbf{w}}[1], l_3) \tag{15}$$

$$\widehat{\mathbf{w}}[3] = \mathcal{GP}(\widehat{\mathbf{w}}[2], l_{11}) \tag{16}$$

$$\widehat{\mathbf{w}}[4] = \mathcal{GP}(\widehat{\mathbf{w}}[3], l_3) \tag{17}$$

where $\mathbf{w}_i$ is the latent space representation of crack front $C_i$.

The work presented in this section up to this point has focused on the development of surrogate models for non-linear crack growth kinetics. The load blocks have been applied at their coarsest temporal resolution and the simulations have been performed at the coarsest spatial mesh. This methodology can now be extended to consider the effects of discretization by modeling the non-linear relationship between the corrected crack front, the applied load block, and the current crack shape:

$$\widehat{\mathbf{w}}^{\infty}[n+1] = g(\mathbf{w}[n], \mathbf{w}[n-1], \ldots \mathbf{w}[n-p], \mathbf{u}^0[n]) \tag{18}$$

where $\widehat{\mathbf{w}}^{\infty}[n+1]$ represents the estimate of the crack front due to the *n*-th block at a temporal resolution of 1 cycle and infinite mesh resolution and $\mathbf{u}^0[n]$ represents the load block at the coarsest temporal and spatial resolution. In what follows, $\widehat{\mathbf{w}}^j[k]$ represents the crack front due to the *k*-th block and a resolution level *j*. The discretization level index *j* ranges from 0 to ∞, where a level 0 implies the coarsest resolution and a level ∞ implies the finest resolution.

In the same manner as was presented previously, the evolution of the corrected crack front can be modeled as a non-linear function of previous crack shape and loading history:

$$\widehat{\mathbf{w}}^{\infty}[n+1] = \mathcal{GP}(\mathbf{w}[n], \mathbf{w}[n-1], \ldots \mathbf{w}[n-p], \mathbf{u}^0[n]) \tag{19}$$

Given an initial crack $\mathbf{w}[0]$ and a load history $L_k$ of $n$ load blocks, the objective is to predict the corrected crack fronts $\widehat{\mathbf{w}}^{\infty}[1], \widehat{\mathbf{w}}^{\infty}[2], \ldots \widehat{\mathbf{w}}^{\infty}[n]$. Prediction for entire load histories may be obtained by considering an iterated GP model in which crack front prediction from the previous stage is taken as an input in the next stage:

$$\widehat{\mathbf{w}}^{\infty}[n+1] = \mathcal{GP}(\widehat{\mathbf{w}}^{\infty}[n], \widehat{\mathbf{w}}[n-1], \ldots \widehat{\mathbf{w}}^{\infty}[n-p], \mathbf{u}^{0}[n]) \tag{20}$$

While the surrogate model prediction depends on the estimates of previous crack shapes at the highest level of discretization, its dependence on the load block is only at the coarsest level.

The evolution of an initial crack front, $C_0$ for load history $L = \{l_7, l_3, l_{11}, l_3\}$ may then be written as:

$$\widehat{\mathbf{w}}^{\infty}[1] = \mathcal{GP}(\mathbf{w}[0], l_7) \tag{21}$$

$$\widehat{\mathbf{w}}^{\infty}[2] = \mathcal{GP}(\widehat{\mathbf{w}}^{\infty}[1], l_3) \tag{22}$$

$$\widehat{\mathbf{w}}^{\infty}[3] = \mathcal{GP}(\widehat{\mathbf{w}}^{\infty}[2], l_{11}) \tag{23}$$

$$\widehat{\mathbf{w}}^{\infty}[4] = \mathcal{GP}(\widehat{\mathbf{w}}^{\infty}[3], l_3) \tag{24}$$

Thus the surrogate modeling technique for crack growth kinetics may be extended to account for the effects of spatial and temporal discretization. However, the surrogate model for crack growth with discretization requires estimates of the corrected fronts for each block. This contrast between the two models is shown in Table 3.5, where the training tables for first order uncorrected and corrected crack growth kinetics are shown.

Table 3.5: Training tables for surrogate modeling for crack growth analysis

| Without Correction | | | With Correction | | |
|---|---|---|---|---|---|
| $\mathbf{C}_k$ | $\mathbf{u}_k$ | $\mathbf{C}_{k+1}$ | $\mathbf{C}_k$ | $\mathbf{u}_k$ | $\mathbf{C}_{k+1}$ |
| $\mathbf{w}[1]$ | $\mathbf{u}[1]$ | $\mathbf{w}[2]$ | $\mathbf{w}[1]$ | $\mathbf{u}[1]$ | $\mathbf{w}^{\infty}[2]$ |
| $\mathbf{w}[2]$ | $\mathbf{u}[2]$ | $\mathbf{w}[3]$ | $\mathbf{w}^{\infty}[2]$ | $\mathbf{u}[2]$ | $\mathbf{w}^{\infty}[3]$ |
| $\mathbf{w}[3]$ | $\mathbf{u}[3]$ | $\mathbf{w}[4]$ | $\mathbf{w}^{\infty}[3]$ | $\mathbf{u}[3]$ | $\mathbf{w}^{\infty}[3]$ |
| $\vdots$ | $\vdots$ | $\vdots$ | $\vdots$ | $\vdots$ | $\vdots$ |
| $\mathbf{w}[L]$ | $\mathbf{u}[L]$ | $\mathbf{w}[L+1]$ | $\mathbf{w}^{\infty}[L]$ | $\mathbf{u}[L]$ | $\mathbf{w}^{\infty}[L+1]$ |

The non-linear evolution of crack front shapes as a function of discretization level must now be considered:

$$\mathbf{w}^{\infty}[i] = f(\mathbf{w}^{0}[i], \mathbf{w}^{1}[i], \mathbf{w}^{2}[i], \dots) \tag{25}$$

where $w^{j}[i]$ is the crack front for the *i*-th load block at the *j*-th level of resolution and can be modeled as a Gaussian process regression:

$$\mathbf{w}^{\infty}[i] = \mathcal{GP}_i(\mathbf{w}^{0}[i], \mathbf{w}^{1}[i], \mathbf{w}^{2}[i] \dots) \tag{26}$$

Thus for each load block, $u_i$ under consideration, a surrogate model is required to predict the corrected front, $\mathbf{w}^{\infty}[i+1]$ at the highest level of discretization. The training data for such a surrogate model consists of crack fronts $\mathbf{w}^{j}[i+1]$ at various levels of resolution *j* and is presented in Table 3.6. Note that while the crack shape at the highest resolution depends on the shape of the crack the coarsest resolution, for the construction of the model for corrected crack front of a given block, this remains constant for all the training points and may be thus be omitted from the regression. As a consequence, the corrected crack front for a given block is determined only as a function of the level of discretization.

Table 3.6: Surrogate model training at various resolutions

| $\mathbf{C}_k$ | $\mathbf{u}_k$ | $\mathbf{C}_{k+1}$ |
|---|---|---|
| $\mathbf{w}[i]$ | $\mathbf{u}^0[i]$ | $\mathbf{w}^0[i+1]$ |
| $\mathbf{w}[i]$ | $\mathbf{u}^1[i]$ | $\mathbf{w}^1[i+1]$ |
| $\mathbf{w}[i]$ | $\mathbf{u}^2[i]$ | $\mathbf{w}^2[i+1]$ |
| ⋮ | ⋮ | ⋮ |
| $\mathbf{w}[i]$ | $\mathbf{u}^d[\mathrm{i}]$ | $\mathbf{w}^d[i+1]$ |

For illustration, first the effect of temporal discretization will be considered. To exhibit this, a sample load block of 36,000 cycles will be corrected for temporal discretization. Four different levels of discretization were considered: 1) one block of 36,000 cycles, 2) two blocks of 18,000 cycles, 3) four blocks of 9,000 cycles, and 4) eight blocks of 4,500 cycles. For each test, the crack fronts were extracted using 3D FEA simulation. The crack front after each mesh test was then transformed into a latent space representation in order to estimate the corrected crack front. A surrogate model was constructed using crack representations to three levels of discretization (36000, 18000, and 9000) and the crack representation due to the eight blocks of 4500 cycles was retained as verification data. The surrogate model and the predictions at discretization levels of 4500 cycles and 1 cycle are shown in Figure 3.6. The predictions of the surrogate model are shown as red circles and the actual data points are shown as blue circles. A fair agreement between the prediction at the 4500 cycles and the corresponding observed value is noted.

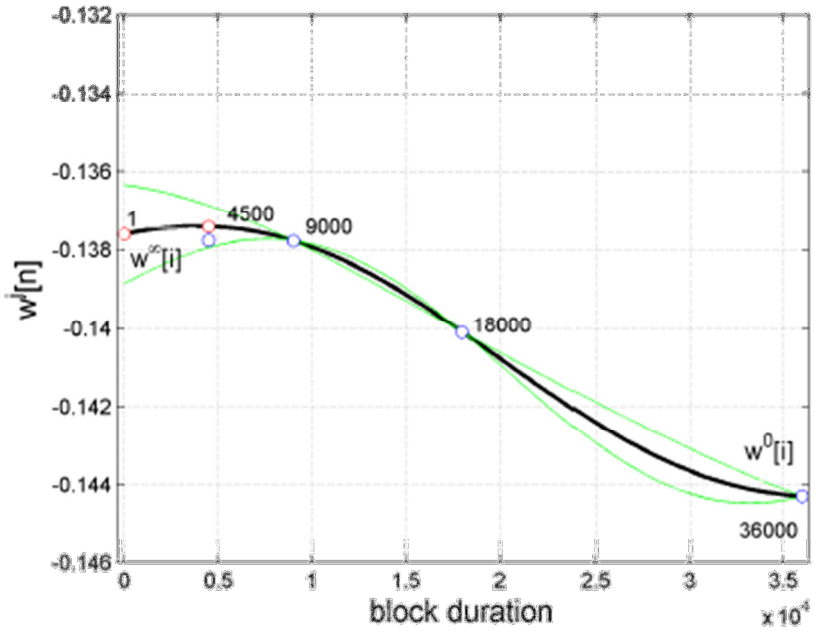


Figure 3.6: Estimation of corrected crack front with temporal discretization

The above discussion presents the estimation of corrected crack fronts for a given block; however, the kinetics of crack growth must be considered for entire load histories consisting of multiple load blocks. Extension of per-block corrected crack fronts to entire load histories is illustrated in Figure 3.7 for a three block history $(B_1, B_2, B_3)$ and a given initial crack front $C_0$. In the first step, the initial crack is independently subjected to the first load block at three different levels of discretization $B_1^0, B_1^1$, and $B_1^2$. The crack fronts resulting from these FEA evaluations are then employed to construct the surrogate model $\mathcal{GP}_1$, which is then used to predicted the corrected crack front at the highest level of discretization, $C_1^\infty$. This predicted crack front is then used as the input for the next step and is used to predict the corrected crack front due to load block $B_2$.

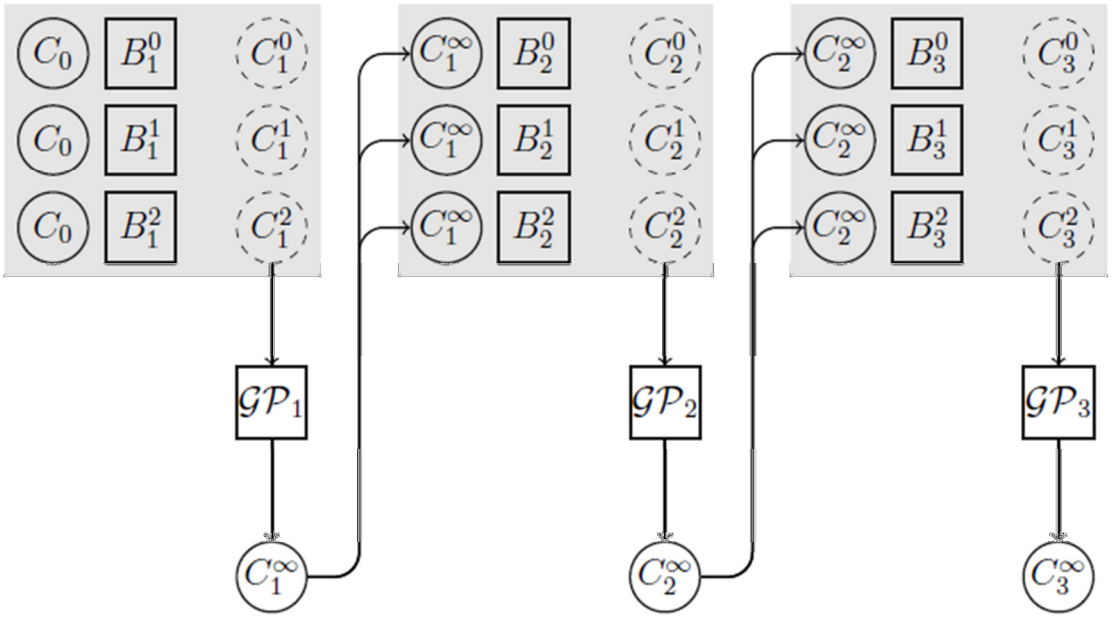


Figure 3.7: Estimation of discretization per block for a three block load history

Together, $C_0, C_1^\infty, C_2^\infty, \ldots$ represent the evolution of the corrected crack front and may thus be employed for any given load history. However, these estimates are based on expensive evaluations of crack shapes at various levels of resolution and are infeasible for direct use in a probabilistic analysis. Instead, in the proposed approach, such estimates are evaluated for a few training load histories and then used to construct the surrogate model described previously. This allows for efficient construction of a surrogate model that generalizes the non-linear relationship between the current crack shape and the effect of discretization due to a given load block.

### 3.5 Illustration of discretization error modeling

While the ultimate goal of discretization error analysis is to determine the combined effect of both temporal and spatial discretization, it is also important to understand the contributions that each type of discretization brings to the error in the final result of each FRANC3D simulation. Consequently, the effect of each type of discretization error will first be used separately to correct the crack fronts and then their combined affects will be analyzed. To this end, four load histories, each of 120,000 cycles total duration, were considered: $l_7, l_4, l_6, l_7; l_6, l_2, l_2, l_{14}; l_1, l_3, l_7, l_{13}$; and $l_8, l_{12}, l_4, l_{11}, l_{10}$. For each load block of a given load history, the corresponding corrected crack front can be estimated using the approach outlined in Figure 3.7. Three of the load histories were considered as training data, and one load history of four blocks was used for verification purposes.

Temporal discretization will be considered first. For each block of the training load histories, the training data was obtained by considering three different discretization levels: *d*, *d*/2, and *d*/4 (where *d* is the duration of the training block). The corrected crack front corresponds to duration $d = 1$. The surrogate model was constructed using the 12 data points from the training load histories as shown in Figure 3.8. In addition to the surface of the surrogate model, the training points and prediction points are also presented in Figure 3.8. In Figure 3.9, the response of the surrogate models at the verification blocks is converted to the original data space and compared with the corresponding block estimates of corrected fronts for the verification blocks which form the baseline values. As seen in the figure, the uncorrected crack front which corresponds

to $C^0[i]$, underestimates crack growth due to the use of a conservative estimate of the equivalent stress. The prediction of the surrogate model is similar to the estimates of the corrected crack fronts using expensive 3-D FEA simulations.

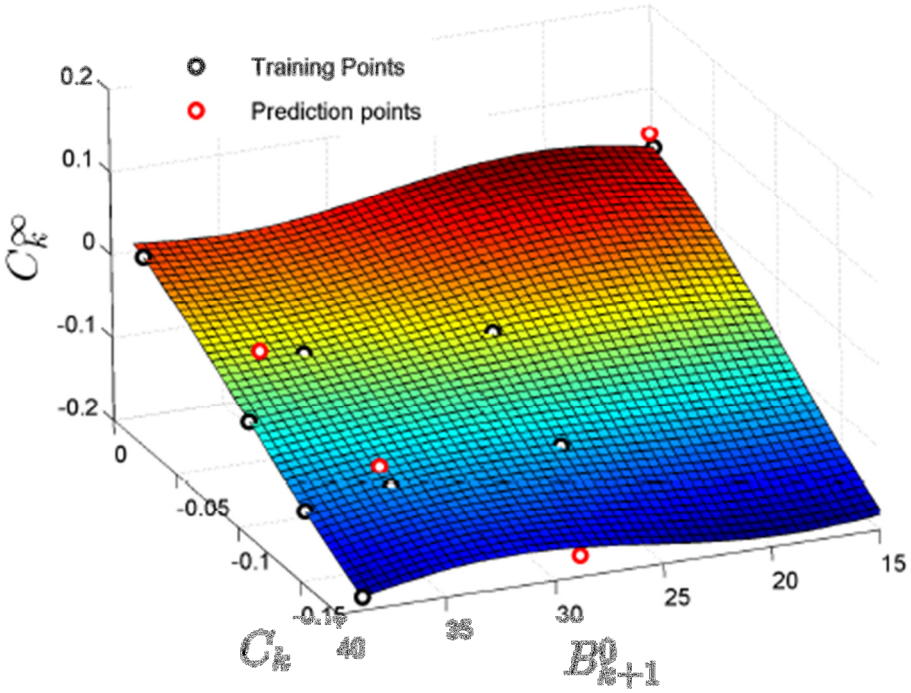


Figure 3.8: Temporal discretization surrogate model

For illustration of the spatial discretization problem, a detailed description of the local mesh in the FEA simulations must be provided. In order to accurately analyze the stress region along the crack front while maintaining computational efficiency, FRANC3D implements the use of a crack tube around the crack front. The crack tube is utilized so that remeshing can be

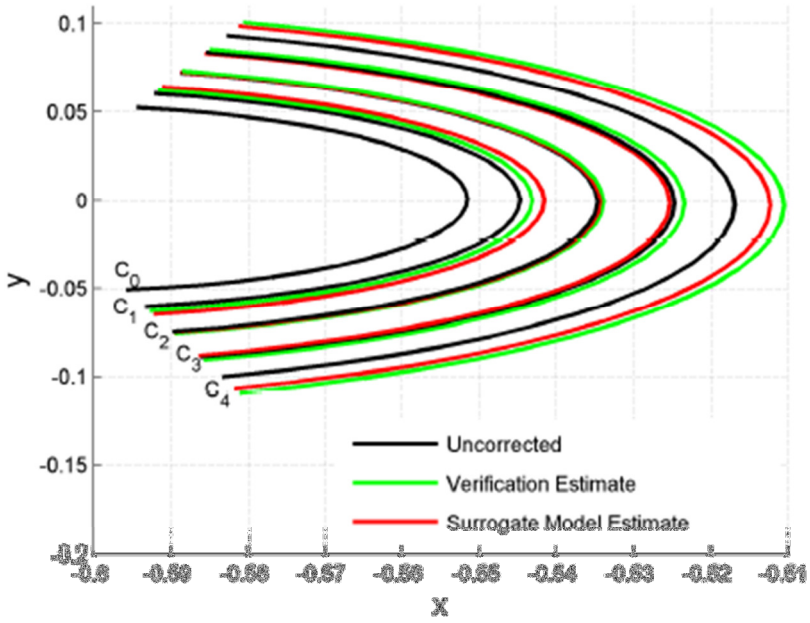


Figure 3.9: Crack growth predictions considering temporal discretization

performed quickly. Therefore, refinement of the mesh is limited to a few parameters which control the size of the crack tube. Since the number of circumferential elements around the crack tube is limited due to constraints related to the FEA solver, the number of rings around the crack front is chosen as the meshing parameter. For each block of the training load histories, the training data was obtained by considering three different discretization levels: 5, 10, and 20 rings. With this nomenclature, the corrected crack front corresponds to an infinite number of rings. Since the using the surrogate model to predict at infinity is not feasible, the reciprocal of the number of rings was used for the training of the model so that the value corresponding to the corrected crack front is zero. The surrogate model was constructed using the same 12 training points from the temporal demonstration and is presented in Figure 3.10. In Figure 3.11, it can be seen that the error in crack growth prediction caused by spatial discretization is less significant that the error due to temporal discretization.

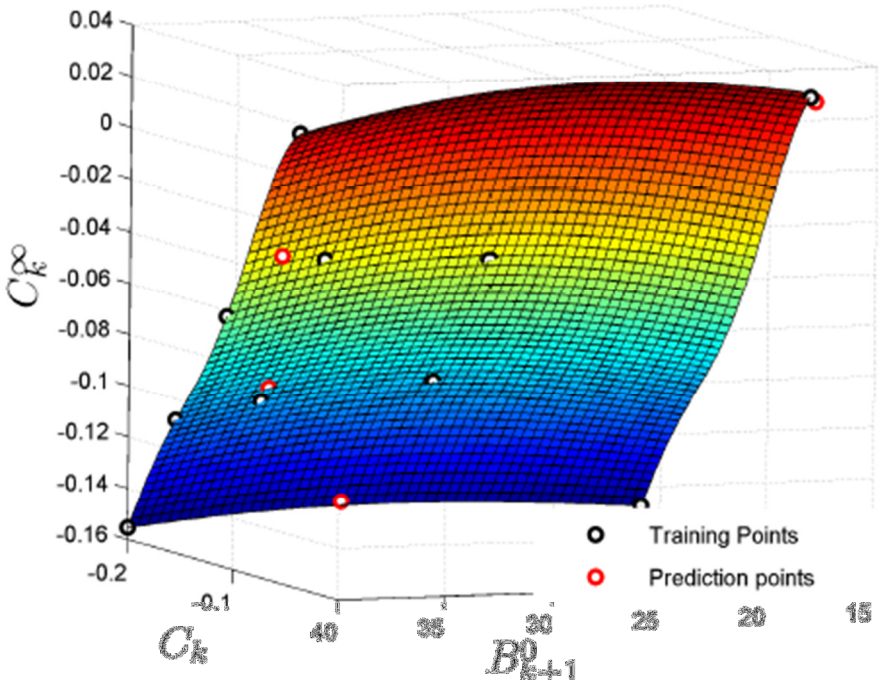


Figure 3.10: Spatial discretization surrogate model

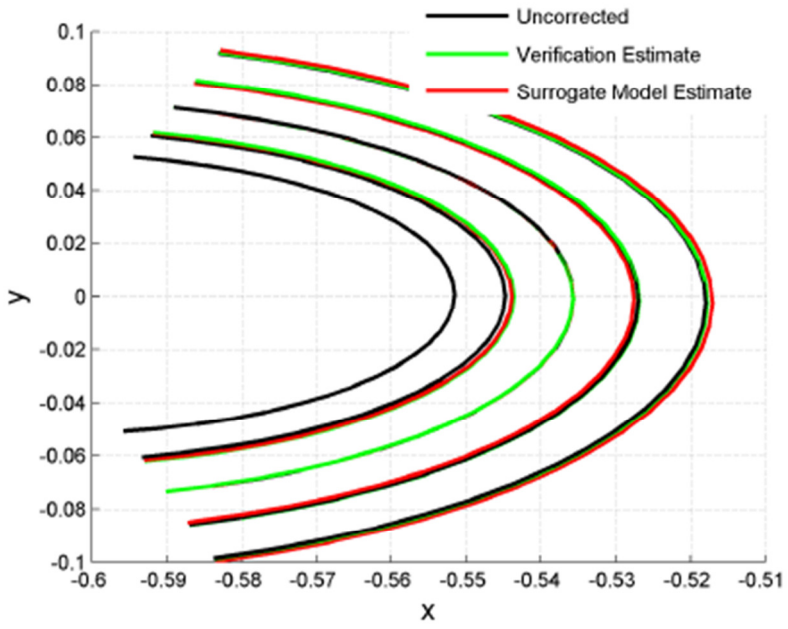


Figure 3.11: Crack growth predictions considering spatial discretization

Finally, the combined effect of both spatial and temporal discretization can be considered. For each block of the training load histories, the training data was obtained by considering three different discretization levels: 1)5 rings and 1 block of *d* cycles, 2)10 rings and 2 blocks of *d*/2 cycles, and 3)20 rings and 4 blocks of *d*/4 cycles. The corrected crack front corresponds to a spatial resolution of infinite rings and a temporal resolution of *d* blocks of 1 cycle. Similar to the previous two demonstrations, the 12 training data points are used to construct the surrogate model which is presented in Figure 3.12. The corrected crack front curves are compared against the uncorrected predictions for the verification load history in Figure 3.13.

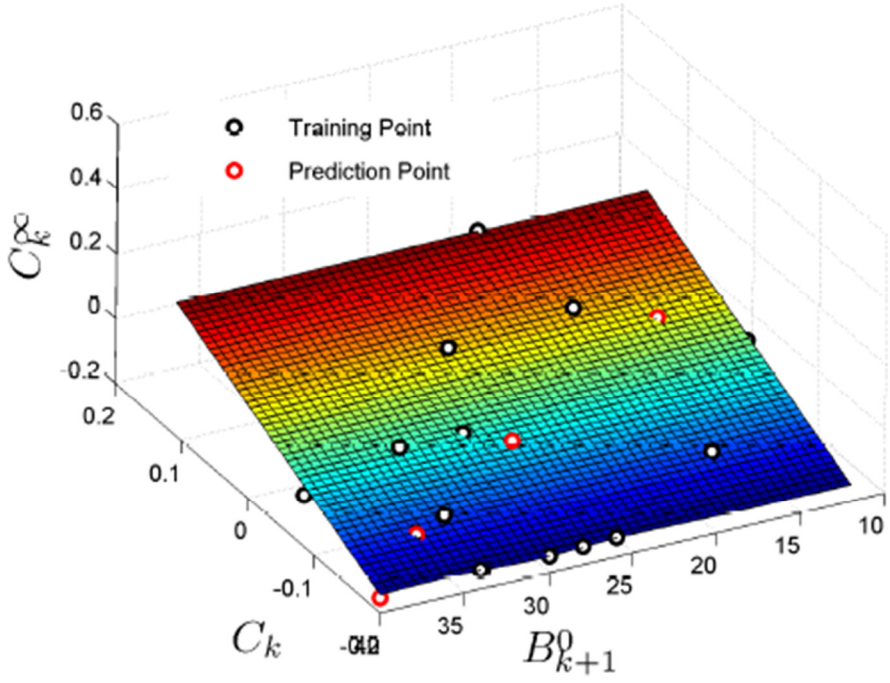


Figure 3.12: Spatiotemporal discretization surrogate model

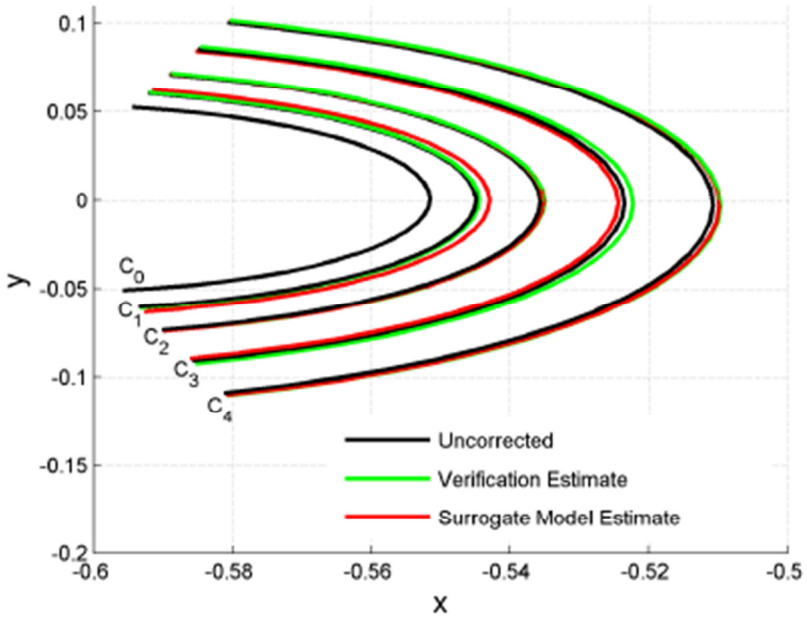


Figure 3.13: Crack growth predictions considering combined spatiotemporal discretization

### 3.6 Conclusion

An approach was proposed for the construction of surrogate models of non-planar cracks for use in crack growth analyses for life prediction and uncertainty quantification. Development of this methodology is necessitated by the demand for computationally cheap albeit reasonably accurate estimates of crack growth for failure prognosis. The proposed method is illustrated using a cylindrical component that is similar to rotorcraft masts.

A non-parametric representation of the crack fronts is employed that allows for the development of surrogate models which model the non-planar crack growth kinetics as the kinetics of freely deformable space curves. The principal steps of the proposed method include representation of crack fronts in a fixed dimension, dimensionality

reduction, and modeling of non-linear kinetics. The non-parameterized crack representation is then employed to model the effects of spatial and temporal discretization in 3-D finite element analysis of non-planar crack growth by modeling both the block estimates of the corrected fronts and the kinetics of crack growth in the low dimensional crack representation space. The proposed methods are illustrated using data from FEA simulations of non-planar crack growth under variable amplitude variable duration multi-axial loading.

# CHAPTER 4

# IDENTIFICATION OF ERRORS IN FATIGUE EXPERIMENTATION AND BAYESIAN MODEL PARAMETER CALIBRATION

## 4.1 Introduction

Several models have been developed to predict crack propagation in a given mechanical component. Many of these models have already undergone treatments to understand how uncertainty from the input parameters can be passed through to determine a realistic distribution for the predicted crack growth increment [32]. Due to its simplicity and versatility, the Paris law crack growth model [26] is the focus of several such studies. Paris law is an effective tool that can determine a crack growth rate ($da$ / $dN$) for a given material and stress intensity factor range. The stress intensity factor range ($\Delta K$) is determined based on the geometry of the component, the initial flaw size, and the applied loading. The Paris law relates these parameters as:

$$\frac{da}{dN} = C\ \Delta K^m \tag{27}$$

where $C$ and $m$ are material constants that can be obtained from physical experiments. Typically when uncertainty is considered in the fatigue crack growth process, it is collected within the material properties $C$ and $m$.

Basic guidelines for experimental error reduction and measurement are provided by the ASTM [33], but in general, experimental uncertainty is usually quantified using data from multiple specimens. Using that approach, the uncertainty in the measured

quantity, be it material properties or crack growth rates, is attributed to variability across the multiple tested specimens [34].

The methodology presented here proposes a technique using Bayesian model parameter calibration to quantify uncertainty in material properties as well as sources of error in the experimentation. The Bayesian model parameter calibration technique utilized in this chapter is based on the Kennedy and O'Hagan (KOH) framework [35]. The KOH framework was developed for the purpose of calibrating computer models under multiple sources of uncertainty. The framework includes a discrepancy term in order to account for the difference between the model prediction and observed data. The discrepancy is an important parameter in calibration because without its inclusion, the calibration may provide inaccurate distributions for the model parameters. The need for a proper understanding of this "discrepancy term" is outlined in [36].

By attributing the uncertainty to a variety of sources, a more realistic understanding of the uncertainty in the material parameters of intent can be achieved. Such an approach also yields some insight into what measures can be taken to reduce the uncertainty in the crack growth model's prediction. Some sources of uncertainty are irreducible, such as the natural variability in material properties such as $C$ and $m$. The reducible uncertainty sources are various measurement errors and the errors in experimental load application. The calibration can also be used to demonstrate which of these sources has the largest effect on the crack growth prediction uncertainty.

It is important to have a complete understanding of the experimental process before the sources of uncertainty can be identified. Measurement technique and choice of measurement quantity affect the errors in test setup, measurement acquisition, and data

analysis [37]. In the literature, Beretta and Murakami [38] investigated the estimation of extreme defect size for suitable fatigue strength prediction. Some known contributors to experimental uncertainty are defects in the material [39] and improper load and displacement measurement [40].

In this chapter, compact tension fatigue experiments will be used to evaluate the material properties $C$ and $m$ to be used in a Paris law fatigue crack growth prediction. The individual sources of uncertainty in the fatigue experiments will be identified. The Bayesian model parameter calibration will then be performed to estimate the posterior probability density functions of the model parameters.

## 4.2 Experimental setup

The material used for the experimental testing presented here is Aluminum 7075 due to its common application in the aircraft industry [41]. The compact tension specimens used for the testing are designed in accordance with ASTM E 647-08. The yield strength of Aluminum 7075 is 69,000 psi (475 MPa). A sample photo of one the specimens is shown in Figure 4.1. A V-shaped notch is machined into the specimen which is further sharpened using a razor. A thickness of ½" along with a length of 2.5" and a width of 2.4" are the geometric parameters used for these specimens. The diameter of 0.5" (with an acceptable pin-to-hole clearance) was used for the gripping holes. The pre-crack has a minimum length of 0.125" for each specimen as prescribed in ASTM E 647-08. Twelve specimens are tested for the purpose of repeatability. Clevis grips are designed in accordance with ASTM E 647-08 and are used to mount the specimens. A schematic diagram of the test assembly showing the Clevis grips and the compact tension

specimen is shown in Figure 4.2. An MTS 810 test machine is used for the mechanical testing of the specimens. The experimental parameters which determine the fatigue crack growth rate include loading amplitude (as a percentage of yield strength of aluminum), nature of applied stress and choice of stress-time modes. The nature of the applied stress can be axial, flexural or torsional or a combination of these modes. This experiment considers only axial stresses. The commonly used time modes include reversed constant amplitude, repeated constant amplitude and random cycling. In order to reduce the number of sources of experimental uncertainty, a repeated constant amplitude stress-time mode is chosen over random cycling. The load was applied in the form of displacements as it is easier to control than applying forces. The specimen is subjected to fatigue loading until failure. In order to capture crack initiation, crack propagation and final failure, an imaging setup is used. The crack growth as a function of number of cycles is determined using the imaging setup.

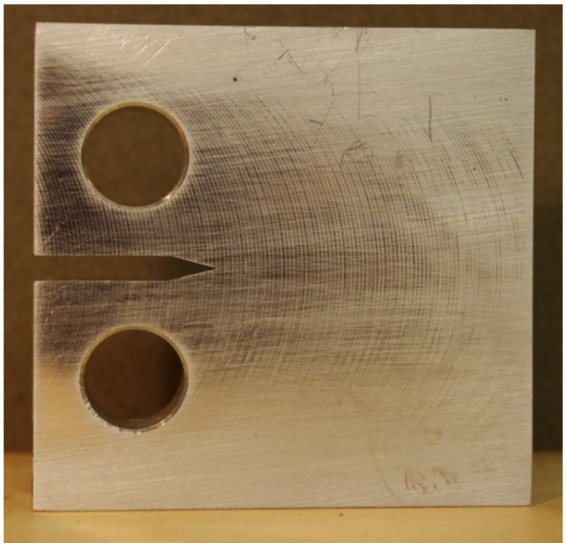

Figure 4.1: Compact tension specimen composed of 7075 aluminum

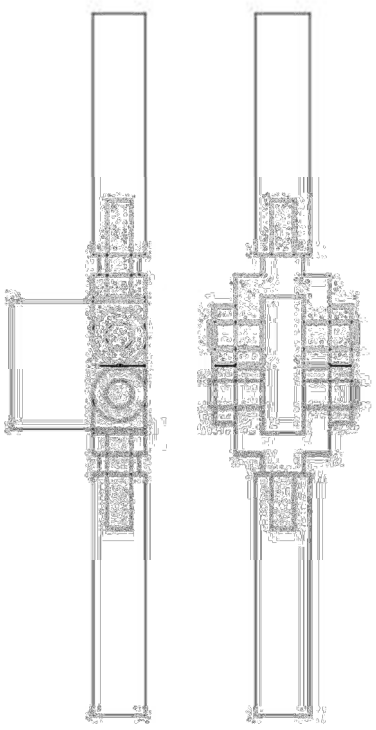

Figure 4.2: Schematic of experiment assembly: The clevis grips are shown holding the compact tension specimen.

The imaging set-up consists of a digital single lens reflex (SLR) camera, two infrared (IR) light emitting diodes (LEDs) and a green screen to capture the images. The IR LEDs are used to remotely trigger the digital camera to capture images at regular intervals of time. This imaging is carried out until the failure of the compact tension specimen. The crack growth is measured from the images using digital image processing.

### 4.3 Sources of error in fatigue experiments

The sources of error in fatigue experiments can be broadly categorized into two types: pre-test errors and measurement errors. Pre-test errors are those that are inherently

present in the system such as material properties, geometry of the test specimen, load alignment, etc. The measurement errors are those that affect the observation of the data such as imaging errors, machine calibration, etc. The errors in the experimental outcome caused by material defects, specimen geometry and crack tip sharpness have been discussed in detail in [39] and are not considered in the work presented here. Since no quantitative data from the experimentation was obtained for these parameters they have been excluded from the work presented here. A more detailed experimentation procedure could be adopted to quantify these identified but unaccounted for sources of uncertainty.

One significant source of error that was identified during the experimental study was alignment error. Alignment errors include errors due to specimen alignment, fixture to specimen contact friction and gripping pressure. Misalignment of the specimen to the fixture and/or fixture to the grips can lead to non-symmetric cracking especially close to the threshold values. The fixture and the specimen should be centered with respect to the loading grips in order to ensure accurate load transfer. The loading axis has to coincide with the central axis of the specimen in order to ensure that the load transferred to the specimen is indeed the load measured. In the case of fatigue experiments, the fixture must be designed to allow for smooth motion without friction. It is important to choose materials for the fixture that transfer load without undergoing fatigue damage themselves. A suitable gripping pressure (5000 psi) was chosen to prevent damage to the fixtures and to allow for smooth load transfer. The direct measurement of alignment errors poses a unique difficulty.

One method for quantification of the alignment error is to measure the variation in the position of specific points on the specimen during the testing. The variation in the

position of a point on the specimen can be tracked using image processing. This variation should be vertical and there should be no horizontal motion. Any changes in the horizontal direction indicate the misalignment in the specimen. While this can be used to track misalignment, it will not be possible to control alignment using this technique.

Misalignment in the experimental specimen can cause increased load value due to the moments that are induced. Kandil and Dyson [42, 43] discuss the effect of misalignment on uniaxial low cycle fatigue specimens. Misalignment in the experimental fixture is calculated by studying the relative horizontal and vertical motion of the red dots in Figure 4.3. Images of the specimen along with the red dots are taken at various intervals of time. The red dots are then tracked to determine the center and radius of the circular region enclosed by them. While the vertical motion is due to the movement of the specimen, the horizontal motion is due to misalignment in the loading fixture. The boundaries of the circular dots are traced using MATLAB's [44] image processing capabilities as shown in Figure 4.3. The variation of the center of the circular dot in the X and Y direction and the variation of the radius of the red dot are measured as shown in Figure 4.3. This graph demonstrates the relative variation of the center of the red dot at the top left of the specimen.

From Figure 4.4, it can be seen that the variation in the radius of the red dot obtained by the tracking procedure is negligible. Finite element analysis was implemented to evaluate the effect that the misalignment seen in the experimentation (variation in the X-direction) can have on the stress intensity factor at the crack tip. The results from this analysis indicate that the misalignment can alter the stress intensity factor by up to 9%.

Testing equipment calibration errors are quantified by comparing the load and displacement data produced by the equipment used for the current test vs. a standard set of data produced by the manufacturer. It is common that with frequent use, most testing equipment loses calibration over time. The comparison is performed in the case of the MTS 810 machine to quantify the error in the application of a prescribed load. The variation in calibration errors for axial load and axial displacement for the experiments considered in this chapter are shown in Figure 4.5. The charts show the variation in error as a function of absolute displacements and loads.

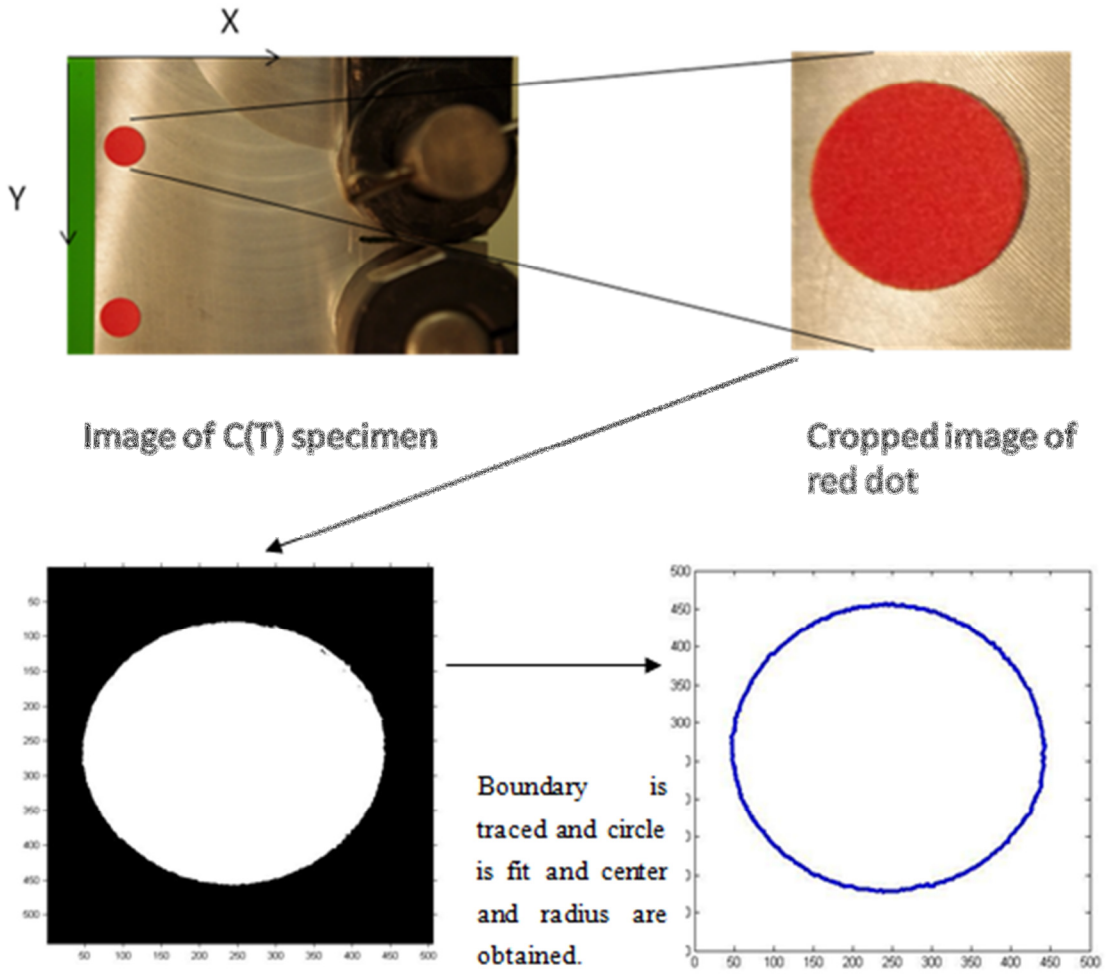


Figure 4.3: Procedure for tracking red alignment dots using MATLAB image processing

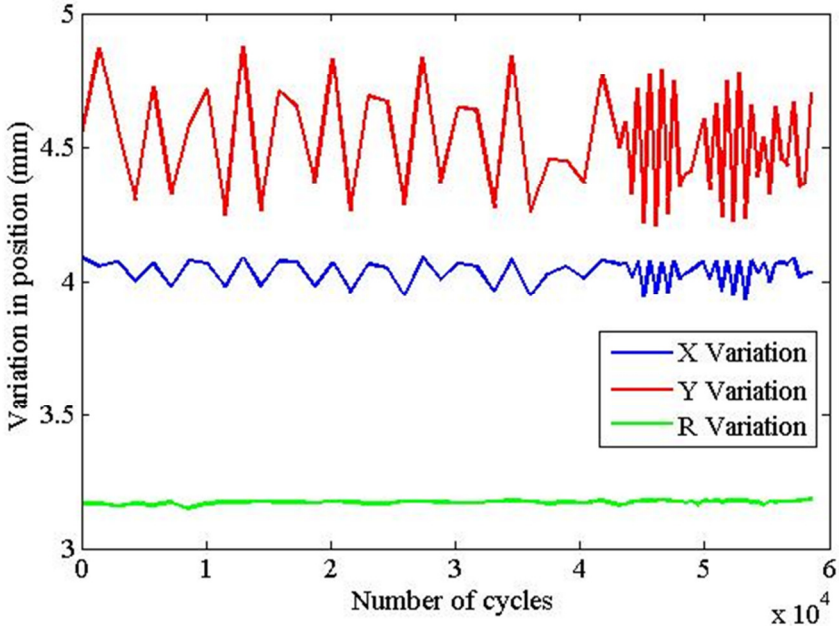


Figure 4.4: Dot tracking to measure position variation: Variation in the x and y directions as well as the dot radius dimension are presented.

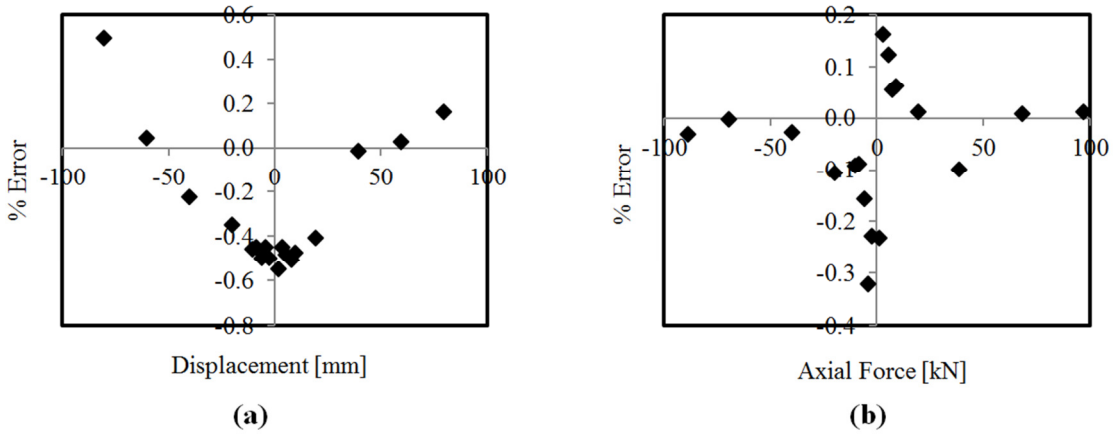


Figure 4.5: Calibration errors for MTS equipment: Error for both displacement-prescribed loading (a) and force-prescribed loading (b) are shown.

The final significant experimental error considered in this work is imaging/observation error. In this case, imaging errors are caused due to resolution concerns resulting from the use of digital imaging. Since digital imaging is used to

measure the crack size for each specimen, errors are incurred due to the image quality of each photograph. In general, this imaging error depends on the quality and proper utilization of the imaging equipment used and the software used to process the images. For the work presented here, an error of +/- 10 pixels is used for the imaging error in the digital photographs. A second observation error is present due to the necessary synchronization of each image with a specific load cycle during the experimentation. Since there is obviously some lag between the imaging trigger and the MTS software, there is some error in this synchronization. The frequency at which the load is applied is 10 Hz; therefore, the error in the cycle count is +/- 10 cycles.

### 4.4 Bayesian model parameter calibration

Consider a general model shown in Figure 4.6. The model is a function of inputs ($\boldsymbol{x}$) and model parameters ($\boldsymbol{\theta}$). The difference between $\boldsymbol{\theta}$ and $\boldsymbol{x}$ is often difficult to determine but in this framework the model inputs, $\boldsymbol{x}$, will be considered to be observable quantities (either stochastic or deterministic) such as loading and model parameters, $\boldsymbol{\theta}$, are not observable (such as crack growth parameters) and are therefore the objective of the calibration procedure. The model output $y_m$ should be a quantity of the same meaning as $y_d$, observable physical quantity, so that a direct comparison can be made. The error in the observation of $y_d$ is often represented as a zero-mean Gaussian random variable $\varepsilon_{obs}$ with a variance $\sigma_{obs}^2$. The alignment error is actually an error that would typically affect the mean value of the observed quantity making the zero-mean Gaussian assumption incorrect, but for this analysis the alignment error was applied to the model prediction to maintain the assumption.

The inputs, outputs, model parameters and various errors can be connected through a directed acyclic graph known as a Bayesian network. The Bayesian network is a collection of nodes and directed edges where each node represents an uncertain parameter and the edges represent the conditional probability links between the nodes [45, 46]. Bayes theorem can be used to calibrate the unknown model parameters on the observation data, $D$, of $y_m$.

$$\pi(\boldsymbol{\theta}, \sigma_{obs}, \sigma_m|D) = \frac{\mathcal{L}(\boldsymbol{\theta},\sigma_{obs},\sigma_m)\,\pi(\boldsymbol{\theta})\,\pi(\sigma_{obs})\,\pi(\sigma_m)}{\int \mathcal{L}(\boldsymbol{\theta},\sigma_{obs},\sigma_m)\,\pi(\boldsymbol{\theta})\,\pi(\sigma_{obs})\,\pi(\sigma_m) d\boldsymbol{\theta}\, d\sigma_{obs} d\sigma_m} \quad (28)$$

$$\mathcal{L}(\boldsymbol{\theta}, \sigma_{obs}, \sigma_m) \propto \Pr(D|\boldsymbol{\theta}, \sigma_{obs}, \sigma_m) \quad (29)$$

where:

$\pi(\boldsymbol{\theta}), \pi(\sigma_{obs})$ and $\pi(\sigma_m)$ = Prior PDFs of $\boldsymbol{\theta}, \sigma_{obs}$ and $\sigma_m$ respectively

$\pi(\boldsymbol{\theta}, \sigma_{obs}, \sigma_m|D)$ = Joint posterior PDF of $\boldsymbol{\theta}, \sigma_{obs}$ and $\sigma_m$

$\mathcal{L}(\boldsymbol{\theta}, \sigma_{obs}, \sigma_m)$ = Joint likelihood function of $\boldsymbol{\theta}, \sigma_{obs}$ and $\sigma_m$

$\Pr(D|\boldsymbol{\theta}, \sigma_{obs}, \sigma_m)$ = Probability of observing the data given $\boldsymbol{\theta}, \sigma_{obs}$ and $\sigma_m$

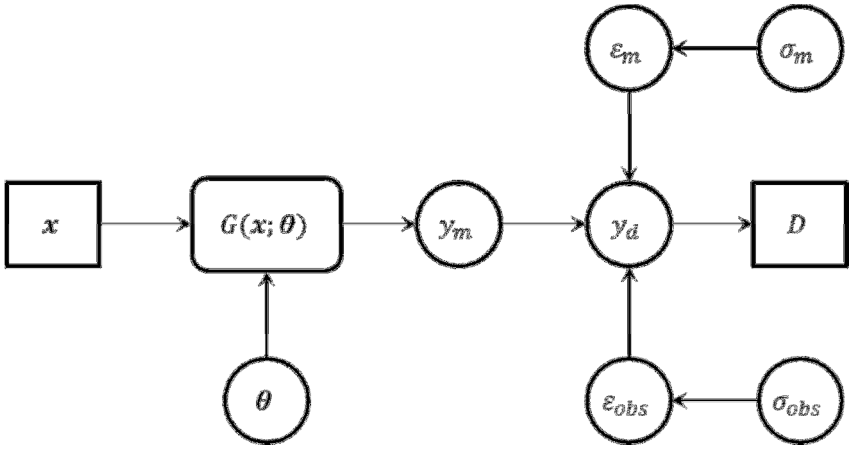


Figure 4.6: Illustrative diagram for general model.

The observation data point D is a random realization of $y_d$. The data realization can be represented then as:

$$y_d = y_m + \varepsilon_{obs} + \varepsilon_m \tag{30}$$

In the simplest case, $y_m$ is deterministic for given values of $\boldsymbol{\theta}$ and $\boldsymbol{x}$, and $y_d$ is deterministic for given values of $y_m$ and $\sigma_{obs}$. For this case of deterministic $y_d$ and $y_m$, $\pi(y_m|\boldsymbol{\theta}, \sigma_{obs}) = 1$ if $y_m = G(\boldsymbol{x}; \boldsymbol{\theta})$, and 0 elsewhere. Also, $\pi(y_d = D|y_m, \varepsilon_{obs}) = 1$ if $y_m + \varepsilon_{obs} = D$, and 0 elsewhere. $\pi(\varepsilon_{obs}|\sigma_{obs})$ is assumed to be $N \sim (0, \sigma_{obs})$ and evaluated at $\varepsilon_{obs}$. Based on these observations, the joint likelihood function of $\boldsymbol{\theta}$ and $\sigma_{obs}$ is derived to be:

$$\mathcal{L}(\boldsymbol{\theta}, \sigma_{obs}, \sigma_m) \propto \int \pi(y_d = D|y_m, \varepsilon_{obs}, \varepsilon_m)\, \pi(y_m|\boldsymbol{\theta}, \boldsymbol{x})\, \pi(\varepsilon_{obs}|\sigma_{obs}) \pi(\varepsilon_m|\sigma_m)\, \pi(\boldsymbol{x})\, dy_m\, d\varepsilon_{obs}\, d\varepsilon_m\, d\boldsymbol{x} \tag{31}$$

Based on the assumptions mentioned above, the previous equation can be simplified to:

$$\mathcal{L}(\boldsymbol{\theta}, \sigma_{obs}, \sigma_m) \propto \int \pi(y_d = D|\boldsymbol{\theta}, \boldsymbol{x}, \varepsilon_{obs}, \varepsilon_m)\, \pi(\boldsymbol{x})\, d\boldsymbol{x} \tag{32}$$

If observation data is available for multiple inputs, $\boldsymbol{X_d}$, the formulation can be modified to include these other observations by making $\boldsymbol{y_d}$ a random vector with a multivariate Gaussian distribution and the observation $\boldsymbol{D}$ are random realizations of the $\boldsymbol{y_d}$.

In the simplest case where the observation error and the model discrepancy are combined, the likelihood calculation can be simplified using a FOSM (First order second moment) [4] approximation of $\mu_{ym}$ and $\sigma_{ym}^2$. Then, if normality is assumed, the variance caused by $y_m$ can be added to the $\sigma_{obs}$ by

$$\sigma_{ovr} = \sqrt{\sigma_{ym}^2 + \sigma_{obs}^2} \tag{33}$$

The joint likelihood function of $\boldsymbol{\theta}$ and $\sigma_{obs}$ can now be written to account for these two modifications:

$$\mathcal{L}(\boldsymbol{\theta}, \sigma_{ovr}) \propto \int \pi\left(\boldsymbol{y_d} = \boldsymbol{D} \middle| \mu_{ym}, \varepsilon_{ovr}\right) \pi\left(\mu_{ym} \middle| \boldsymbol{\theta}, \boldsymbol{X_d}\right) \pi(\varepsilon_{ovr} | \sigma_{ovr}) \, \pi(\boldsymbol{X_d}) \, d\mu_{ym} \, d\varepsilon_{ovr} \, d\boldsymbol{X_d} \tag{34}$$

### 4.5 Implementation of Bayesian calibration

The Bayesian network for the problem of concern in this chapter is presented in Figure 4.7. The calibration parameters are $\sigma_m, \sigma_N, \sigma_{a0}, C, m, \Delta P,$ and $\rho$ where $\sigma_{mf}$ is the model form error between the model output and the actual crack growth, $\sigma_N$ is the error in the observation of the cycle count, $\sigma_{a0}$ is the observation error in the imaging process, $C$ and $m$ are the Paris law parameters, $\Delta P$ $(P_{max} - P_{min})$ is the applied load which includes variability caused by test machine calibration, and $\rho$ is the error due to the alignment of the pins in the loading apparatus. Observations of $a_d$ (the actual crack length) are available at multiple values of $\mu_{a0}$ (mean initial crack length) and $\mu_N$ (mean duration of loading). The prior distributions used in the framework for the calibrated parameters are assumed to be uninformed (uniform distributions based on general information gained during the testing process) for the purposes of demonstration. For most of the parameters ($\sigma_N, \sigma_{a0}, C, m, \Delta P,$ and $\rho$) the uniform distributions are located simply between the bounds outlined in Section 4.2, but the sampling of the final parameter, $\sigma_{mf}$, is only limited to being a positive value so that the likelihood calculation

can be performed. More informed priors will be used in a later demonstration to emphasize the importance of prior knowledge on the calibration technique. The likelihood function, as discussed in the previous section and the relationship between $a_d$ and $a_m$ is based on the Paris law crack growth model.

$$\mu_{am} = a_0 + C\,\Delta K^m * N \tag{35}$$

$$a_d = \mu_{am} + \varepsilon_m \tag{36}$$

where $N$ is a normally distributed random variable with a mean, $\mu_N$, and standard deviation, $\sigma_N$, $a_0$ is also normally distributed with mean, $\mu_{a0}$, and standard deviation, $\sigma_{a0}$, and $\epsilon_{obs}$ is normally distributed with a mean of 0 and a standard deviation of $\sqrt{\sigma_{obs}^2 + \sigma_{am}^2}$, $C$ and $m$ are the Paris law parameters, $\mu_{am}$ is the mean model prediction, $a_d$ is an experimental observation, $\Delta K$ is the stress intensity factor range, and $\varepsilon_m$ is the model form error.

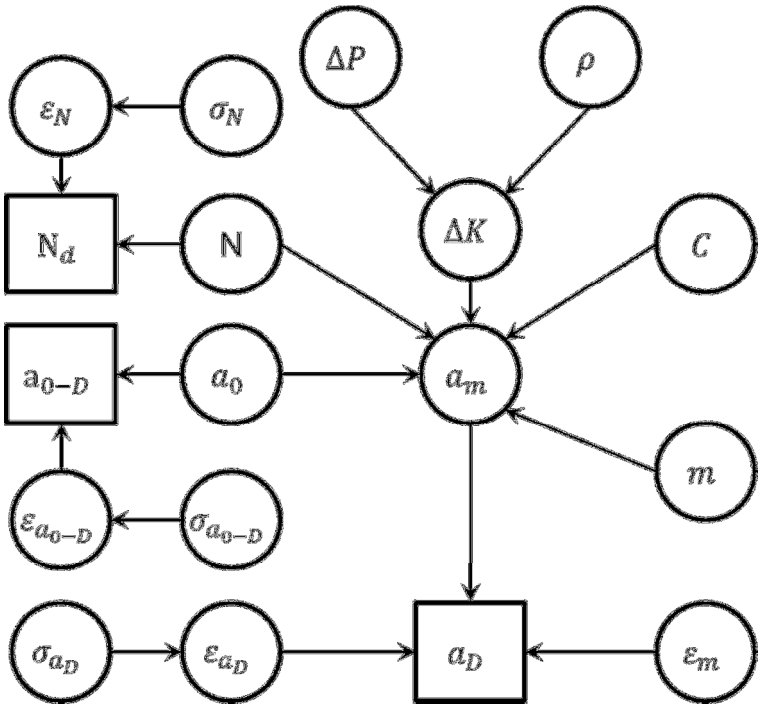


Figure 4.7: Bayes Network for CT specimen crack growth.

In typical uncertainty analyses of fatigue crack growth experiments, a linear regression is performed on $da/dN$ versus $\Delta K$ data and it is assumed that the parameters $C$ and $m$ are normally distributed. In Gurney [47], it is shown that the natural logarithm of the parameter $C$ is linearly related to parameter $m$ and therefore the uncertainty can be tracked using only the $m$ parameter. While Cortie and Garrett [48] demonstrated that it is inappropriate to constrain the values of the $m$ parameter in this manner, it remains a simple and effective means to monitor the two parameters and is therefore still occasionally used in practice.

To demonstrate the effect that uninformed experimentation can have on the Paris parameters, distributions for Paris law parameters that are assumed from literature values [49] are shown in Figure 4.9 and then compared to the calibrated values using the proposed methodology. Figure 4.8 presents the $da\ /\ dN$ vs. $\Delta K$ data for six of the fatigue specimens that were tested and will subsequently be used for calibration.

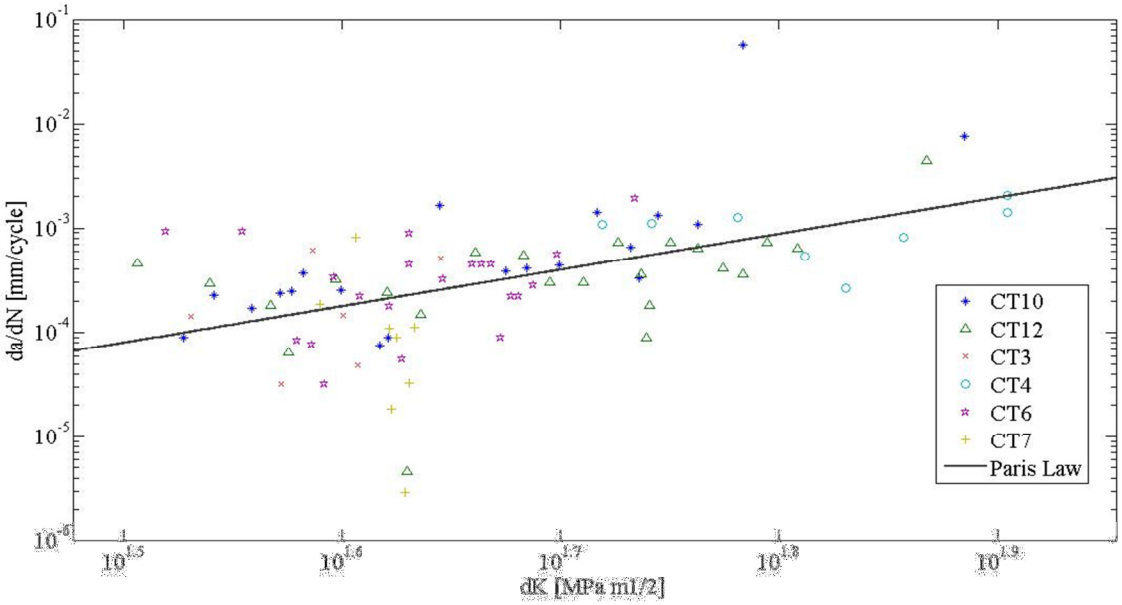


Figure 4.8: $da\ /\ dN$ vs $dK$ plot for CT specimens.

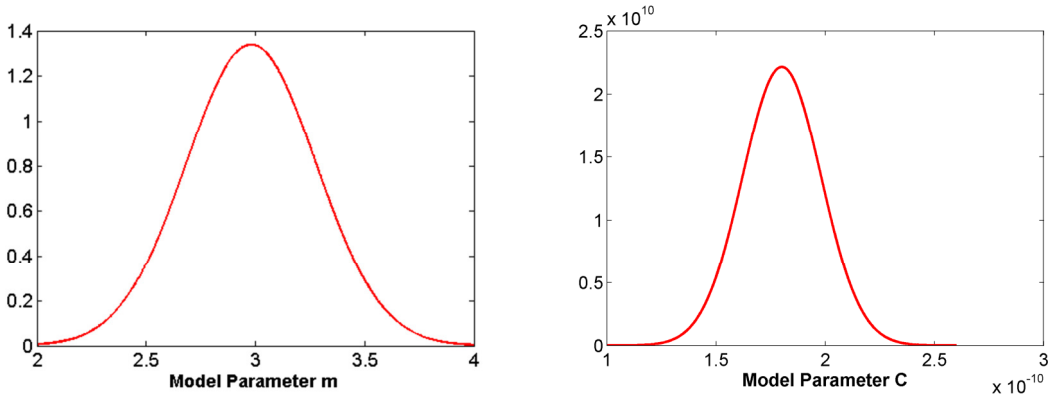


Figure 4.9: Prior Distributions of $C$ and $m$ parameters

Figure 4.10 shows the posterior distributions for the $C$ and $m$ parameters when the simplest Bayesian calibration approach is employed. A direct comparison of these two sets of distributions is useful. This is because the distributions of the parameters found in Figure 4.10 are conditioned upon the results of the calibration of all of the other parameters that were calibrated during the analysis. Even if the distributions are not directly comparable, it is still important to note the shape and location of the distributions in Figure 4.10 and how they differ from those in Figure 4.9. One particular item of note is the posterior distribution of parameter $C$ in Figure 4.10a and its seemingly lognormal form.

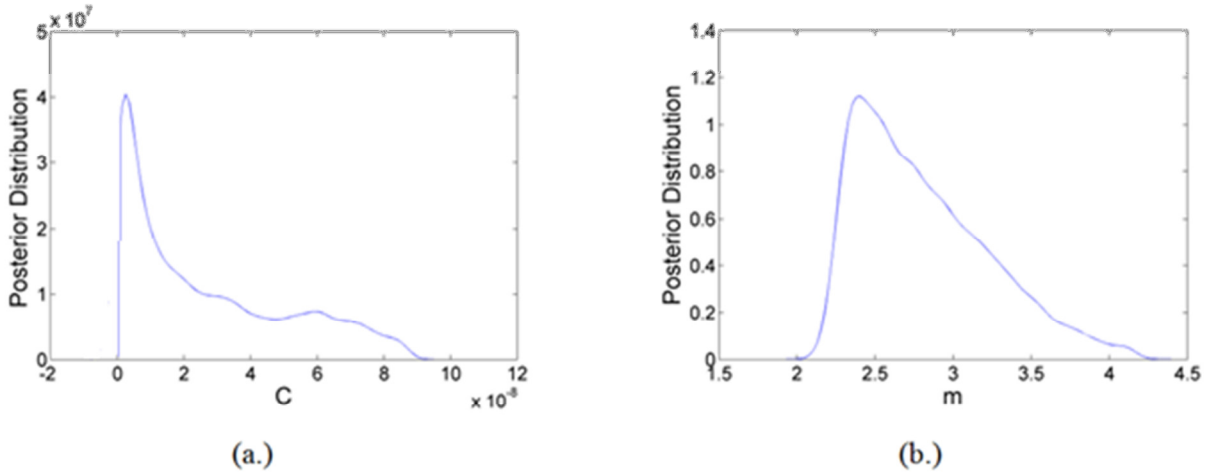


Figure 4.10: Posterior distributions of $C$ and $m$ parameters calibrated using the Bayesian model parameter calibration technique.

The posterior distributions for the other parameters that were calibrated are displayed in Figure 4.11. Some of these distributions do not possess a definitive shape which could be caused by two issues. Once issue could be that the problem is under-constrained (which is true in this instance) or the likelihood calculation is not particularly sensitive to the parameter in question meaning that as the parameter is sampled, the changes in its value do not significantly affect the likelihood calculation. Since it is known that the problem is under-constrained in this case, that issue will be addressed now. The first step towards a more constrained calibration is the use of more informed priors.

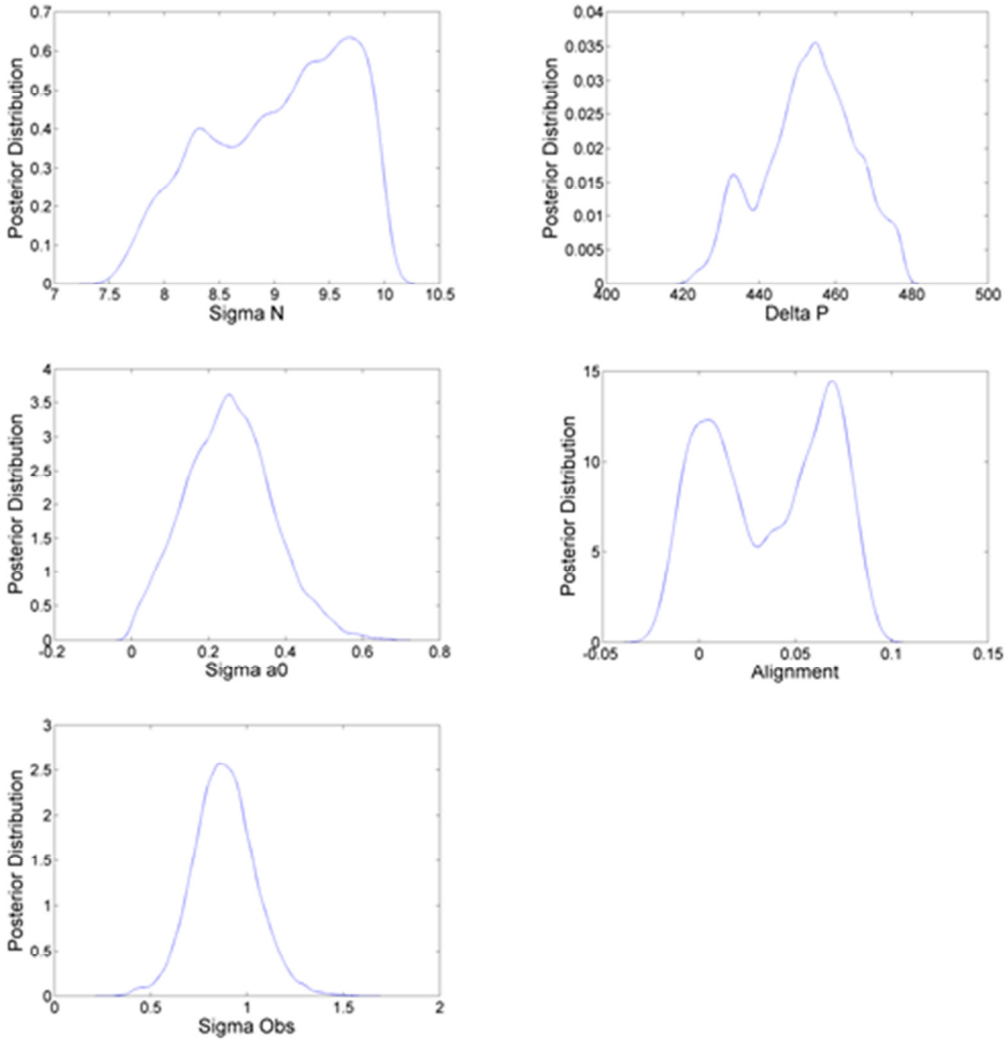


Figure 4.11: Posterior distributions for other calibrated parameters

To further illustrate this point, a more complete calibration analysis was performed. This new analysis utilized more informed priors and a discrepancy term. A normal distribution was used as the prior distribution for the parameters $\boldsymbol{C}$ and $\boldsymbol{m}$ which are the primary focus of this research. The prior distributions shown in Figure 4.9 were used this time. The discrepancy term, as discussed at great length in [35], is necessary to insure that the uncertainty in the posterior distributions of the parameters is not combined with the model form error incurred through the use of an imperfect model. The results of

this refined model with more informed priors and the added discrepancy term are shown in Figures 4.12 and 4.13.

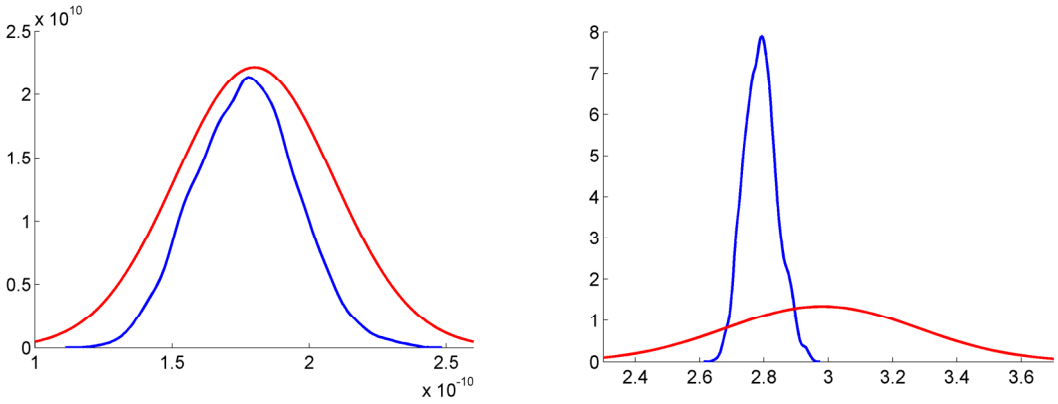


Model Parameter C

Model Parameter m

Figure 4.12: Posterior distributions of $\boldsymbol{C}$ and $\boldsymbol{m}$ parameters calibrated using the refined Bayesian model parameter calibration technique.

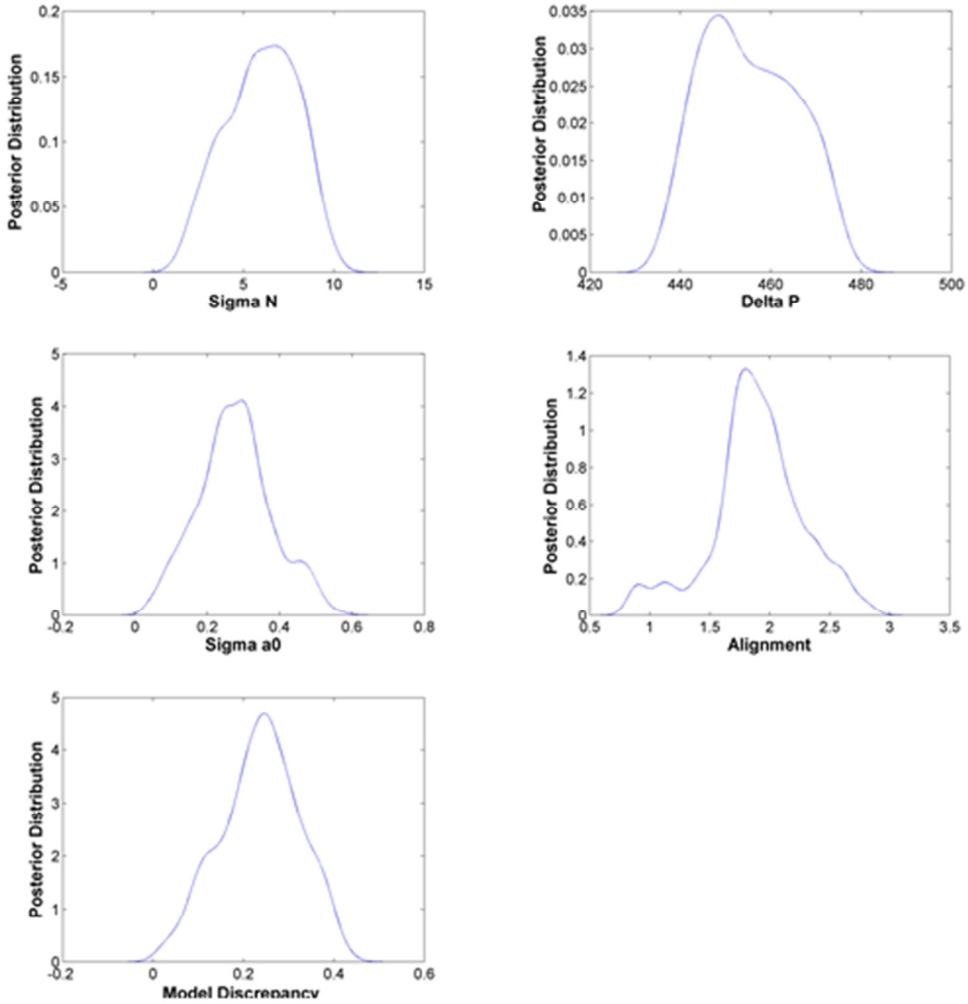


Figure 4.13: Posterior distributions for other calibrated parameters

## 4.6 Conclusion

A framework was developed in this chapter to apply knowledge of uncertainty sources present in fatigue crack growth experimentation toward the quantification of the uncertainty in the parameters of a crack growth model. Two material parameters, *C* and *m*, are used in the Paris law crack growth model to predict a crack growth rate given a stress intensity factor range. Typically the values, and the uncertainty about said values, for these material constants are found using a linear regression analysis. The results presented in this chapter show that this reported uncertainty in the material properties is

not justifiable considering that some of the uncertainty is actually coming from other sources than the material itself. The methodology presented here used a Bayesian calibration technique to compare observation data against model prediction that is affected by several model parameters and error terms. This technique attributes uncertainty to all of the calibrated model parameters rather than just $C$ and $m$. A comparison of the material property distributions found via linear regression and Bayesian calibration shows that not only is the uncertainty reduced but the distribution type and calibrated mean parameter values are different. It was shown that error terms can be calibrated as well. The information gained from the calibration of the error terms can be used to further improve the analysis by determining which parameters are contributing the most uncertainty to the experimentation results. It can also be used to determine which variables have negligible effect on the likelihood function and therefore the experimentation as a whole. This information can be used to refine the experimentation and to determine the most efficient means to distribute a budget aimed at minimizing the experimental uncertainty.

# CHAPTER 5

# MODEL VALIDATION

## 5.1 Introduction

In Chapter II, a computationally efficient two-stage approach for planar approximation of non-planar crack growth was developed. The proposed methodology used a parameterized representation of the non-planar crack, and employed two surrogate models: the first surrogate model is trained using FRANC3D based simulations of non-planar fatigue crack growth to capture the relationship between the applied load history and equivalent planar crack orientation. The second surrogate model is trained using planar crack growth simulation to calculate the stress intensity factor as a function of crack size, crack orientation, and load magnitude for use in planar crack growth analysis.

Individual predictions of the two surrogate models, as well as their combined predictions were verified for accuracy using FRANC3D based finite element simulations of non-planar fatigue crack growth in the rotorcraft mast example that was discussed in Chapter III. The verified two-stage approach was then used to conduct probabilistic analyses designed to quantify the effects of various sources of uncertainty in crack growth, including natural variability in loading, initial crack size, and model uncertainty during the crack growth analysis. In Chapter III a methodology was presented to account for numerical errors caused by spatial and temporal discretizations. The work presented in that chapter will be expanded in this chapter to be utilized for the equivalent planar model. The same discretization variables that were used to control the resolution of the

temporal and spatial meshes in Chapter III will be used once again. Chapter IV presented the calibration of fatigue crack growth model parameters using experimental data when experimental error is considered. The work in that chapter was performed using aluminum samples and since the material for the rotorcraft mast problem is 4340 steel, this is the material used in the discussion presented here.

In this chapter, the focus of the work presented will be on validation of the equivalent planar crack growth (EPCG) model using Bayesian hypothesis testing. In this study, multiple sets of experimental data were available to be used in the model validation process. This chapter strives to demonstrate how multiple sources of information can be linked via a Bayes network to provide complete model validation. The EPCG model employed in this work will be trained using data that has been corrected for discretization error and the model parameters will be calibrated using the Bayesian parameter calibration technique that was presented in Chapter IV.

## 5.2 Discretization Error in EPCG Model

A detailed discussion on discretization errors present in fatigue crack growth modeling is presented in Chapter III but a brief summary will be provided here for clarity. Since most modern fatigue crack growth analyses rely on finite element models there is almost always some inherent spatial discretization error present in the results. This numerical error is proportional to the refinement of the spatial mesh used in the finite element solver. In Chapter III, a Gaussian process model was used to estimate the spatial discretization error for entire crack fronts. The model was trained by gathering crack growth results for varying levels of finite element mesh refinement. The idea being

that an infinitely refined mesh will eliminate the spatial discretization error. Since an infinite mesh is impossible, extrapolation was performed to predict the result at this infinite refinement.

The Gaussian process model is not the only means for quantification of discretization error however. A much simpler technique was presented by Richards [50] using the Richardson extrapolation technique that is used to determine the converged solution of a sequence of refinements. Using Richardson extrapolation, the discretization can be calculated as:

$$\epsilon_h = \left(\frac{f_1 - f_2}{r^p - 1}\right) \tag{37}$$

where $f_1$ and $f_2$ are the solutions for the coarsest mesh and next finest mesh respectively, $r$ is the mesh refinement ratio, and $p$ is the order of convergence. If the parameters $h_1$ and $h_2$ are used to denote the corresponding mesh sizes of $f_1$ and $f_2$, then the mesh refinement ratio is simply $h_2/h_1$. The order of convergence can then be calculated as:

$$p = \frac{log\left(\frac{f_3 - f_2}{f_2 - f_1}\right)}{\log(r)} \tag{38}$$

where $f_3$ is the result of the finest mesh test and the other variables are the sames as was defined above.

It should be noted that although the Richardson extrapolation technique for discretization error quantification is convenient, it is not without some serious drawbacks. The main drawback to the technique is the list of criteria required for its use. The first

such criterion is the requirement of a uniform mesh refinement. While this requirement may seem rather insignificant, the difficulty usually is increased because of the second requirement which is that the mesh tests need to be performed in the convergent region of the sequence. Since it is difficult to determine where exactly the "convergent region" lies, the limit on the mesh tests is usually enforced by computational limits. In the spatial discretization problem for example, the convergence point is infinity. Since mesh tests cannot be performed at infinity, they are usually performed at a level that is near the computational limits of the finite element solver. The third criterion for Richardson extrapolation is that the mesh test results be monotonically increasing or decreasing. It was this requirement that led to the use of the Gaussian process model in the work presented in Chapter III. Since the crack fronts in that chapter were represented in a latent space, the mesh tests did not necessarily lead to monotonic behavior in the results. The Gaussian process modeling technique is capable of handling these inconsistencies in the data but the Richardson extrapolation is not.

The EPCG model presented in this chapter does not require the latent space representation of the crack fronts and is therefore a simpler case for the discretization error quantification. Since the results of the mesh tests for the EPCG model abide by the Richardson criteria, the Richardson extrapolation technique will be employed for discretization error quantification in this chapter.

### 5.3 Experimental Data from Bell Helicopter Textron Inc.

Bell Helicopter Textron Inc. provided three sources of experimental data for the use of model calibration and validation in this study. Middle tension (MT) tests were

supplied for the purpose of model calibration. Three sets of MT test data were supplied with were from 4340 steel specimens and a load ratio of 0.05. Another set of material level experimental data, KB-bar tests, was also supplied and was originally to be used for model calibration as well. The main difference between the KB-bar tests and the MT tests was that the Kb-bar tests possessed a surface crack rather than a through crack like the MT specimens. The results of these tests were originally intended to calibrate the $s$ parameter necessary for the $K_{EQ}$ calculation which will be discussed in Section 5.4, but the $K_{II}$ stress intensity factors were near zero which led to an insignificant $s$ calculation. Since the rotorcraft masts were subjected to multi-axial loading, they provided good calibration results for the $s$ parameter

The rotorcraft mast specimens were tested under a constant amplitude load with the same load ratio of 0.05. Four specimens were tested but only two yielded usable results. Of the two data sets, one was used for model calibration and the second was used for model validation. Since such a small data set was available, the calibration/validation was performed twice. Each time the procedure was performed a different mast specimen data set was held out for the validation purposes and the other one was used for calibration. The results presented in Sections 5.4 and 5.5 will be the average of these two iterations.

### 5.4 Experimental testing and model parameter calibration

The equivalent stress intensity factors used to train the original surrogate models for the EPCG model were based on FRANC3D's estimates, which compute the equivalent stress intensity factor as only a function of the maximum $K_I$ values, which is

not appropriate for use in applications that involve a multi-axial loading scenario. As seen in Figure 5.1, the surrogate model trained using FRANC3D's estimate of the equivalent stress intensity factors is conservative in its estimate of crack growth when compared to the experimental data.

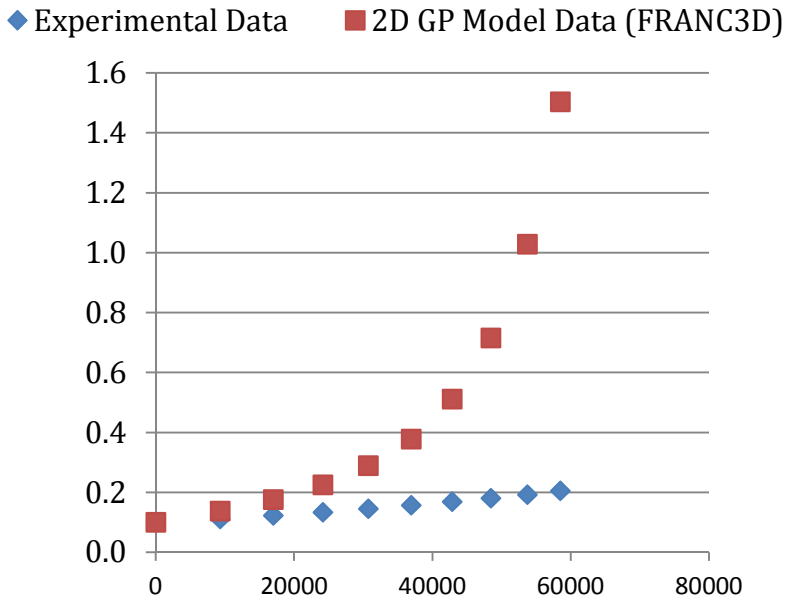


Figure 5.1. Crack Length Validation Comparison

In order to incorporate the characteristics of all three failure modes, a new methodology to compute the equivalent stress intensity factors has been adopted. Towards this, the three SIF values ($K_I$, $K_{II}$, and $K_{III}$) at each training location are obtained along each crack front using FRANC3D. The equivalent stress intensity factor is calculated as:

$$\Delta K_{EQ} = \frac{1}{B}\sqrt{(\Delta k_I)^2 + \left(\frac{\Delta k_{II}}{s}\right)^2 + \left(\frac{\Delta k_{III}}{s}\right)^2 + A\left(\frac{\Delta k^h}{s}\right)^2} \quad (39)$$

where: *A,B*, and *s* are material properties

$\Delta k_I$, $\Delta k_{II}$ and $\Delta k_{III}$ are the SIFs transformed to the characteristic stress plane

$\Delta k^h$ is the hydrostatic stress term

The derivation of this formula can be found in Liu and Mahadevan [51]. The method proposed by [51] requires estimation of a parameter *s*, which is the ratio of a particular material's (4340 steel in this case) Mode I and Mode II threshold stress intensity factors, which are material properties and can be obtained experimentally.

Since a wide range of values (1.09 – 2.50) for the $s$ parameter are available in the literature [52, 53], the parameter must be calibrated in order to determine a usable value. To perform the calibration, the following equation is used [51]:

$$\frac{1}{B}\sqrt{(\Delta k_1)^2 + \left(\frac{\Delta k_2}{s}\right)^2 + A(\Delta k^h)^2} = K_{I,th} \tag{40}$$

The above equation is appropriate for use in a low crack growth rate situation. Certain simplifications, such as $B = s$ and $A = 9(s^2 - 1)$, are made based on the assumption of the presence of tensile dominated loading. The $K_{I,th}$ values for each material level experiment were acquired during the experiment by Bell Helicopter. Using these $K_{I,th}$ values and the SIF values computed by FRANC3D from an FEA model of the rotorcraft mast, the "s" parameter can be determined. The Bayesian model parameter calibration was once again employed for this calibration.

The procedure outlined for model parameter calibration in Chapter IV is employed once again here. The goal once again is to obtain the parameters $C$and $m$ in the Paris law crack growth equation plus the new parameter $s$ is also calibrated. The values of parameters $C$ and $m$ calculated here are different than those calibrated in chapter IV since their calibration is based on experimental testing of 4340 steel specimens instead of aluminum.

Another major difference in the calibration in this chapter versus the calibration presented in Chapter 4 is that multiple data sets from different sources are present. Experimental data from Bell Helicopter is available for material level (middle-tension-MT) tests and for component level (rotorcraft mast) tests. The MT data from Bell is used first for $C$ and $m$ parameter calibration. The priors used for this initial calibration were based on literature values of $C$ and $m$ with distributions $N(1e^{-9}, 1e^{-10})$ and $N(2.7, 0.27)$ respectively. The posteriors from this calibration are then fed to the next stage of calibration which utilizes data from CT specimens in which experimental errors are also addressed.

The next stage of the calibration comes from compact tension experimental data as was presented in Chapter IV for aluminum. The experimental setup was the same for the 4340 steel specimens as was described in Chapter IV for the aluminum test specimens. The posterior distributions for the $C$ and $m$ parameters are then past to the calibration using the mast data from Bell Helicopter Textron Inc.

Since the component level test involves bending and torsional loading, all three modes of fracture must be considered instead of only the first mode which is the case for most material level tests. Since all three fracture modes are present, the component level

tests are the best source for calibration of the $s$ parameter that is required for the $K_{EQ}$ calculation that was discussed previously. The EPCG model is a function of the $s$ parameter as well as the Paris coefficients $C$ and $m$ and is therefore used for the calibration. The prior distributions for the $C$ and $m$ parameters are the posterior distributions from the previous calibration and the prior for the $s$ parameter is based on literature values [52] and is $N(1.09.0.1)$. Similar to the previous step, the prior distributions for the $C$ and $m$ parameters are the posterior distributions resulting from the previously performed CT calibration.

Figure 5.2 displays the Bayes network for incorporation of the multiple sources of data available for model validation in this project. The actual implementation of this network was described above and is shown in Figure 5.3. The order in which these calibrations are performed can be justified by investigating the likelihood calculation for the network presented in Figure 5.2:

$$\mathcal{L}(C, m, s) = P(D_{MT}|C, m)\, P(D_{Mast}|C, m, s)\, P(D_{CT}|C, m) \tag{41}$$

The associative property allows that mathematically, it doesn't matter in which order the calibrations are performed. The implementation order chosen for this study was done so that the mast calibration was performed last due to its similarity to the validation data. The CT calibration was chosen to be performed after the MT tests due to its consideration of experimental errors. The posterior distributions for the calibrated parameters are presented in Figure 5.4. Samples are then taken from these distributions to evaluate the EPCG model used in the model validation presented in the next section of this chapter.

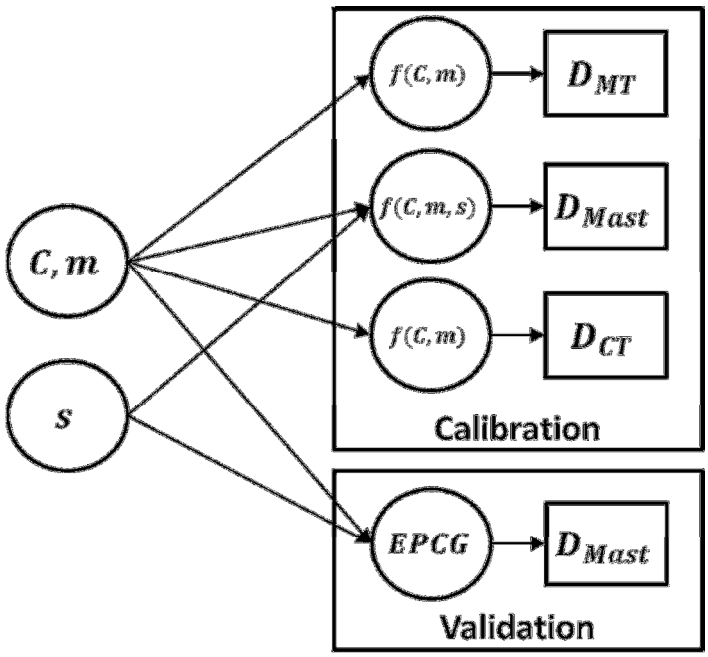


Figure 5.2: Bayes network for calibration and validation when multiple information sources are available

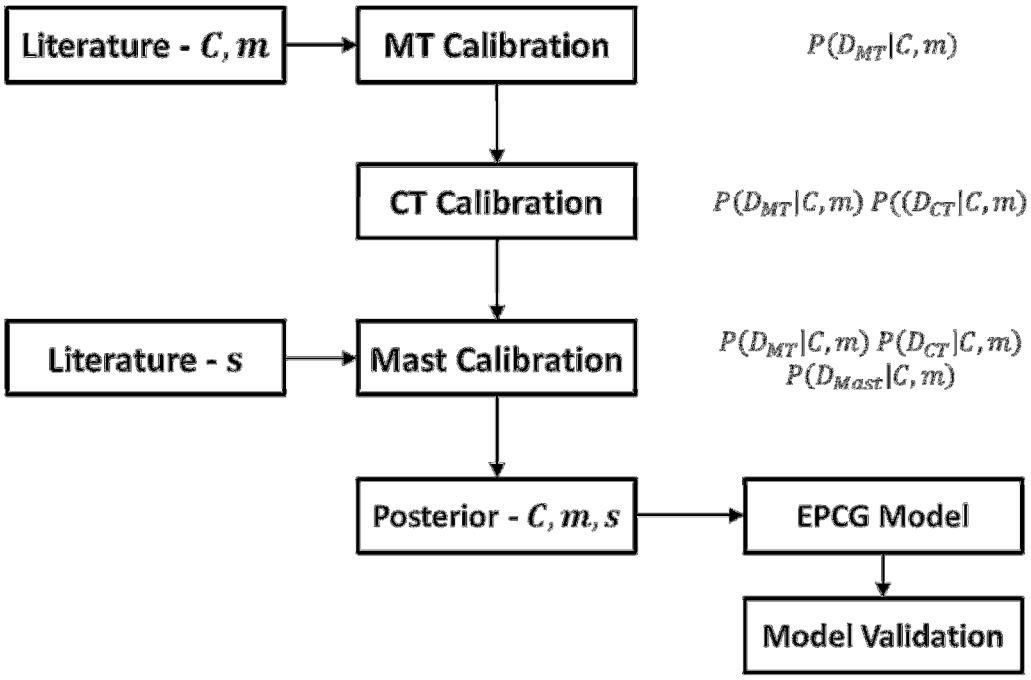


Figure 5.3: Implementation of calibration procedure

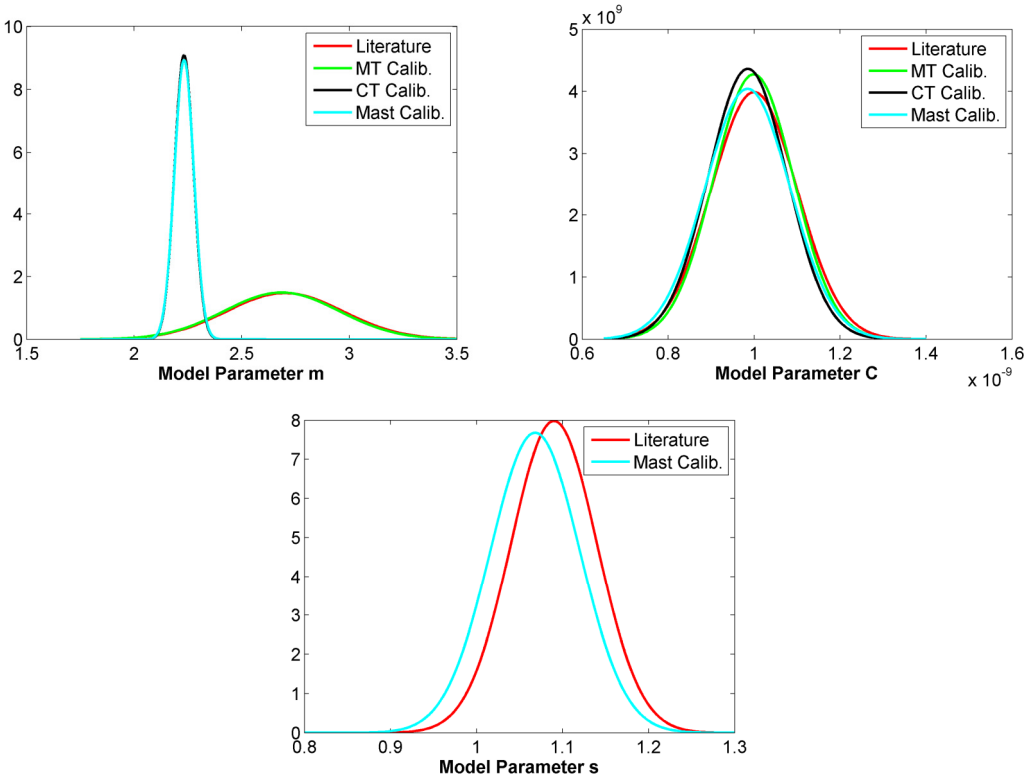


Figure 5.4: Posterior Distributions of Calibrated Parameters

## 5.5 Bayesian Model Validation

Bayesian hypothesis testing was the quantitative validation technique chosen to compare the model prediction with experimental results. Bayesian hypothesis testing is used to compare multiple models so as to judge which model's prediction most closely resembles the experimental results. The data provided by Bell for the rotorcraft mast was deterministic but in order to provide a more realistic representation of real world data, an observation error of 0.025 inches was assumed.

In the case of model validation, the posterior probabilities of the two hypotheses compared using the Bayesian method are $P(H_0(\text{The model is correct})|D)$ and

$P(H_1(\text{The model is incorrect})|D)$. The probabilities of observing the data are then $P(D|H_0)$ and $P(D|H_0)$ which can also be referred to as likelihoods $L(H_0)$ and $L(H_1)$. The Bayes factor is simply the ratio of these two likelihoods.

Rebba [54] showed that this Bayes factor that comes from the hypothesis testing can be used to provide a measure of model confidence. The confidence measure is calculated as:

$$Model\ Confidence = \frac{P(\boldsymbol{D}|H_0)}{P(\boldsymbol{D}|H_0) + P(\boldsymbol{D}|H_1)} = \frac{Bayes\ Factor}{1 + Bayes\ Factor} \tag{42}$$

Another model validation technique will be presented in Chapter VI of this thesis that employs a reliability-based metric but that will be discussed later.

A visual comparison of the physical experiment/predictive model results for one of the mast specimens is presented in Figures 5.5. The figure provides two samples of model prediction results. The first model prediction set is based on the EPCG model before any correction was provided for discretization error and before the Paris parameters were calibrated. The second set of prediction results is based on a revised EPCG model which has been adjusted to compensate for discretization errors and which uses model parameters that were quantified using the Bayesian model parameter calibration technique.

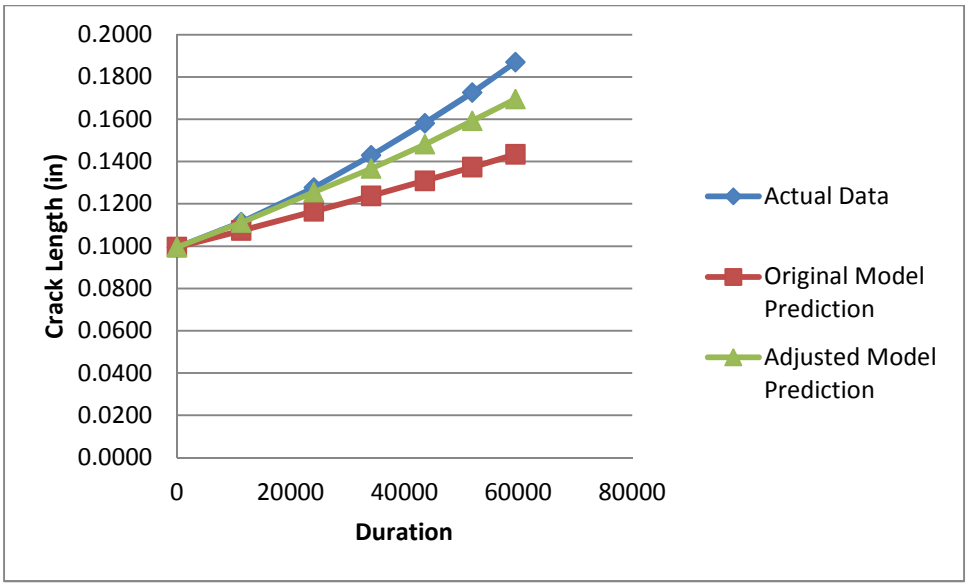


Figure 5.5: Experimental Data vs. Model Prediction

A more quantitative validation investigation using Bayesian Hypothesis testing is presented in Tables 5.1 and 5.2. The tables show the validation results for both models and show that the model is improved by the addition of discretization error and the calibration of the Paris law parameters. The values are an average of the validation results for the two specimens used, where in each case one mast was used for model calibration and the other was used for validation.

Table 5.1: Validation results for unadjusted prediction model

| Model Before Revision | | | | |
|---|---|---|---|---|
| **Cycles** | **BF-Depth** | **Confidence** | **BF-Length** | **Confidence** |
| 11315 | 4.04 | 80.15% | 6.90 | 87.34% |
| 16985 | 4.01 | 80.04% | 6.28 | 86.26% |
| 24067 | 3.94 | 79.74% | 5.57 | 84.78% |
| 24170 | 3.94 | 79.74% | 5.56 | 84.75% |
| 30719 | 3.88 | 79.49% | 4.83 | 82.85% |
| 34163 | 3.85 | 79.37% | 4.37 | 81.38% |
| 36952 | 3.82 | 79.26% | 3.99 | 79.97% |
| 42878 | 3.71 | 78.76% | 3.93 | 79.71% |
| 43576 | 3.70 | 78.71% | 3.79 | 79.12% |
| 48449 | 3.61 | 78.32% | 2.80 | 73.66% |
| 51889 | 3.46 | 77.58% | 2.65 | 72.57% |
| 53722 | 3.38 | 77.15% | 2.58 | 72.04% |
| 58487 | 3.29 | 76.68% | 2.43 | 70.83% |

Table 5.2: Validation results for prediction model after parameter calibration and discretization error

| Model After Revision | | | | |
|---|---|---|---|---|
| **Cycles** | **BF-Depth** | **Confidence** | **BF-Length** | **Confidence** |
| 11315 | 4.86 | 82.95% | 8.00 | 88.89% |
| 16985 | 4.85 | 82.89% | 7.36 | 88.04% |
| 24067 | 4.82 | 82.83% | 6.74 | 87.09% |
| 24170 | 4.82 | 82.83% | 6.74 | 87.08% |
| 30719 | 4.80 | 82.77% | 6.34 | 86.37% |
| 34163 | 4.79 | 82.74% | 6.11 | 85.94% |
| 36952 | 4.79 | 82.72% | 5.95 | 85.61% |
| 42878 | 4.77 | 82.67% | 5.53 | 84.68% |
| 43576 | 4.77 | 82.67% | 5.47 | 84.55% |
| 48449 | 4.76 | 82.63% | 5.07 | 83.52% |
| 51889 | 4.75 | 82.60% | 4.77 | 82.66% |
| 53722 | 4.74 | 82.58% | 4.58 | 82.09% |
| 58487 | 4.72 | 82.52% | 4.26 | 80.98% |

## 5.6 Conclusion

This chapter presented the validation of the equivalent planar crack growth model. The two surrogate models employed in equivalent planar analysis were trained using stress intensity factors acquired via FRANC3D and the crack propagation was performed by use of Paris law. In the original approximation, the equivalent stress intensity factor was determined solely based on $K_I$. A new $K_{EQ}$ calculation technique is then employed to account for all three modes of failure. Since the $K_{EQ}$ calculation required an additional material property, it along with the Paris law parameters, were calibrated using experimental data. The calibration methodology presented here provided a thorough means by which multiple sources of information can be utilized to provide a detailed and robust model parameter calibration and then a more relevant model validation.

The effect of the discretization error and the model parameter calibration on the predictive model was also investigated. The adjusted model provided more accurate results that are closer to the experimental rotorcraft specimen results provided by Bell Helicopter as can be witnessed in Figure 5.5 and Tables 5.1 and 5.2.

# CHAPTER 6

# STRUCTURAL HEALTH MONITORING AND FATIGUE DAMAGE PROGNOSIS FOR CONDITION BASED MAINTENANCE INSPECTION SCHEDULING

## 6.1 Introduction

The previous chapters of this thesis focused on the uncertainty quantification as it pertains to three dimensional crack growth modeling and experimentation. The focus of this chapter is to use uncertainty quantification results towards risk management. Until recently, most critical components in aircraft were operated on a rigid safe-life basis. That is, these components were immediately removed from service as soon as any type of fatigue damage was observed during routine in sections of the craft. The reason for operating under this condition is due to the complexity and uncertainty in service environments for these components. As more research is completed in understanding these uncertainties and as computational power increases, alleviating the modeling challenges of complex systems, the rigidity of the safe-life condition can begin to be relaxed. If the models for these components are found to be more reliable, the components can continue to remain operational as long as certain structural health monitoring (SHM) and fatigue damage prognosis (FDP) techniques are followed. It should be noted here that SHM and FDP are not inherently connected [55], but the integration of these two technologies has already been presented in the literature [56]; however, the goal of this chapter is to present a methodology for using these techniques

to determine an efficient and safe condition-based maintenance (CBM) schedule for an in-service rotorcraft mast.

Condition-based maintenance is a method of optimally utilizing maintenance time and equipment so as to reduce costs while maintaining an adequate level of reliability of a component. The motivation behind the development of CBM techniques [57] was to reduce downtime and the unnecessary replacement of components that still have significant remaining life but may have been in service longer than the safe-life tolerance.

Numerous tools and methodologies can be found in the literature for fatigue reliability analysis and inspection updating [58, 59, 60, 61]. Garbatov and Soares [62] proposed a method of optimized inspection planning for floating structures, in which inspection planning was treated as an optimization problem under reliability constraints. Zhang and Mahadevan [63] proposed a Bayesian approach for reliability updating and inspection decision-making with respect to corrosion fatigue incorporating the reliability of the NDI (non-destructive inspection) technique, inspection data, and model. McLemore [64] focused on using reliability-based inspection optimization (RBIO) to determine inspection fidelity based on the integration of uncertainty sources in a Bayesian network. In that work, the decision of inspection fidelity was made with respect to the component's entire life cycle. One major deficiency in this methodology is that in a DT approach the final life of the component is not known when the component is initially placed in service. This chapter extends McLemore's work to expand the inspection fidelity choice to a mission-by-mission scheduling decision making process rather than a total component life methodology which was presented there.

In the first few sections of this chapter, the focus will be directed toward the estimation of a proper inspection interval that will lead to an efficient yet safe maintenance schedule for aircraft structures. To that end, two alternative methods to determine an inspection interval on which to evaluate the fatigue damage present in a rotorcraft mast will be presented. In order to perform either of these interval estimation techniques, it is necessary to have a model capable of predicting crack growth from a given initial flaw and loading scenario. In this chapter, the equivalent planar crack growth model that was discussed in detail in Chapter II will be utilized. For clarity a brief summary of the methodology behind the equivalent planar crack growth model is presented in the following paragraph.

The computationally efficient two-stage approach for planar approximation of non-planar crack growth uses a parameterized representation of the non-planar crack, and employs two surrogate models. The first surrogate model is trained using FRANC3D [17] based simulations of non-planar fatigue crack growth to capture the relationship between the applied load history and equivalent planar crack orientation. This model is used to estimate the final crack orientation so that a planar crack growth model can be utilized to approximate the actual non-planar crack. The second surrogate model is trained using planar crack growth simulation to calculate the stress intensity factor as a function of crack size, crack orientation, and load magnitude for use in planar crack growth analysis. The orientation and stress intensity factors that are calculated from these two models can then be passed through any simple crack growth equation such as Paris Law [26] to estimate the non-planar crack propagation for a given load amplitude and duration.

Since both methods for inspection interval estimation presented in this chapter involve the use of some reliability measure in the predictive model that is to be used, it is necessary to have some rotorcraft masts that are reserved strictly for the purpose of model validation. A reliability-based model validation metric will be used in this chapter to determine the reliability of the crack growth model. The reliability metric is a simple measure of the probability that the crack growth model prediction lies with a specified error interval around the actual crack size at a prescribed time step. The first inspection interval estimation method is essentially just the time required for the model's reliability to fall below a certain value. The second method for determining a safe and efficient inspection interval is slightly more involved. A damage-tolerance approach is utilized for the second method. The damage tolerance approach employs the EPCG model to predict the point at which the predicted crack growth exceeds a predetermined critical value. Once this critical crack length barrier is passed the component should be inspected to see if a critical flaw has actually occurred.

After the inspection takes place, it is important to utilize the data that is obtained during the inspection. The data gathered from the inspection can be used to improve the model that is being used from the crack growth prediction. Bayesian model updating [21] is an appropriate technique to be used for this task and will be also be presented. A numerical example, as mentioned earlier, will also be provided for improved clarity of the techniques presented and to illustrate the overall framework for the procedure.

The latter portion of this chapter is focused on an expansion to the inspection interval estimation to include the concept of inspection fidelity. The determination of the inspection fidelity will be performed by implementing a detailed simulation model. The

model will be used to emulate the actual crack growth that is occurring or going to occur in the actual component. In this way, the model can be used to estimate the effect that different types of inspections can have on the remaining life of the component.

The estimate of remaining life will vary depending on the amount, and quality, of information gained during the inspection. In theory, a higher fidelity inspection will provide more information about the current state of the component and will therefore lead to the digital model predicting a longer component life after the inspection. The knowledge gained from the model's estimation will be used to add the inspection fidelity choice to the inspection schedule planning discussed earlier.

### 6.2 Types of non-destructive testing

In the area of SHM of fatigue fracture, there are many options available for non-destructive component inspection [65]. Two types of inspection are considered here: visual inspection and ultrasonic spectroscopy.

The visual inspection is the easiest and most useful type of NDT to perform. A visual inspection is simply a trained inspection technician simply visually analyzing the component to attempt to identify any fatigue damage. While there are definite advantages (low cost, ease of use) to this inspection technique, it is also somewhat imprecise. There is a large range of error associated with this inspection technique. The visual inspection technique can also only be used to measure surface cracks. If the crack depth is of concern then the usage of this technique is severely limited.

The second inspection method to focus on is the ultrasonic spectroscopy [66]. Ultrasonic tests (UT) utilize the acoustic properties of the component in question to assess the

presence of some type of flaw. The advantage of UT over visual inspection is that UT allows the user to see what is happening underneath the surface of the component. This is a useful tool for determining the depth of known cracks or for the discovery of hidden cracks that may not be visible on the surface of the component. Ultrasonic spectroscopy is also commonly used to assess corrosion damage. The drawbacks to UT are that while the inspection equipment itself is not expensive, the user must be a highly trained technician to properly interpret the results and calibrate the machine.

It is helpful to remember that the cost of a particular inspection is not only measured by the direct cost of the equipment used to perform the inspection. For instance, a visual inspection can typically be performed while the component is not only still installed in the system, but many times while the system is in use. Other more advanced systems may require the system to be temporarily removed from service so the component of interest can be removed and inspected. The system downtime is often a greater cost than the actual inspection.

### 6.3 Reliability-based model validation metric

The idea behind the reliability-based validation metric [54] is quite simple. Given a desired error tolerance, what is the probability that the difference between the model prediction and the experimental data is within that interval. One drawback to validation metrics is that they all possess some subjectivity, and this metric is no exception. The subjectivity for a reliability-based validation metric is in the error tolerance that must be chosen. In the case of fatigue crack propagation monitoring, it can be assumed that this

error interval is simply the detectability limit [67] of the inspection process. By using this value the subjectivity in the model validation is minimized.

The utility of the reliability-based validation metric is that a probability limit, $c$, can be added to the formulation ($P(-\epsilon < D < \epsilon) \geq c$) to ensure that the model prediction is rejected below a specified reliability level. The rejection of model prediction below a specified reliability (or model "confidence") is useful in crack growth monitoring because the inspection interval can be easily determined from this confidence cut-off. Another benefit of the metric is the ability to consider noise in the experimental data as well as the uncertainty in the model prediction. If normality is assumed, the model reliability can be calculated then as

$$r = \Phi\left[\frac{\varepsilon - (\mu - \mu_m)}{\sqrt{({\sigma_m}^2 + {\sigma_{YD}}^2)}}\right] - \Phi\left[\frac{-\varepsilon - (\mu - \mu_m)}{\sqrt{({\sigma_m}^2 + {\sigma_{YD}}^2)}}\right] \quad (43)$$

where $\epsilon$ is the acceptable error range (the detectability limit in this case), $\mu$ is the mean experimental observation, $\mu_m$ is the mean model prediction, $\sigma_m$ is the standard deviation of the model prediction and $\sigma_{YD}$ is the observation noise.

Once the validation of a series of test specimens is performed, a quantitative measurement of the model reliability is known. A series of predictions can be made with increasing duration length to establish a reliability curve for the model. It stands to reason that an increase in the duration of the prediction will lead to a decrease in the model reliability. If this is the case, the reliability will eventually reach a threshold value beyond which the model's prediction is no longer trustworthy and should not be used for maintenance decision making.

### 6.4 Estimation of detectability limit

In the previous section, the detectability limit during inspection was mentioned and was utilized as the error interval for the validation process. Since damage inspection is a critical aspect of aircraft component maintenance, it has led to the development of many different inspection techniques that are in use in the industry. Obviously, the most useful of these techniques are non-destructive inspection (NDI) techniques since they do not damage the component that is still in service within a fleet but also provide useful information about the component's airworthiness [68]. All NDI techniques have varying degrees of inspection fidelity characterized by probability of detection and detectability limit. The probability of detection (POD) is the probability of a crack that is present being detected by the inspection technique. The detectability limit is the minimum size of flaw that can be detected by the inspection technique. In this chapter, a statistical approach is taken to determine the POD for a given detectability limit. The probability of detecting a crack of size $a_n$ is then computed by:

$$f(a_n) = \Phi(\alpha + \beta a_n) = \frac{1}{2}\left[1 + \text{erf}\left(\frac{\alpha+\beta a_n}{\sqrt{2}}\right)\right] \quad (44)$$

$$\text{erf}(x) = \frac{2}{\sqrt{\pi}}\int_0^x e^{-t^2} dt \quad (45)$$

where the symbol Φ represented the standard normal cumulative density function, $erf$ is a Gaussian error function, $\alpha$ and $\beta$ are model parameters based on the chosen inspection fidelity, and $a_n$ represents crack size. Once the model parameters are determined, an acceptable POD can be selected. Based on that POD value, the estimation of the detectability limit follows naturally [69] by determining what size crack $a_n$ can be detected consistently given the selected POD.

### 6.5 Damage tolerance methodology

Since the airworthiness of rotorcraft components is a crucial safety issue, model reliability alone is not enough to determine a proper inspection interval. In order to maintain a safe inspection interval, a damage tolerance methodology should be used in conjunction with model reliability.

One key component to the damage tolerance methodology is the selection of the critical and allowable flaw sizes that determine whether or not a component remains in service. The critical flaw size is computed by considering the geometry and the material properties and preferably elastic-plastic fracture analysis so that brittle fracture, plastic collapse, and buckling can be considered. Once the critical flaw size is known the allowable flaw size can be estimated based on uncertainties present in the predictive model being used and input parameters such as applied loading and material constants. Considering all of the previously mentioned quantities, the allowable flaw size should be relatively small when compared with $a_{Critical}$, so that it will take a reasonable amount of time for the crack to grow from $a_{Allow}$ to $a_{Critical}$. Following this provision is important to ensure that the safety of the component is maximized.

Figures 6.1-6.3 demonstrate how a typical damage tolerant inspection interval estimation is performed. First, the model is used to grow the crack starting with an initial flaw size equal to the detectability limit of the inspection technique to be used. The crack is propagated to the point where it is equal to the allowable value. The component is then inspected at $N_{Ins} < N_{Allow}$. At this point, if no flaw is detected then the procedure is repeated(Figures 6.1 & 6.2). Once a flaw has been detected, the initial flaw size is adjusted to $a_{Obs}$ and the inspection procedure is repeated as in Figure 6.3. [70]

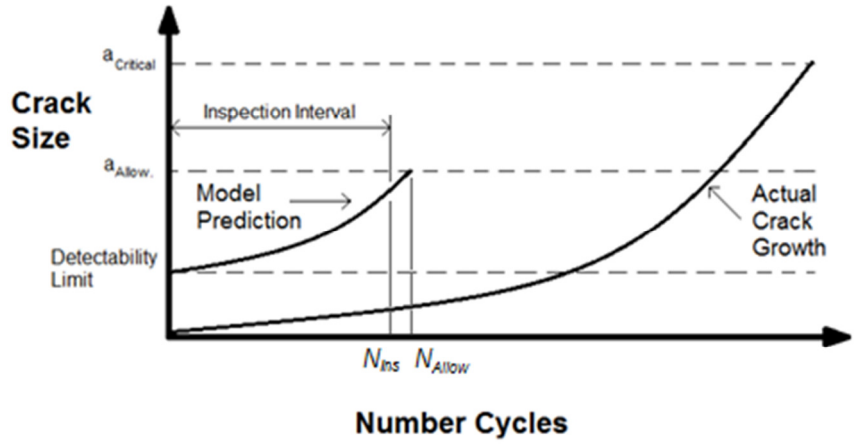


Figure 6.1: Determination of inspection interval prior to actual crack being observed

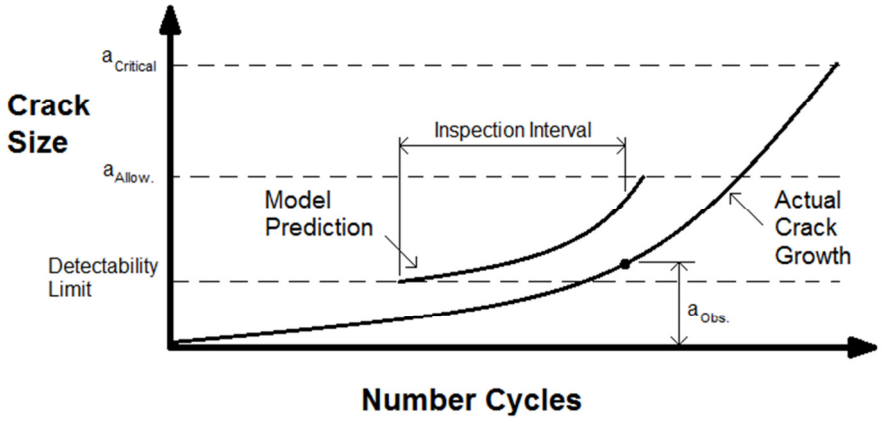


Figure 6.2: Determination of inspection interval after first inspection

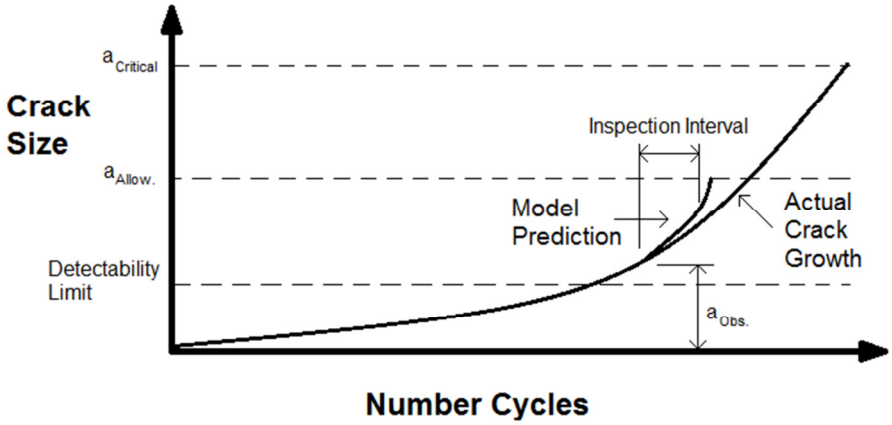


Figure 6.3: Determination of inspection interval after flaw has been observed

The above approach did not consider the reliability of the model. In order to provide a more reliable and efficient methodology, the model reliability estimate can be combined with the damage tolerance methodology for estimation of the inspection interval. First, the detectability limit must be estimated using Eq. 40. A POD that is reasonable for the component in question should be used for this estimation. Once the detectability limit is known, the reliability-based validation metric can be used to determine the confidence in the predictive model being used. In order to perform this validation, some components must be reserved from the fleet for strictly validation purposes. A model confidence can be determined for each of the reserved specimens and then averaged to give an overall confidence in the model for the fleet. Based on these results, the inspection interval based on the validation of the model can be determined give some confidence limit placed on the model. As an example, if the confidence limit is said to be 95% and the model's reliability drops below 95% at 32,000 load cycles, then that is the inspection interval at which the component should be evaluated. However this value should only be used if it is below the value estimated by the damage tolerance methodology.

For actual implementation of this methodology, it should be combined with the technique proposed in Section 6.3 using the reliability validation metric. A framework for this proposed methodology is presented in Figure 6.4. As can be seen in the diagram, the procedure begins by determining whether a flaw is detected or not. If a flaw is detected then the measured crack size is used as the initial crack for the prediction model, but if a flaw is not detected then the detectability limit of the inspection technique is used as the initial crack length in the prediction model. The model is then used to determine when the flaw should reach a critical size and that duration is then used as the inspection

interval for the actual component unless that duration is longer than the reliability limit for the model. If the crack size measured during the inspection is at or near the critical size, then the component should be retired; otherwise, the entire procedure will repeat.

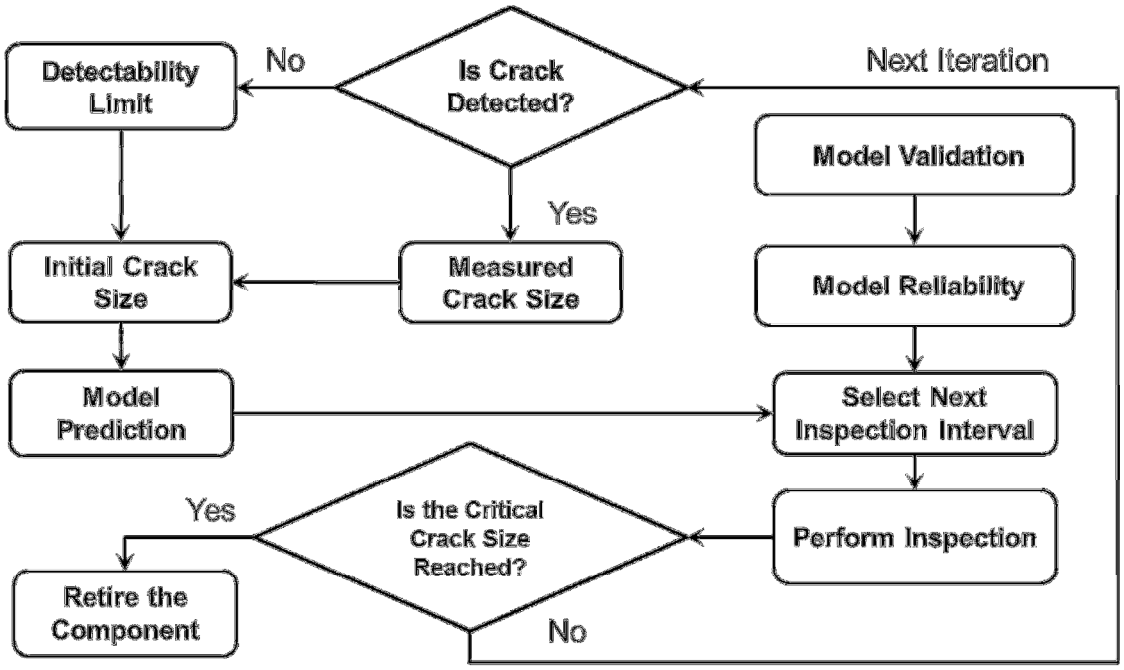


Figure 6.4: Framework for maintenance inspection scheduling

### 6.6 Numerical example: inspection interval estimation

For this example, experimental crack growth data for six rotorcraft masts subjected bending and torsional loading were provided by Bell Helicopter for the purposes of model validation. Since no in-service rotorcraft mast was available for maintenance scheduling, it will be assumed that five of the supplied data sets are withheld components used for model validation and the sixth component will serve as the in-service component for which the maintenance scheduling is being determined.

Using the reliability metric described in Section 6.3, a measure of the model reliability is obtained from the five test specimens. This is achieved by using the predictive model to estimate the crack growth at an increasing duration of load cycles. The model reliability is then tracked, as can be seen in Figure 6.5. The model reliability drops below 95% at a cycle duration of 30,704 cycles; therefore, 30,704 is the largest inspection interval for the remainder of this example.

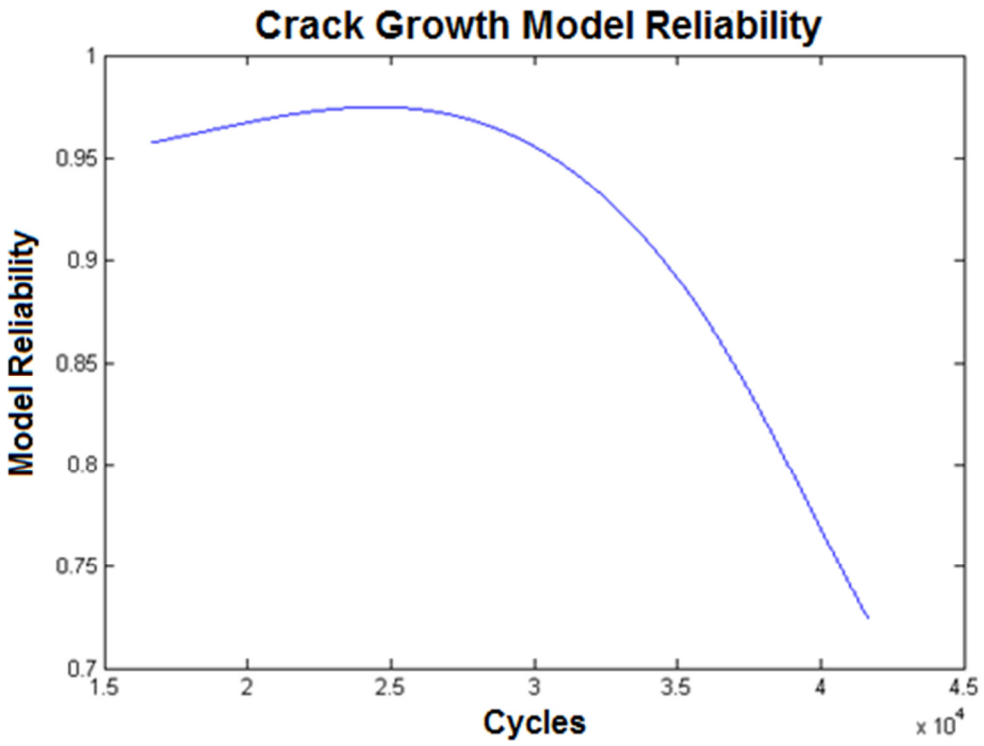


Figure 6.5: Model reliability curve.

For the damage-tolerance approach to inspection interval estimation, inspection fidelity parameters were chosen so that the POD was 95% for a 0.1 inch crack. The allowable crack length to be used in this method is 0.21 inch. The EPCG model is used to grow the crack to the 0.21 inch threshold and the duration to arrive at this length is

found to be 57161 cycles. Since the lower of the two values is 30704 cycles, an inspection is to be performed at that point. The inspection found that there was a crack at 30704 cycles and that the length was 0.1537 inch. The model results and the actual crack growth are displayed in Figure 6.6.

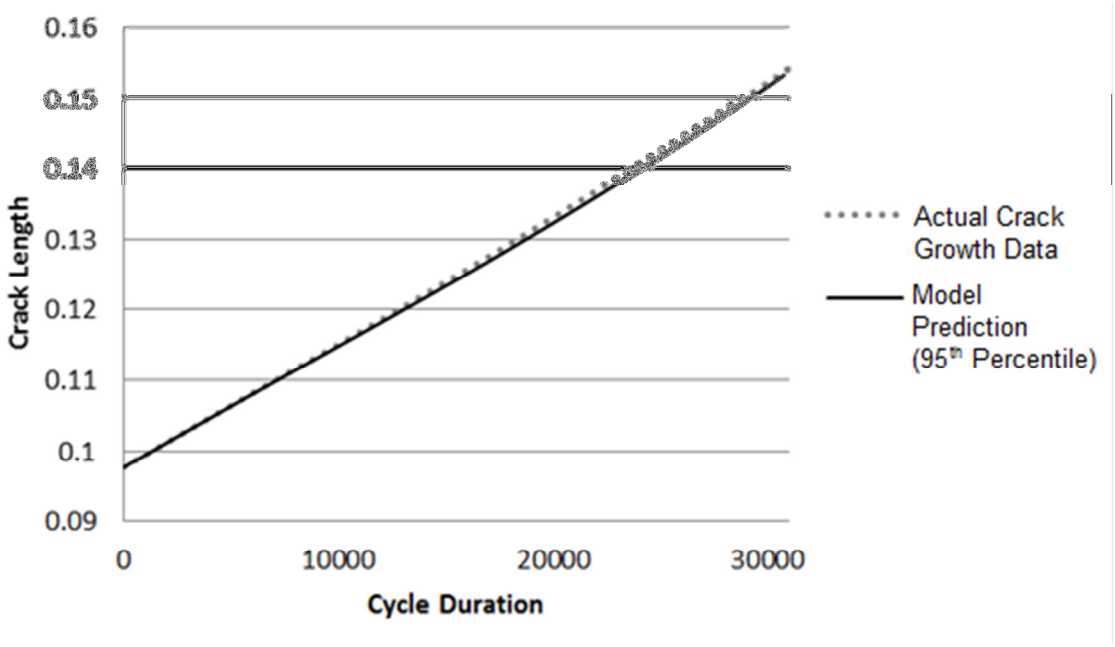


Figure 6.6: Actual crack growth and initial model prediction.

The initial crack is then set to be 0.1537 in. and the model is once again used to predict the duration required to reach the critical flaw length (22177 cycles). The second inspection (performed 22177 cycles after the first inspection) observed a crack with a length of 0.2032 inch. The model results and the actual crack growth between the first and second inspections are displayed in Figure 6.7.

Following the same procedure outlined before, the inspection interval after the second inspection is found to be 5761 cycles. The third inspection yields an observed actual crack length of 0.2173 inch. The model results and the actual crack growth

between the second and third inspections are displayed in Figure 6.8. Since the actual crack length has nearly reached the allowable crack length, the rotorcraft mast would most likely be retired from service at this point. For completeness, Figure 6.9 shows the entire operation comparing the model results at each iteration with the actual crack growth.

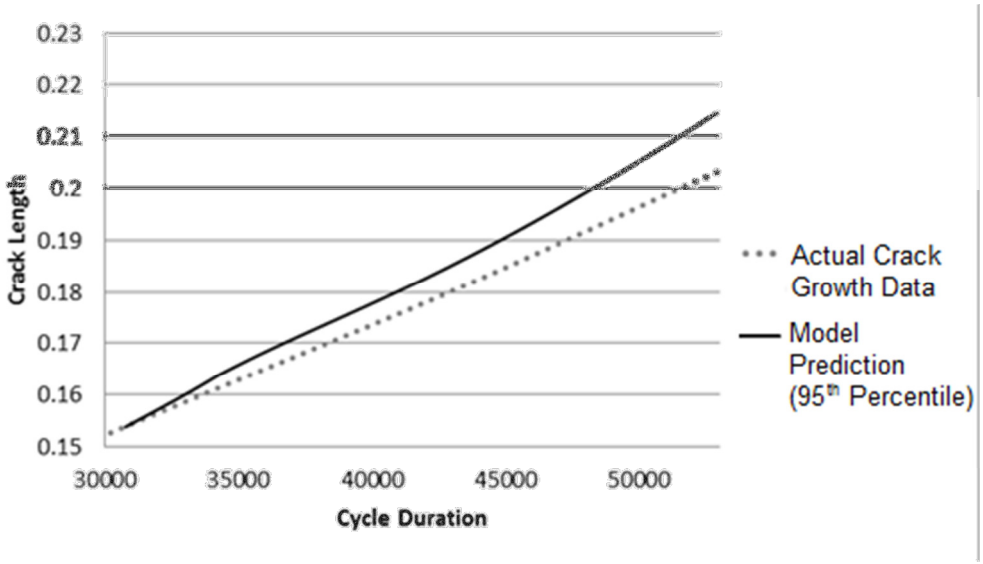


Figure 6.7: Actual crack growth compared against the model after the 1st inspection

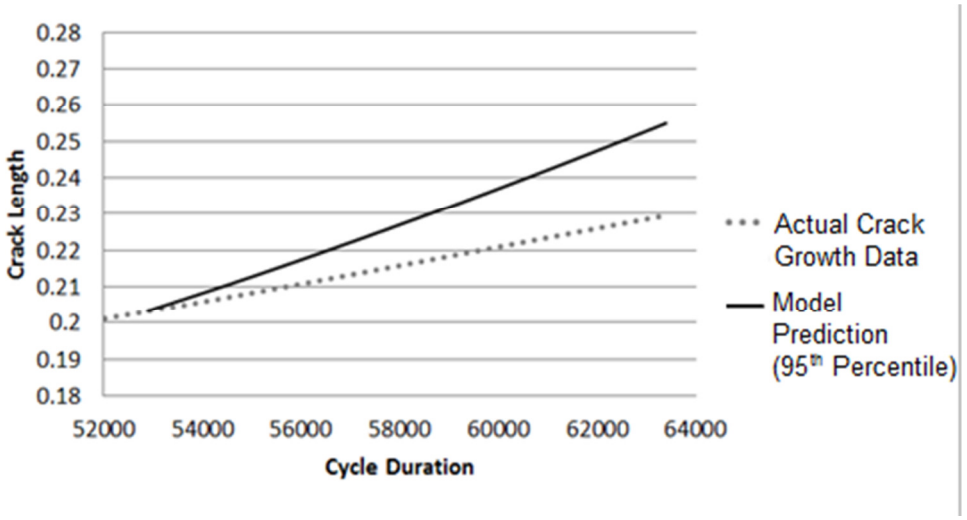


Figure 6.8: Actual crack growth compared against the model after the 2nd inspection

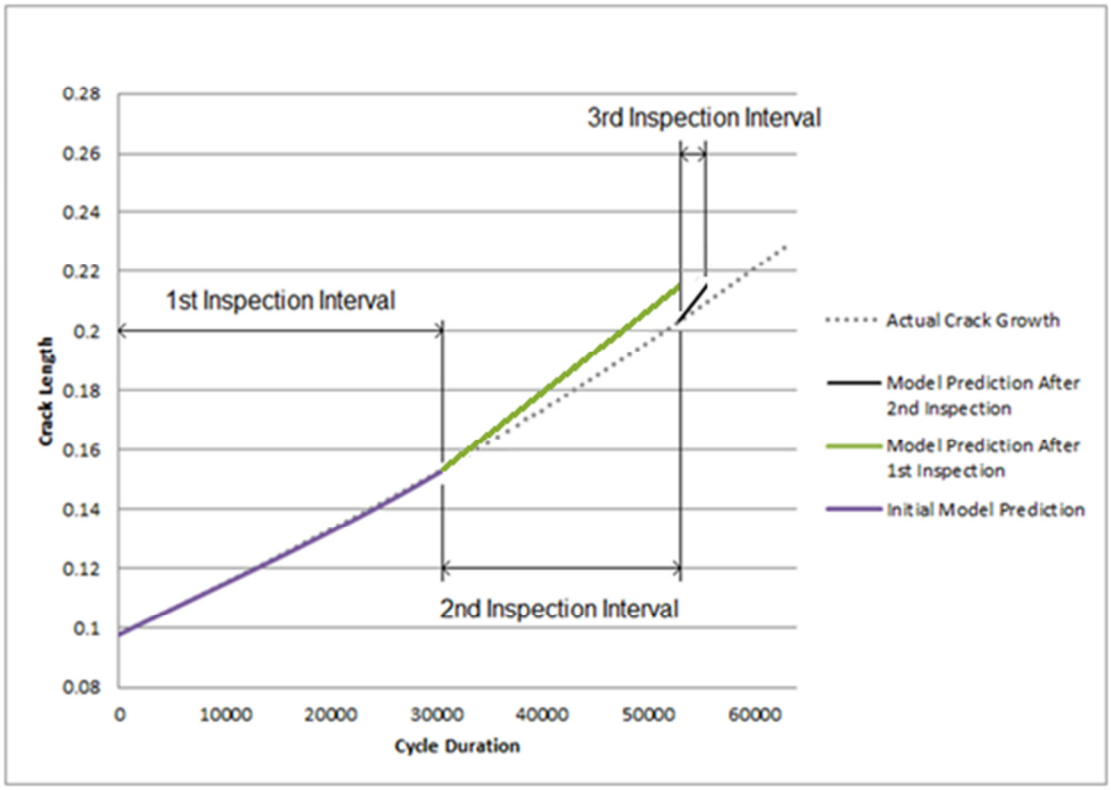


Figure 6.9: Maintenance inspection schedule for numerical example.

## 6.7 Extension to include inspection fidelity

The method for determining the fidelity of the inspection that will occur at each maintenance interval will be based on the next mission length required of the aircraft. The fidelity of the inspection technique will determine the next inspection interval. This value will then be compared with the length of time needed to perform the mission that is needed for the component to complete in that interval. Depending on this mission length a decision will be made as to which inspection should be performed. The equivalent planar crack growth model that was summarized in Section 6.1 and was discussed in detail in Chapter 2 will be used for model prediction.

To further increase the accuracy of the digital model's simulation results, a Bayesian network will be employed so that information gained from the maintenance inspections can be used to update the model parameters. A schematic of the Bayesian network used in this scenario is presented in Figure 6.10. The concept of Bayesian model parameter calibration was presented in great detail in Chapter IV and will be used here to once again calibrate the Paris law parameters $C$ and $m$. As discussed previously, the Bayesian framework lends itself quite well to this type of problem where there are several sources of uncertainty because it is capable of attributing the uncertainty to the appropriate causes. Since there is inherent uncertainty in the observation of the data and error in the model that is being used, it would be inappropriate to lump all of that uncertainty in the parameters of the model. By performing the calibration using the Bayesian network, the distributions of the model parameters can be properly updated as the information is gathered so as to increase the precision and accuracy of the model's prediction.

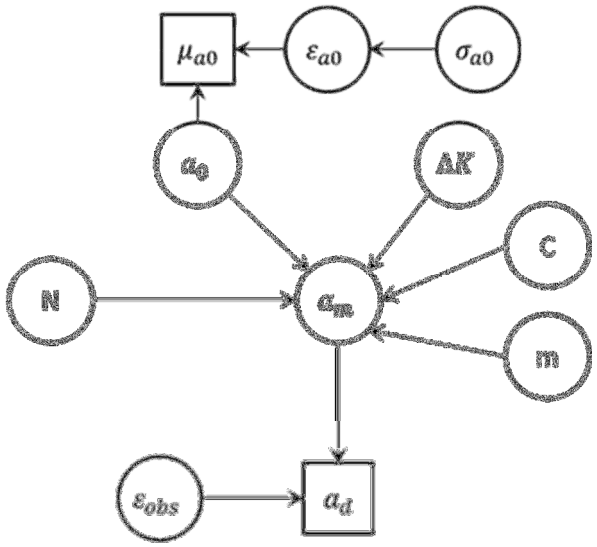


Figure 6.10: Bayes network for simulation model.

### 6.8 Framework for implementation with inspection fidelity considerations

The framework for implementation of inspection fidelity to the scheduling process begins with the determination of the first inspection interval using the method outlined in Section 6.5. At this inspection time instance, a choice must be made as to which type of inspection should be performed, a low fidelity inspection (LFI) or a high fidelity inspection (HFI). The decision variable will be the number of cycles required before the second inspection is needed and the prediction model is used to estimate the value of this variable. The information gained at the first inspection will be used to update the initial flaw used in the prediction model. A HFI will provide more information making the model's prediction more accurate and the result will be a longer inspection interval before the second inspection is needed.

The decision can then be made as to what type of inspection fidelity should be used at the next scheduled inspection depending on the mission that is needed to be performed. Consider a case where the upcoming mission for a system will require the component of interest to undergo 7000 cycles of loading and two types of inspection are considered: a LFI (e.g. visual inspection) and a HFI (e.g. ultrasonic spectroscopy). The model predicts that after the LFI another inspection will be needed in 5000 cycles but after the HFI, the next inspection shouldn't be needed for another 10,000 cycles. In this example, the HFI inspection should be performed so as to meet the needs of the upcoming mission. The user should keep in mind however that this prediction is only an estimation from the crack growth model. Once the inspection is physically performed the actual next inspection interval should be determined using the approached discussed in

Section 6.5 so as to insure the safety of the system. A diagram illustrating each of the steps in the methodology is presented in Figure 6.11.

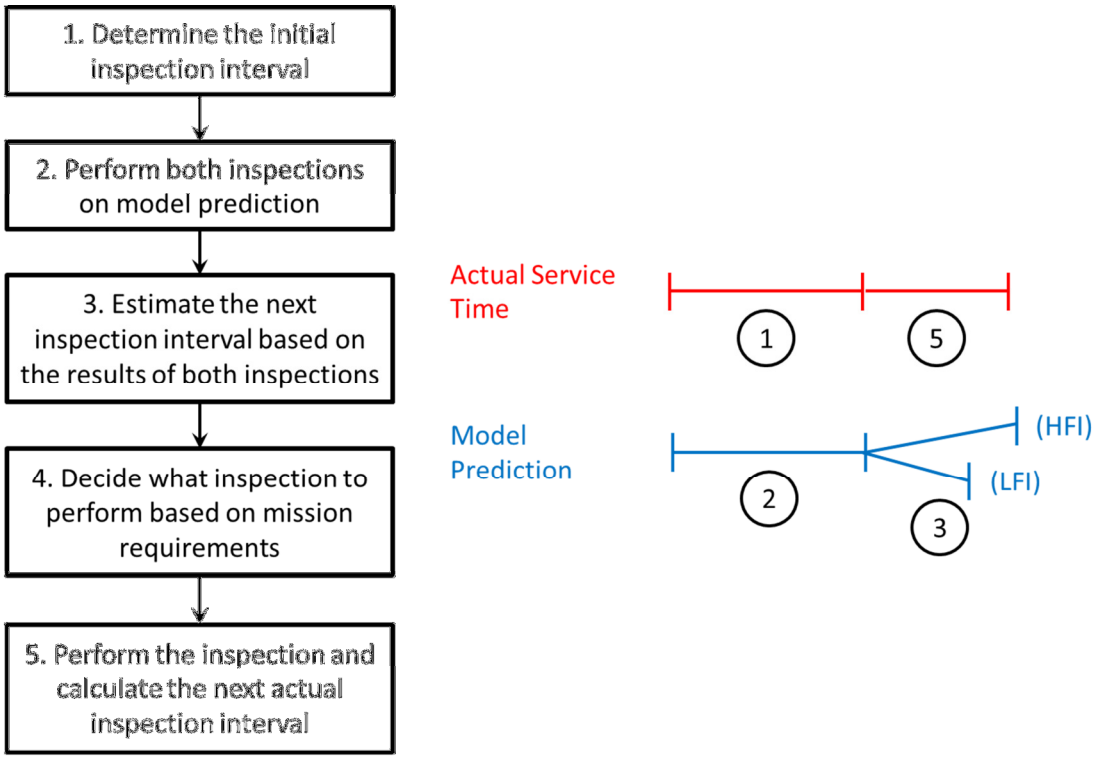


Figure 6.11 Framework for inclusion of inspection fidelity

### 6.9 Extension of numerical example to include inspection fidelity

The numerical example presented in Section 6.6 is continued here to include considerations for inspection fidelity. The results found in that analysis will be used here. The reliability limit found in that section of 30, 704 cycles will be implemented in this example also. Since this was the first inspection interval in that analysis, it will be used once again. The crack growth model can now be used to determine the type of inspection that should be performed at this inspection event. There are two different inspection

fidelities that can be chosen. The high-fidelity inspection (HFI) has an observation error of 0.005 inches and the low-fidelity inspection (LFI) has an observation error of 0.04 inches. This information is used to update the initial flaw size used in the prediction model for the duration of the second inspection interval. The results of inspection scheduling analysis are presented in Table 6.1.

Table 6.1: Results of digital model simulation

| | Observation Error | Next Inspection Needed |
|---|---|---|
| HFI | 0.005 inches | 18,537 Cycles |
| LFI | 0.04 inches | 11,105 Cycles |

The decision of which inspection to implement is dependent on the type of mission that must be performed. It is assumed that the duration of the upcoming mission is going to be 15,000 cycles. Since this duration is longer than the 11,105 cycles predicted from the LFI simulation and shorter than the 18,537 cycles yielded from the HFI simulation, the HFI should be performed at the next inspection.

Assuming the final specimen from the Bell Helicopter data as the component in service, the actual inspection data is taken as an interpolated result from the series of data points provided by Bell. Per this procedure, the actual inspected flaw growth at the initial inspection (30,704 cycles) is taken as a uniform distribution between 0.1400 and 0.1500. The results of the inspection can then be used to update the Paris Law coefficients used in the prediction model. The results of the Bayesian updating are presented in Table 6.2.

Table 6.2: Updated Paris Law parameters

| Parameter | *C* Mean | *C* Std. Dev. | *m* Mean | *m* Std. Dev. |
|---|---|---|---|---|
| **Prior** | 3.41E-10 | 3.41E-11 | 2.9976 | 0.29976 |
| **Posterior** | 3.41E-10 | 3.40E-11 | 3.0018 | 0.3274 |

Using these updated parameters, the predictive model can be used to determine the actual inspection interval for the next mission. The results of this analysis show that the digital model was quite accurate in its prediction of an inspection interval of 18,537 cycles. The inspection interval for the next mission is actually 20,065 cycles which means the digital model was slightly conservative. The procedure can then be repeated until the predicted duration is less than the desired mission length. Once this occurs the component should be retired.

### 6.10 Conclusion

The methodology presented in this chapter demonstrates an efficient and safe method for the determination of maintenance inspection interval and fidelity level for mechanical components in an aircraft. The procedure begins by evaluating the reliability of the predictive model that is used for the remainder of the analysis. The model reliability limit is used as a ceiling for the inspection interval. The ceiling insures safety of the component because it doesn't allow the model prediction to affect the inspection procedure outside of its reliable range. The damage tolerance approach to inspection interval determination limits the service range between inspections so that the component is not in service past the point where the model predicts that a flaw will have grown past some tolerable limit.

Once the initial inspection interval is determined, the prediction model was used to evaluate what type of inspection should be performed in order to maximize the use of the component. Depending on the fidelity of the inspection that is chosen, the duration until the next inspection is estimated by the digital model. That information can then be used to decide which mission can be performed and which inspection type should be chosen.

Condition-based maintenance is a means to efficiently conserve component life and maximize their use. The procedure outlined in this chapter demonstrates how this CBM approach can be implemented by including model reliability, fidelity and reliability of the inspection technique, and mission needs of the aircraft.

# CHAPTER 7

## SUMMARY AND FUTURE WORK

Traditional DT approaches to fatigue critical components have assumed a deterministic damage accumulation process where deterministic crack growth curves, constant material properties and specific initial flaw sizes are used. Since uncertainty is present at all levels of the crack growth simulation and data collection, this thesis develops systematic approaches to quantify and include these sources of uncertainty in DT risk assessment and management.

Chapter III was focused on the modeling of discretization errors. A non-parameterized crack representation was employed to model the effects of spatial and temporal discretization in 3-D finite element analysis of non-planar crack growth by modeling both the block estimates of the corrected fronts and the kinetics of crack growth in the low dimensional crack representation space. The principles involved and the solutions proposed are illustrated using data from FEA simulations of non-planar crack growth under variable amplitude variable duration multi-axial loading. The surrogate models were trained using FEA simulations at varying levels of discretization. The work presented in this chapter only considered one controlling spatial mesh control variable. An expansion of this methodology should focus on spatial meshes with multiple controlling parameters.

In Chapter IV, a framework was provided to apply knowledge of uncertainty sources present in fatigue crack growth experimentation toward the quantification of the

uncertainty in the parameters of a crack growth model aimed at predicting the outcome of the experimentation. Since Paris law was implemented throughout this thesis, the goal of the work in this chapter was to calibrate distributions for the material parameters $C$ and $m$. The typical distributions for these parameters used in most models include errors and uncertainties that should be attributed to other sources in the experimental process. Chapter IV provided a methodology to properly calibrate these values by including all known uncertainty sources in a Bayesian network. Some obvious future work on this topic would be further investigation of the fatigue experimentation procedure to identify and quantify more sources of error or uncertainty. While the techniques presented here addressed a visual imaging data acquisition system, the methodology is generic and applicable to other types of crack growth experiments.

The error sources identified in chapters III and IV were used to correct the model prediction in Chapter V. The equivalent planar crack growth model that was described in Chapter II was used to predict the crack growth in a rotorcraft mast under constant amplitude loading. The model was adjusted to account for both spatial and temporal discretization error and the model parameter calibration technique outlined in Chapter IV was used to determine the appropriate values for the Paris Law coefficients. These results were then compared against experimental data using a Bayesian hypothesis testing validation metric.

Chapter VI of the thesis was concerned with risk management. A methodology was presented in this chapter to determine maintenance inspection interval and fidelity level for a mechanical component in the aircraft. A reliability based validation metric was proposed as the method for determining the reliability limit to be placed on the

inspection interval length. A methodology was developed to use this reliability limit in conjunction with the DT methodology to determine safe and efficient inspection/maintenance scheduling for the demonstration component. Two types of inspection, LFI and HFI, were assumed available, and the crack growth prediction model was used to estimate the length of the next inspection interval depending on which inspection type was chosen. This information could be used in two ways: 1) select the inspection type with respect to the next individual mission duration, or 2) optimally schedule multiple missions. An extension of this work can consider additional measurable quantities such as crack depth measurement rather than only length, extent of corrosion damage, etc.

## REFERENCES


[1] Roylance, D., *Introduction to fracture mechanics*, Department of Materials Science and Engineering, Massachusetts Institute of Technology, Cambridge, MA, 2001.

[2] Reed, R., Smith, J. and Christ, B., "The economic effects of fracture in the United States," *SP647-1*, NBS, March 1983.

[3] Tong, Y., "Literature review on structural risk and reliability analysis," *Aeronautical and Maritime Research Laboratory – Report DSTO-TR-1110*, Melbourne, Australia, 2001.

[4] Haldar, A. and Mahadevan, S., *Probability, Reliability, and Statistical Methods in Engineering Design*, New York, John Wiley and Sons, 2000.

[5] Box, George E. and Tiao, G., *Bayesian inference in statistical analysis*. New York: Wiley, 1992.

[6] Ghanem, R. and Spanos, P., "Polynomial chaos in stochastic finite elements," *Journal of Applied Mechanics*, Vol. 57, No. 1, 1990, pp. 197–202.

[7] Boser, B., Guyon, I., and Vapnik, V., "A training algorithm for optimal margin classifiers," *Proceedings of the fifth annual workshop on Computational learning theory*, ACM, 1992, pp. 144–152.

[8] Tipping, M., "Sparse Bayesian learning and the relevance vector machine," *The Journal of Ma- chine Learning Research*, Vol. 1, 2001, pp. 211–244.

[9] Rasmussen, C., *Evaluation of Gaussian processes and other methods for non-linear regression*, Ph.D. thesis, University of Toronto, 1996.

[10] Santner, T., Williams, B., and Notz, W., *The design and analysis of computer experiments*, Springer Verlag, 2003.

[11] McFarland, J., *Uncertainty Analysis for Computer Simulations through Validation and Calibration*, Ph.D. thesis, Vanderbilt University, 2008.

[12] MacKay, D., "Introduction to Gaussian processes," *NATO ASI Series F Computer and Systems Sciences*, Vol 168, 1998, pp 133-166.

[13] Paciorek, C., *Nonstationary Gaussian processes for regression and spatial modeling*, Ph.D. thesis, Citeseer, 2003.

[14] Rasmussen, C. and Williams, C., *Gaussian processes for machine learning*, Springer, 2006.

[15] Cressie, N. and Huang, H., "Classes of Nonseparable, Spatio-Temporal Stationary Covariance Functions," *Journal of the American Statistical Association*, Vol 94, Issue 448, 1999, pp 1330-1340.

[16] Paciorek, C. and Schervish, M., "Nonstationary covariance functions for Gaussian process regression," *Advances in Neural Information Processing Systems*, Vol 16, 2004, pp 1-8.

[17] Ingrafea, T. et al., "FRANC3D, 3D Fracture Analysis Code," The Cornell University Fracture Group, Cornell University. Ithaca, NY, 1996.

[18] Hombal, V., Ling, Y., Wolfe, K., and Mahadevan, S., "Two-Stage Approximation of Non-Planar Crack Growth," *Engineering Fracture Mechanics*, Article in Press, Aug. 2012.

[19] Sankararaman, S., Ling, Y., Shantz, C. and Mahadevan, S., "Statistical inference of equivalent initial flaw size with complicated structural geometry and multi-axial variable amplitude loading," *International Journal of Fatigue*, Vol 32, Issue 10, 2010, pp 1689-1700.

[20] Sankararaman, S., *Uncertainty Quantification and Integration in Engineering Systems*, Ph.D. thesis, Vanderbilt University, 2012.

[21] Lee, P., *Bayesian statistics*. Arnold London, UK:, 2004.

[22] Newman Jr., J., "Analyses of Surface Cracks in Finite Plates Under Tension or Bending Loads," *NASA Technical Report*, Langley Research Center, 1979.

[23] Newman Jr., J. and Raju, I., "Stress intensity factor equations for cracks in three-dimensional finite bodies," *Fracture Mechanics*, Vol 1, 1983, pp 238-269.

[24] Hombal, V. and Mahadevan, S., "Surrogate Modeling of 3D Crack Growth", *International Journal of Fatigue*, Article in Press, Aug. 2012.

[25] ANSYS® Academic Research*, Release 13.0*

[26] Paris, P. and Erdogan, F., "A Critical Analysis of Crack Propagation Laws," *Journal of Basic Engineering – Transactions of ASME*, 1963, pp 528-534.

[27] De Boor, C., *A Practical Guide to Splines*, Springer, 2001.

[28] Prenter, P., *Splines and variational methods*, John Wiley and Sons, New York, 1975.

[29] Johnson, R. and Wichern, D., *Applied multivariate statistical data analysis*, Prentice Hall, Upper Saddle River, NJ, 2002.

[30] Ko, J. and Fox, D., "GP-Bayes Filters: Bayesian filtering using Gaussian process prediction and observation models," *Autonomous Robots*, Vol 27, Issue 1, 2009, pp 75-90.

[31] Wang, J., Fleet, D. and Hertzmann, A., "Gaussian process dynamical models for human motion," *IEEE Transactions on Pattern Analysis and Machine Intelligence*, 2007, pp 283-298.

[32] Yang, J. and Manning, S., "Stochastic Crack Growth Analysis Methodologies for Metallic Structures," *Engineering Fracture Mechanics*, Vol 37, Issue 5, 1990, pp 1105-1124.

[33] E08 Committee. *Test Method for Measurement of Fatigue Crack Growth Rates*. ASTM International, 2008. http://www.astm.org/doiLink.cgi?E647.

[34] Jones, R., S. Pitt, T. Constable, B. Farahmand, "Observations on fatigue crack growth in a range of materials", *Materials & Design*, Volume 32, Issues 8–9, September 2011, Pages 4362-4368.

[35] Kennedy, M. and O'Hagan, A., "Bayesian Calibration of Computer Models," *Journal of the Royal Statistical Society – Series B Statistical Methodology*, Vol 63, Issue 3, 2001, pp 425-464.

[36] Trucano, T., Swiler, L., Igusa, T., Oberkampf, W. and Pilch, M., "Calibration, Validation, and Sensitivity Analysis: What's What," *Reliability Engineering and System Safety*, Vol 91, 2006, pp 1331-1357.

[37] Griffith, D. and Carne, T., "Experimental Uncertainty Quantification of Modal Test Data," *25th International Modal Analysis Conference*, February 2007, Orlando, FL, USA

[38] Beretta, S. and Murakami, Y., "Statistical Analysis of Defects for Fatigue Strength Prediction and Quality Control of Materials," *Fatigue and Fracture of Engineering Materials and Structures*, Vol 21, Issue 9, pp 1049-1065.

[39] Murakami, Y. and Endo, M., "Effects of Defects, Inclusions and Inhomogeneities on Fatigue Strength," *International Journal of Fatigue*, Vol 16, Issue 3, 1994.

[40] Vasudevan, A., Sadananda, K. and Glinka, G., "Critical Parameters for Fatigue Damage," *International Journal of Fatigue*, Vol 23, 2001, pp S39-S53.

[41] Lee, W., Sue, W., Lin, C. and Wu, C., "The strain rate and temperature dependence of the dynamic impact properties of 7075 aluminum alloy," *Journal of Materials Processing Technology*, Vol 100, Issues 1-3, pp 116-122.

[42] Kandil, F. and Dyson, B., "The Influence of Load Misalignment During Low-Cycle Fatigue Testing. I: Modeling. II: Applications," *Fatigue and Fracture of Engineering Materials and Structures*, Vol 16, Issue 5, pp 509-537.

[43] Kandil, F. and Dyson, B., "Prediction of Uncertainties in Low-Cycle Fatigue Data," *Proceedings of the 5$^{th}$ International Conference on Creep and Fracture of Engineering Materials and Structures*, March-April 1993, University College Swansea, Institute of Materials, London, pp 517-525.

[44] MATLAB®, r2011a, The Mathworks, Natick, MA.

[45] Jensen, F., *An introduction to Bayesian networks*, Vol 210, UCL Press, London, 1996.

[46] Heckerman, D., "A tutorial on learning with Bayesian networks," *Innovations in Bayesian Networks*, 2008, pp 33-82.

[47] Gurney, T., *An Analysis of Some Fatigue Crack Propagation Data for Steels Subjected to Pulsating Tension Loading*, The Welding Institute, 1978

[48] Cortie, M. and Garrett, G., "On the correlation between the $C$ and $m$ in the paris equation for fatigue crack propagation," *Engineering Fracture Mechanics*, Vol 30, Issue 1, 1988, pp 49-58.

[49] A. Carpinteri and M. Paggi, "Are the Paris' law parameters dependent on each other?", *Frattura ed Integrita Strutturale*, Vol. 2, pg. 10–16, 2007.

[50] Richards, S., "Completed richardson extrapolation in space and time." *Commun. Numerical Methods Eng.*, Vol. 13, pg 573-585, 1997.

[51] Liu, Y. and S. Mahadevan, "Threshold stress intensity factor and crack growth rate prediction under mixed mode loading," *Engineering Fracture Mechanics*, Vol. 74, pg 332-345, 2007.

[52] Shah, R., "Fracture under combined modes in 4340 steel." *ASTM STP 560*, 29-52 (1974).

[53] Cowie, J., "The influence of second-phase dispersions on shear instability and fracture toughness of ultrahigh strength 4340 steel." *US Army Mat. Tech. Lab. Rep.* (1989) MTL-TR 89-20 .

[54] Rebba, R. and Mahadevan, S., "Computational Methods for Reliability Assessment." *Reliability Engineering and System Safety*, Vol 93, 2008, pp 1197-1207.

[55] Farrar, C. and Lieven, N., "Damage Prognosis: The Future of Structural Health Monitoring," *Royal Society A: Mathematical, Physical and Engineering Science*, Issue 365, 2007, pp 623-632.

[56] Ling, Y. and Mahadevan, S., "Integration of Structural Health Monitoring and Fatigue Damage Prognosis," *Mechanical Systems and Signal Processing*, Vol 28, 2012, pp 89-104.

[57] Grall, A., Berenguer, L. and Dieulle, A., "A condition-based maintenance policy for stochastically deteriorating systems," *Reliability Engineering and System Safety*, Vol 76, 2002, pp 167-180.

[58] Faccioli, R., Ferrettii, C., Piva, R., Copello, S., "System fatigue updating for offshore structures", *Proceedings of the 14th International Conference on Offshore Mechanics and Arctic Engineering*, Copenhagen, 1995.

[59] Onoufriou, T., Fowler, D., Smith, J.K., "Reliability-based optimized inspection planning", *Proceedings of 7th International Conference on Behavior of Offshore Structures*, Boston, 1994.

[60] Shetty, N.K., Gierlinski, J.T., Smith, J.K., Stahl, B., "Structural system reliability considerations in fatigue inspection planning", *Proceedings of the 8th International Conference on the Behavior of Offshore Structures*, Delft, 1997.

[61] Stratman, B., *Reliability and Clustering Techniques for Inspection Optimization of Large Populations*, Ph. D. Dissertation, Vanderbilt University, 2007.

[62] Garbatov, Y., Soares, C.G., "Cost and reliability based strategies for fatigue maintenance planning of floating structures", *Reliability Engineering & System Safety*, Vol. 73 (Issue 3), pp. 293-301, 2001.

[63] Zhang, R., Mahadevan, S., "Reliability-based reassessment of corrosion fatigue life", *Structural Safety*, Vol. 23 (Issue 1), pp. 77-91, 2001.

[64] McLemore, K., *Test Campaign for Model Uncertainty Reduction*, Master's thesis, Vanderbilt University, 2012.

[65] Staszewski, W., Boller, C. and Tomlinson, G., *Health Monitoring of Aerospace Structures: Smart Sensor Technologiesand Signal Processing*, New York, John Wiley and Sons, 2004.

[66] Baldev, R., Jayakumar, T. and Thayasimuthu, M., *Practical non-destructive testing*. New Delhi, India, Narosa Pub. House, 2002.

[67] Zhang, R. and Mahadevan, S., "Fatigue reliability analysis using nondestructive inspection," *Journal of Structural Engineering*, Vol 127, Issue 8, 2001, pp 957.

[68] Hull, B. and John, V., *Non-destructive testing*, London, Macmillan Education, 1988.,

[69] Berens, A and Hovey, P., "Statistical methods for estimating crack detection probabilities," *Probabilistic fracture mechanics and fatigue methods: applications for structural design and maintenance, STP 798 – ASTM*, 1983

[70] Anderson, T., *Fracture Mechanics*, Boca Raton, FL, CRC Press, 1991.